2004

Effects Of Bond Coat Surface Preparation On Thermal Cycling Lifetime And Failure Characteristics Of Thermal Barrier Coatings

Jing Liu
University of Central Florida

EFFECTS OF BOND COAT SURFACE PREPARATION ON THERMAL CYCLING LIFETIME AND FAILURE CHARACTERISTICS OF THERMAL BARRIER COATINGS

by

JING LIU
B.S. Beijing Polytechnic University, 2002

A thesis submitted in partial fulfillment of the requirements
for the degree of Master of Science
in the Department of Mechanical, Materials, and Aerospace Engineering
in the College of Engineering and Computer Science
at the University of Central Florida
Orlando, Florida

Summer Term
2004

Major Professor: Dr. Yong-ho Sohn

ABSTRACT

Thermal barrier coatings (TBCs) have been widely used in gas turbine engines to protect the underlying metal from high operating temperature so as to improve the durability of the components and enhance the engine efficiency. However, since the TBCs always operate in a demanding high-temperature environment of aircraft and industrial gas-turbine engines, a better understanding of this complex system is required to improve the durability and reliability.

The objective of this study is to investigate the effects of surface modification for the NiCoCrAlY bond coats on the thermal cycling lifetime and failure characteristics of TBCs. Parameters of modification for the bond coats included as-sprayed, barrel-finished, hand-polished and pre-oxidation heat treatment at 1100°C in $P_{O_2}=10^{-8}$ atm up to 4 hours, carried out prior to the electron beam physical vapor deposition (EB-PVD) of ZrO_2-7wt% Y_2O_3 (7YSZ) ceramic topcoat. The resulting characteristics of the bond coat and the thermally grown oxide (TGO) scale were initially documented by surface roughness, phase constituents of the TGO scale, and residual stress of the TGO scale. The thermal cycling test consisted of 10-minute heat-up to 1121°C, 40-minute hold at 1121°C, and 10-minute forced air-quench. As-coated and thermally-cycled TBCs were characterized by optical profilometry (OPM), photo-stimulated luminescence spectroscopy (PSLS), optical microscopy, scanning electron microscopy (SEM) equipped with energy dispersive spectroscopy (EDS), and scanning/transmission electron

microscopy (TEM/STEM) equipped with high angle annular dark field (HAADF) and X-ray energy dispersive spectroscopy (XEDS). TBC specimens for TEM/STEM analysis were prepared by focused ion beam (FIB) in-situ lift-out (INLO) technique.

Superior thermal cycling lifetime was observed for TBCs with as-sprayed bond coats regardless of pre-oxidation heat treatment, and TBCs with hand-polished bond coats only after pre-oxidation heat treatment. With pre-oxidation heat treatment, relative photostimulated luminescence intensity of the equilibrium α-Al_2O_3 increased. Thus, the improvement in TBC lifetime can be correlated with an increase in the amount of α-Al_2O_3 in the TGO scale, given a specific surface modification/roughness. The lifetime improvement due to pre-oxidation was particularly significant to TBCs with smooth hand-polished bond coats and negligible for TBCs with rough as-sprayed bond coats.

Spallation-fracture paths depended on the lifetime of TBCs. Premature spallation of TBCs occurred at the interface between the YSZ and TGO. Longer durability can be achieved by restricting the fracture paths to the TGO/bond coat interface. Small particulate phase observed through the TGO scale was identified as Y_2O_3 (cubic) by diffraction analysis on TEM. While small addition of Y in the NiCoCrAlY bond coat helps the adhesion of the TGO scale, excessive alloying can lead to deleterious effects.

This work is dedicated to my family.

ACKNOWLEDGEMENTS

I would like to express my deep gratitude to my advisor Dr. Yong-ho Sohn. His technical guidance, life counsel, continuous support, encouragement help and patience have always been highly appreciated. I would like to give special thanks to University of Connecticut for funding this project as well as Howmet Research Corporation and Pratt & Whitney for specimen preparation and technical assistance. Sincere appreciation goes to the committee members, Dr. Desai and Dr. Heinrich, and fellow graduate students in the High Temperature Material Laboratory. My thanks also extend to the Zonta International Foundation who awarded me a Zonta International Amelia Earhart Fellowship for my study. Finally, sincere thanks go to my family for their support and understanding.

TABLE OF CONTENTS

LIST OF TABLES

LIST OF FIGURES

1. INTRODUCTION

Greater efficiency and output of gas turbines, which inescapably connotes an increase in turbine inlet temperature, require methods by which temperature limits can be surmounted by overcoming hot-section material restraints. Thermal barrier coatings (TBCs) are the most promising and exciting development to meet this demand. Being widely used in the hot section in both aero and land-based gas turbines, TBCs have improved the power and efficiency of gas turbine engines dramatically.[1,2,3,4,5] For instance, it has been reported that a 170°C increase in the engine operating temperature can improve the engines thrust by 5.0% and efficiency by 1.0%.[6] TBCs have the potential for increasing the temperature capability of gas turbines by 90~150°C: significantly above what is achievable with the most advanced superalloys.[7] Moreover, this large temperature increment is equivalent to at least three generations of new superalloys development, which would be difficult or perhaps impossible, for Co- or Ni-based superalloys, which are the current choices for high temperature materials.[8]

Generally, TBC system consists of four layers: ceramic topcoat, thermally grown oxide (TGO) scale, metallic bond coat, and superalloy substrate. Over the years, a number of ceramics have been suggested and tested as TBCs or anticorrosion coatings in engines. However, zirconium dioxide (ZrO_2) in its stabilized form appears to be optimum choice as determined originally by NASA.[9] Stabilization of high temperature tetragonal phase down to ambient temperature is essential for ZrO_2-based coatings. Through

decades of study, Y_2O_3 (7~8wt.%) partially stabilized zirconia (YSZ) successfully met the requirements of many high temperature applications.

TBCs must be strain tolerant to avoid instantaneous delamination by incorporating either microcracks or aligned porosity.[10] Two established methods for depositing the ceramic topcoat are air plasma spray (APS), and electron beam physical vapor deposition (EB-PVD). In APS, particulate matters introduced into the plasma is heated to a liquid state and accelerated toward the work piece. Upon impact, the hot particles deform to form splats and produce a complex interlocked mcirostructure. EB-PVD method uses an electron beam to evaporate the oxide from an ingot, and components are coated by vapor condensation. The EB-PVD ceramic topcoat generally exhibits longer durability with strain-tolerant columnar microstructure and strong atomic-level adhesion with the substrate. EB-PVD topcoat also has the following advantageous properties: good thermal shock resistance, aerodynamically smooth surfaces and good erosion resistance.[11] Therefore, in this study, EB-PVD was employed for the topcoat deposition.

The bond coats are deposited by low pressure/vacuum plasma spray (LPPS/VPS) or EB-PVD for the MCrAlY (M=Ni and /or Co) bond coat, and a combination of electroplating in conjunction with diffusion – aluminizing or chemical vapor deposition (CVD) for the (Ni,Pt)Al bond coat.[12,13] During engine application, the bond coat temperature in gas turbine engines typically exceeds 700°C, resulting in bond coat oxidation and inevitable formation of the TGO scale between the bond coat and the ceramic topcoat.[14] The interconnected porosity and microcracks that exist in the topcoat

allow the oxygen to easily oxidize the bond coat surface. Moreover, even if the topcoat were fully dense, the extremely high ionic diffusivity of oxygen in the YSZ topcoat renders it oxygen transparent. Furthermore, the TGO scale also forms during the bond coat processing and topcoat deposition. Although the formation of the TGO is inevitable, the ideal bond coat is engineered to strive for the formation of uniform and defect-free oxidation scale consisting of α–Al_2O_3 that possesses a slow growth rate. Such a TGO has a very low oxygen ionic diffusivity and provides an excellent diffusion barrier, retarding further bond coat oxidation.[15]

The growth of TGO during service is considered to be the crucial phenomenon responsible for the failure of TBCs.[16] TGO growth results in a constrained volume expansion that leads to compressive "growth" stresses (<1 GPa)[17] persisting at all temperatures. Upon cooling, the thermal expansion mismatch between the TGO and bond coat leads to a very high compressive residual stress in the TGO up to 6 GPa.[18,19,20] The large compressive residual stress in the TGO provides the strain energy that can drive spallation, typically within and/or near the TGO scale.

In addition, phase constituent of the TGO is considered to be a critical factor influencing the adhesion at the TGO/YSZ interface. The formation of the metastable θ-Al_2O_3 and its conversion to the stable α-Al_2O_3 in the TGO has been reported to have a profound effect on the structural integrity of the TGO/YSZ interface during thermal cycles.[21,22] The polymorphic transformation of Al_2O_3 may be responsible for additional residual stress from the volumetric constraint in the TGO and the nucleation of sub-critical cracks, eventually leading to the spallation of the TGO.[23,24] Thus, the formation of

a “perfect” TGO that only consists of α-Al_2O_3 prior to the deposition of topcoat can help to improve the oxidation resistance and enhance the durability and reliability of TBCs.

Moreover, the initial defects and surface irregularities of the bond coat can give rise to in-plane and out-of-plane tensile stresses. These tensile stresses can crack the TGO at the microstructural scale. Cracks in the TGO can admits molecular oxygen to the bond coat surface and accelerates oxidation, further creating out-of-plane tensile stresses across the TGO/bond coat interface, and eventually leading to spallation.[25,26] Therefore, good bond coat surfaces can enhance the adhesion of the TGO to bond coat, and elongate the lifetime of the TBCs.

The main objective of this study is to examine the lifetime and failure characteristics of TBCs as a function of bond coat surface preparation and associated with TGO formation. Specifically, the effects of bond coat surface modification and pre-oxidation heat treatment for the NiCoCrAlY bond coat (PWA276), carried out prior to the application of the EB-PVD YSZ topcoat, on the thermal cyclic lifetime of TBCs were investigated. Microstructural development and failure characteristics of TBCs were examined by using optical profilometry (OPM), photo-stimulated luminescence spectroscopy (PSLS), optical microscopy (OM), scanning electron microscopy (SEM) equipped with energy dispersive spectroscopy (EDS), focus ion beam in-situ lift-out (FIB-INLO), transmission electron microscopy (TEM) and scanning TEM (STEM). In order to achieve the main objective, the following studies were carried out.

1) Effects of bond coat surface roughness and pre-oxidation on the thermal cyclic lifetime of TBCs. The roughness of the bond coat determined by OPM was varied

by three different processing routes: as-sprayed; barrel-finished; and hand-polished. The pre-oxidation heat treatment was carried out at 1100°C with P_{O_2} = 10^{-8} atm for 2-4 hours.

2) Bond coat processing effects on the phase constituents and compressive residual stress of the TGO for as-received TBCs and as a function of thermal cycling.
3) Relationship between the microstructural development, failure characteristics and thermal cyclic lifetime of TBCs.

2. LITERATURE REVIEW

2.1 Thermal Barrier Coatings (TBCs)

In general, TBC system consists of four layers, as shown in Fig. 1: (1) a thermally insulating ceramic topcoat (typically yttria partially stabilized zirconia, YSZ) with low thermal conductivity and chemical inertness in combustion atmospheres; (2) a metallic bond coat that forms a TGO scale to protect the turbine blades against environmental degradation by reducing hot corrosion and oxidation attack; (3) a TGO scale that forms during processing as well as in service, and is the real bonding layer between the ceramic topcoat and the metallic bond coat; and (4) the superalloy substrate to sustain strength at high temperatures. TBC, as a system provides a thermal and oxidation barrier between the hot gases and air cooled turbine blades and vanes. The reduction of surface temperature of the metal component enables conventional superalloys to be continuously used. Therefore, an increase of the engine operating temperature and/or a prolongation of component lifetime at current temperatures can be achieved.[27]

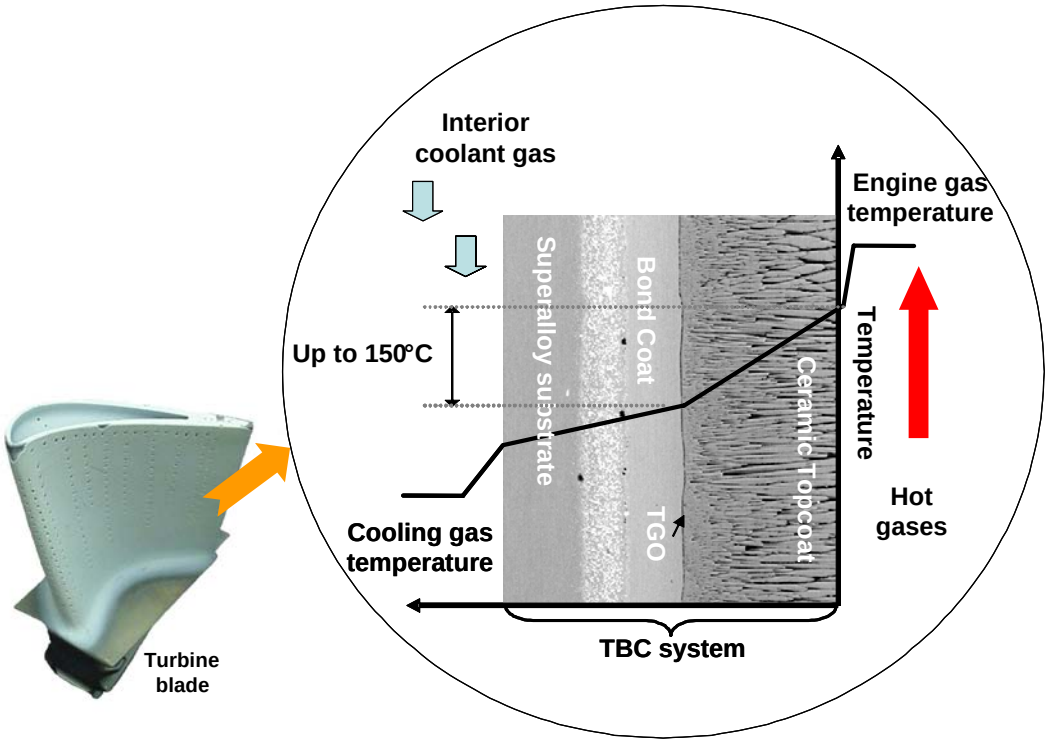

Figure 1. Typical TBC system and its application.

2.1.1 Ceramic Topcoat

The ceramic topcoat is required to create the temperature gradient across the thickness of the coating. Therefore, this layer is likely to have high melting point, high surface emissivity, low thermal conductivity, high thermal shock resistance, low vapor pressure, resistance to oxidation or chemical degradation, and high coefficient of thermal expansion. A porous, columnar or splat-quenched, 100-400 μm thick, yttria stabilized zirconia (YSZ) layer is currently preferred for this function.[28] Generally, 6-8 wt.% Y_2O_3 is used to stabilize zirconia and retain the non-equilibrium tetragonal (t') phase with high

resistance to thermal decomposition, degradation by H_2O vapor, and grain growth.[29] Partially stabilized zirconia is outstanding in terms of a thermal conductivity, which is approximately 100 times lower than that of α-Al_2O_3. It also has one of the highest coefficient of thermal expansion among common oxides (except for MgO): 11×10^{-6} $^oC^{-1}$ at 1000^{o}C, quite close to 17×10^{-6} $^oC^{-1}$ for average Ni-based superalloys.[30] Moreover, the partially stabilized zirconia is regard to have excellent thermal shock resistance, high strength, and high fracture toughness by a ferroelastic domain-switching mechanism that remains active at temperatures up to 1400^{o}C.[31]

2.1.2 Electron Beam Physical Vapor Deposition (EB-PVD)

Physical vapor deposition emerged in the 1960s as one of the primary overlay coating production technique. The term physical vapor deposition (PVD) refers to deposition of materials by vapor transport in a vacuum without the need for a chemical reaction.[32] Since the 1980s, EB-PVD technology has been employed for TBCs. Today it is one of the most commonly used methods for coating turbine airfoil components.[33]

Fig. 2 shows a schematic diagram of a typical coating chamber for EB-PVD process. An ingot of the appropriate composition is vaporized in vacuum using a high power density heat source such as an electron beam (100 - 200 kW). The parts to be coated are manipulated within the vapor cloud with the material condensing on the preheated substrate surface. The composition of the deposited coating will often be different from that of the starting ingot, due to differences in vapor pressure; therefore,

the composition of the ingot must be adjusted accordingly. This technology has progressed to where the elements with a broad range of vapor pressures can be simultaneously evaporated from a single source.

The EB-PVD provides TBCs with many advantageous properties, such as good thermal shock resistance, aerodynamically smooth surfaces and good erosion resistance.[10] The deposition conditions are designed to create a columnar grain structure shown in Fig. 3 with both intra- and inter-columnar porosities to enhance the thermal resistance and the strain tolerance. [34] As described by Strangman, "strain within the coatings is accommodated by free expansion of the columns into the gaps, which results in negligible stress buildup".[35]

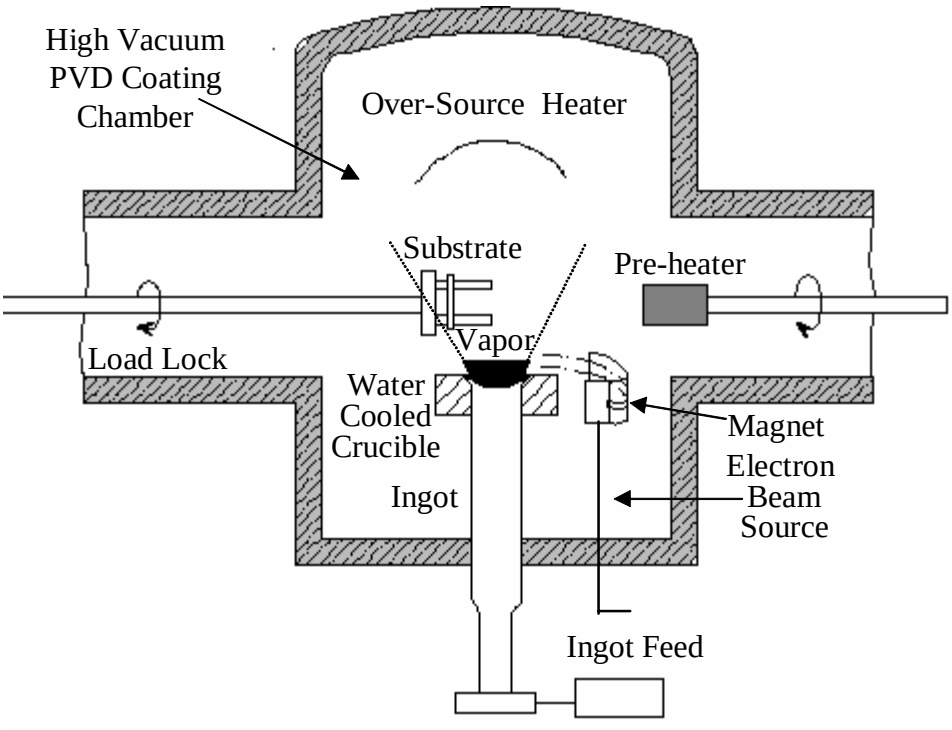

Figure 2. A schematic illustration of an EB-PVD coatings chamber.[36]

Unfortunately, the control over many variables in EB-PVD processing can be difficult. The engineering constraints on coatings deposition using EB-PVD therefore can limit the means available to introduce porosity in the coating.[37]

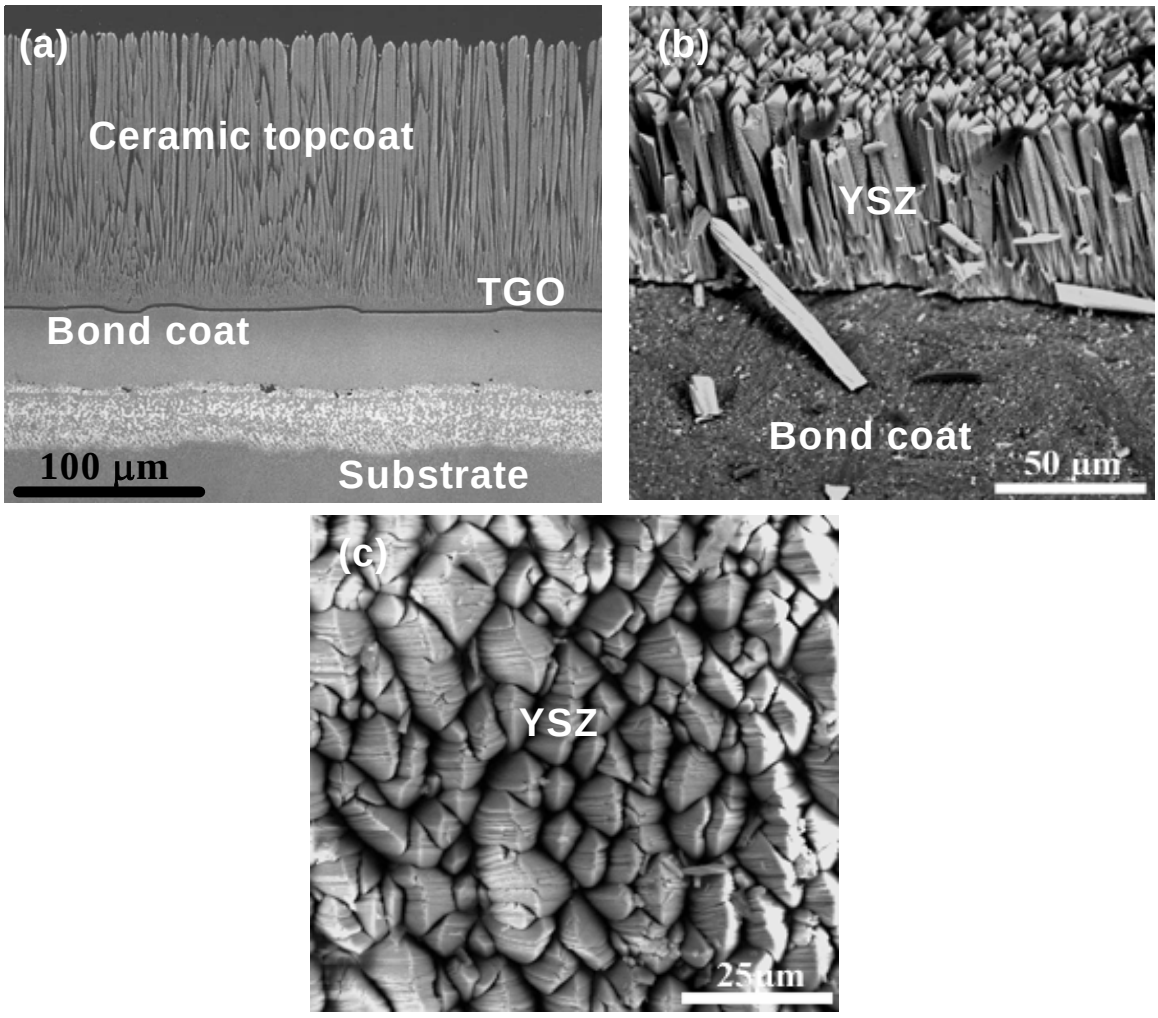

Figure 3. Typical EB-PVD TBC system, showing the columnar structure of YSZ ceramic topcoat. (a) Cross-sectional backscattered electron micrograph of EB-PVD TBC system; (b) Backscattered electron micrograph of the fractured YSZ topcoat; and (c) Secondary electron micrograph of the top view of YSZ columnar structure.

2.2 Bond Coats

Since the ceramic topcoat is transparent to oxygen transport due to its porosity and high ionic diffusivity, the oxidation resistant layer is required to protect the underlying turbine blade from environmental degradation. This layer is also important for adhesion, and reduces the thermal expansion mismatch between the ceramic topcoat and superalloy substrate. Studies on the bond coats have documented that the composition, microstructure, thickness, surface roughness and processing technique have strong effects on the durability and reliability of TBCs.[38,39,40,41,42]

2.2.1 Types of Bond Coat

A typical bond coat contains Nickel, Cobalt, Chromium, Aluminum, and Yttrium, with Nickel as the primary solvent. This kind of bond coat is well known as MCrAlY bond coat (where M can be Nickel, Cobalt, or mixtures of both).[43,44] There are usually two phases in the MCrAlY bond coat: β-NiAl (B2) and γ-Ni (fcc) solid solutions. MCrAlY coating, in general, has a higher Aluminum content than the superalloy substrates and can act as a reservoir of Aluminum to form Al_2O_3 oxide scale. Yttrium is added at very low concentration to improve the adhesion of the TGO, primarily by acting as a solid state gettering site for Sulfur, which diffuses from the substrate and poisons the metal/oxide interface.[45,46,47,48] Another type of bond coat with similar function is the diffusion aluminide bond coat. For better oxidation and hot-corrosion resistance, Platinum has been incorporated, forming (Ni,Pt)Al bond coats, although the mechanism

by which Platinum exerts its beneficial effects is not well understood.[49,50] Both diffusion aluminide and (Ni,Pt)Al bond coats typically contain single β-phase, with various solid solutioning.[51] Though (Ni,Pt)Al bond coats provide a longer lifetime for TBCs, it is much more expensive than MCrAlY bond coats. Therefore, MCrAlY bond coats are still widely used in industry.

The bond coat composition is designed to obtain a highly adherent TGO. The best durability of TBCs were demonstrated (in weight percent) with vacuum plasma sprayed Ni-35Cr-5.9Al-0.95Y by Stecura[39] and Miller *et al.*, and with vacuum plasma sprayed Ni-4Co-9Cr-6Al-0.3Y plus aluminization by Wortman *et al.*.

2.2.2 Plasma Spray

Low pressure plasma spray (LPPS) was used for the NiCoCrAlY bond coat deposition in this study. LPPS is a relatively new method for depositing coatings that are rich in reactive element such as Aluminum and Chromium. The low-pressure environments minimize the formation of oxide defects within the coating structure. The advantages of the low-pressure process include higher powder particle velocities and broader spray patterns.[52] Coatings also can be made under the cover of an inert gas (e.g., Ar) shroud.

Fig. 4 shows a schematic diagram of typical plasma spray process. The process involves the injection of material, usually in the form of pre-alloyed powder, into a high-temperature plasma gas stream that has been created inside a plasma gun. Here, the powder particles are melted and accelerated toward the substrate. The molten metal then

spreads out onto the substrate surface and solidifies (i.e., splat quench). The parameters of the process, such as the amount of preheat, plasma gun characteristics, gun to workpiece distance, and so on, all influence the structure and properties of the deposit. Typically, the surface finish of plasma-sprayed coatings is rougher than that of EB-PVD coatings, and finishing operations must be performed to meet the required aerodynamic specifications. The microstructure of typical LPPS NiCoCrAlY coatings is shown in Fig. 5.

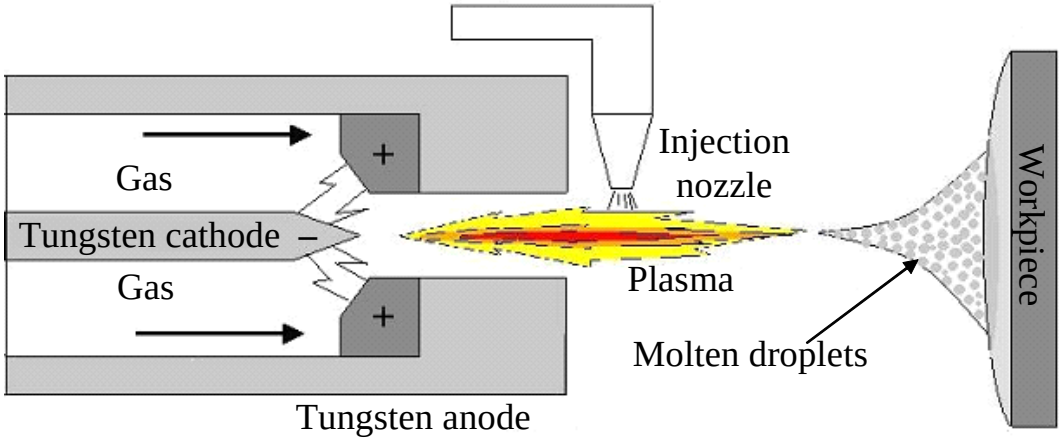

Figure 4. A schematic diagram of plasma spray process.[53]

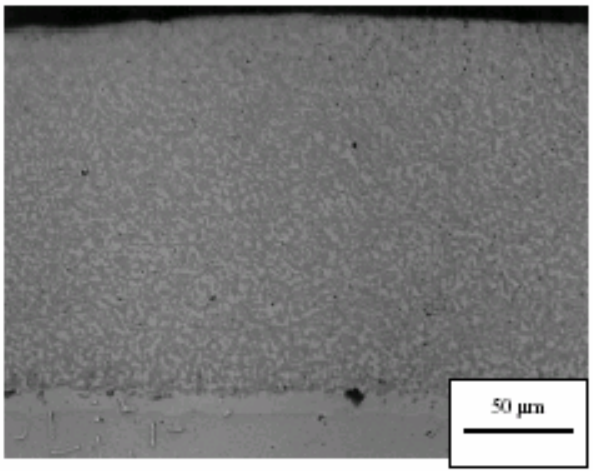

Figure 5. Low-pressure plasma sprayed NiCoCrAlY coating on a Ni-base superalloy substrate.[54]

2.3 Characterization of Bond Coat Surfaces

2.3.1 Surface Roughness of the Bond Coats

Extensive microstructural examination of TBCs with (Ni,Pt)Al bond coat by Gell and coworkers[55,56] has identified bond coat surface features/defects as damage initiation sites. Fig. 6 shows these surface features/defects to be: “ridges” associated with (Ni,Pt)Al bond coat and “entrapped” oxides associated with shot-peening of MCrAlY coatings. Also presented in Fig. 6 are the oxide cavities and accelerated growth of oxide scale resulting from the cyclic plasticity of these features/defects during thermal cycling.

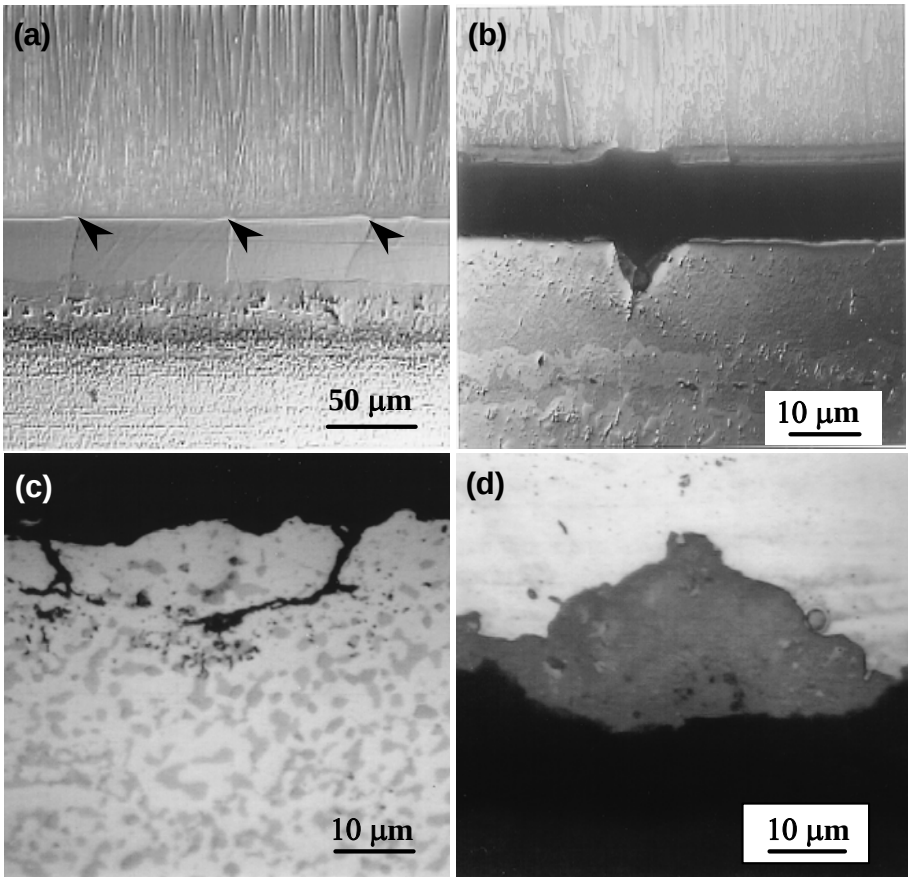

Figure 6. Surface features/defects: (a) “ridges” and (b) oxide-filled cavities in platinum aluminide (Pt-Al) EB-PVD TBCs; (c) “entrapped” oxides and (d) oxide-filled cavities associated with MCrAlY EB-PVD TBCs. These features/defects are present due to the processing of the bond coats before thermal cycling and evolve into oxide-filled cavities during thermal cycling.[55,56]

As well-known, the growth of TGO, thermal expansion mismatch between the TGO and bond coat, and phase transformations of the Al_2O_3 polymorphs contribute to the residual stresses within the TGO scale. In addition, the bond coat surface roughness has a significant effect on the in-plane and out-of plane tensile stresses as illustrated in Fig. 7. In-plane tensile stresses can crack the TGO, admit molecular oxygen to the bond coat

surface, and accelerate oxidation. Out-of-plane tensile stress eventually leads to TGO and TBC spallation.[25,26,57]

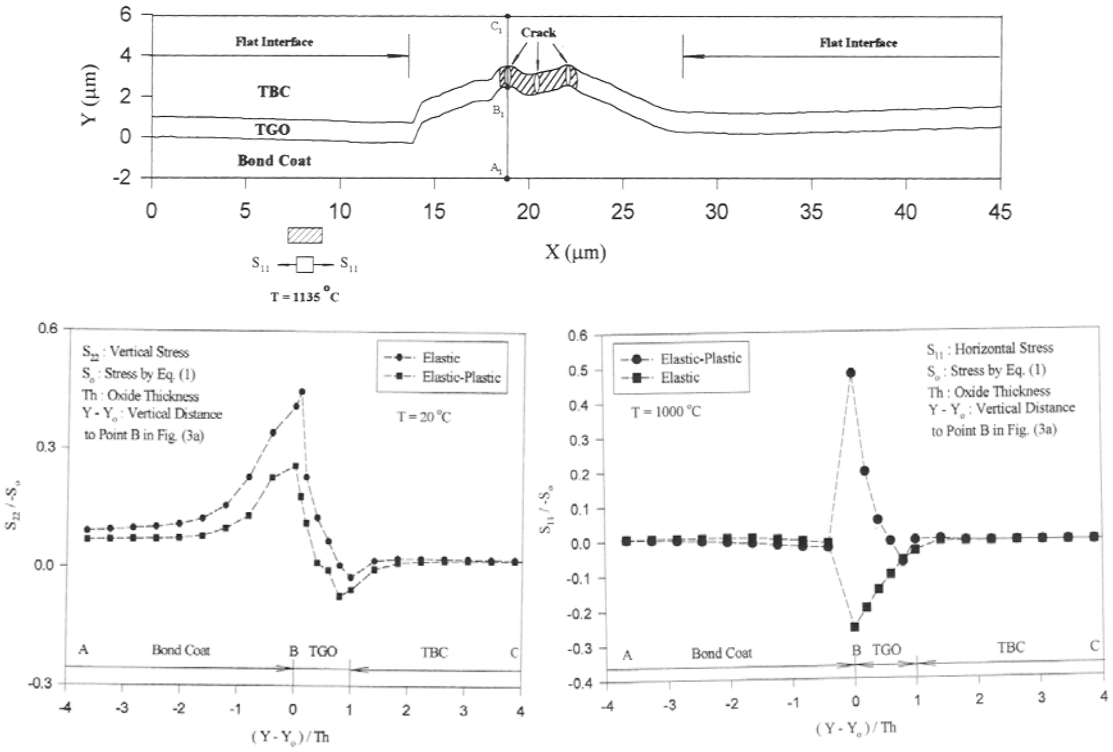

Figure 7. Tensile stress calculated from finite element analysis for out-of-plane (vertical) and in-plane (horizontal) stress in the TGO along the line A-B-C near the ridge of the Pt-Al bond coat surface.[25]

Fig. 8 shows a schematic illustration from Gell's research group, comparing the mechanisms of damage initiation and progression of the (Ni,Pt)Al/EB-PVD TBCs with and without bond coat ridges. In the specimens with ridges, the spalled YSZ is broken into dozens of smaller pieces at cavity/grain boundary sites. Damage progression occurs from multiple cavity/grain boundary sites and likely involves crack link-up and

progression. The spallation occurs because once a single crack gets started, the crack encounters the nearby stress fields associated with the geometrical arrays of cavities at most grain boundaries. Rapid crack link-up and macro-crack propagation occurs. In contrast, the TBCs with smooth bond coats surface spall by a buckling mode over a rather large area.[57] A number of distinctly separate buckles develop over a large number of cycles to get sufficiently large contiguous debonded region for buckling. However, as the strain energy release rate driving delamination increases with increasing oxide thickness, the buckling tendency requiring a critical size of the debonded region decreases with increasing oxide thickness. Therefore, an increase in oxide thickness alone does not lead directly to buckling spallation. Thus, for samples with smooth bond coat surface, spallation involves a more difficult and time-consuming degradation process, which leads to a longer lifetime.[57]

Therefore, a reliable industrial processing technique that ensures optimum MCrAlY bond coat surface roughness, which can be examined by optical profilometry, is also an important factor controlling the lifetime of the TBCs.

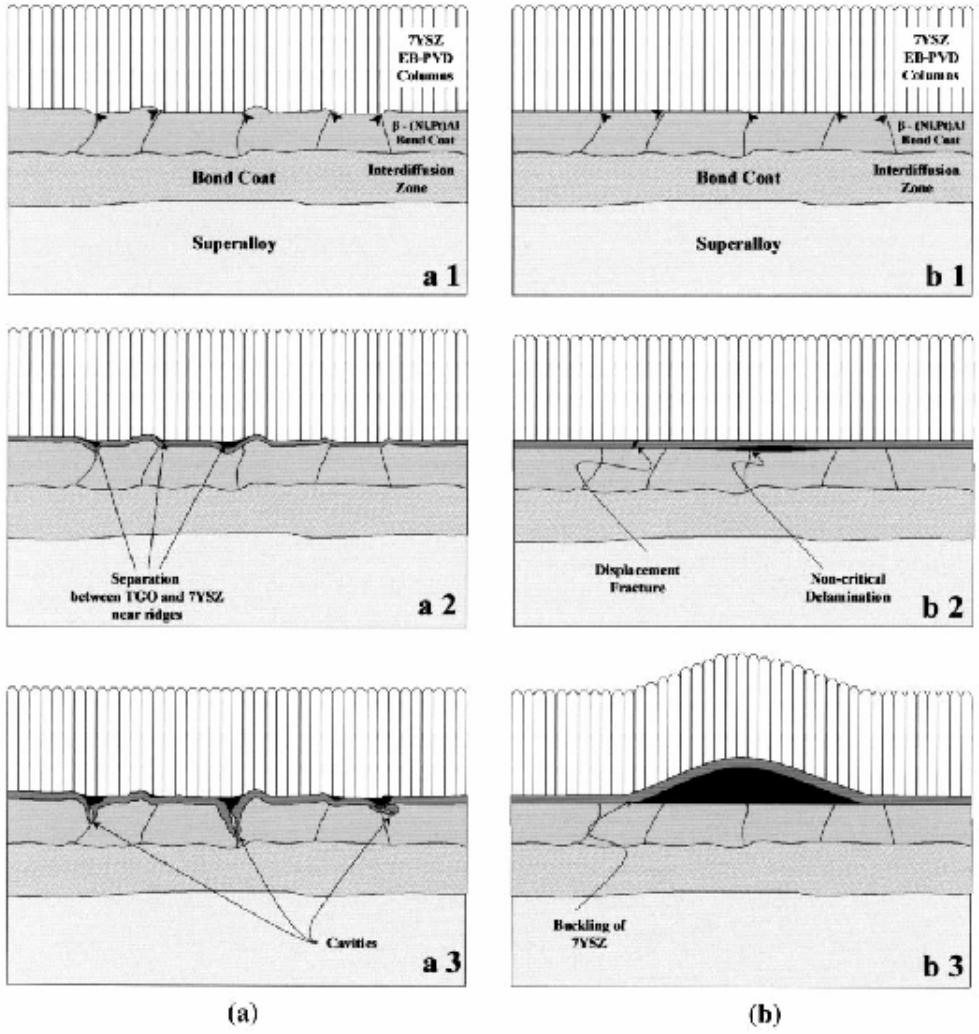

Figure 8. Schematics of thermal cycling failure mechanism in (Ni,Pt)Al/EB-PVD TBCs (a) with bond coat ridges and (b) without bond coat ridges. The thermal cyclic lifetime during failure shown in b3 is approximately three times as that in a3.

2.3.2 Optical Profilometry (OPM)

Fig. 9 shows the principle of OPM schematically. The OPM utilizes the interference of light to determine surface topography and transmission properties. An

interference microscope compares a sample's surface to an internal reference mirror. The difference in shape between the sample and the mirror produces a contour map (via some small amount of computer processing). In the diagram the sample is a nominally flat tilted mirror and the resulting interference pattern is characteristic of an inclined plane. Each band in the interference pattern represents a contour height of half the wavelength of "light": 0.2750μm. Allowing for any electronic variations, the contour bands are purely sinusoidal in shape hence the exact position of any point along the wave can be determined to a very high degree of accuracy.

To measure the sample's relative height from such interference patterns, a piezo electric crystal moves the reference mirror in small increments (90 degree segments). The computer stores an image of the sample at each position. The computer then calculates the phase equation, which determines the exact location of each pixel in the camera image in terms of its height above the surface.

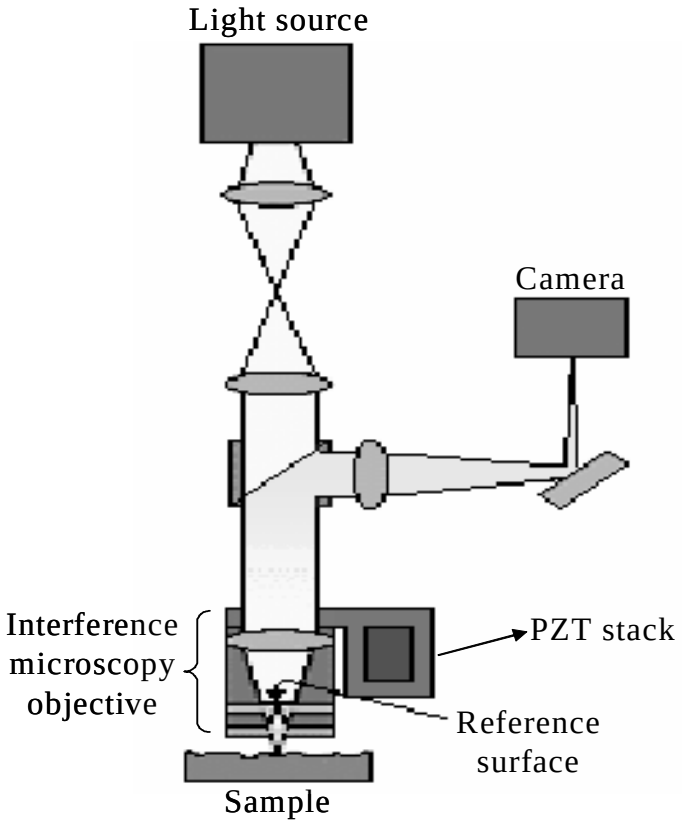

Figure 9. A schematic representation of the principle of optical profiling system.[58]

Fig. 10 shows the non-contact NT3300 OPM used in this study. It can rapidly and accurately measure the 3D surface topography, heights from Angstroms to millimeters, with vertical resolution to 0.1 nm. The OPM has been ideally suited for wide applications, including quality inspection, failure analysis and rapid production measurement of MEMS, semiconductor packaging, medical devices, automotive systems and many other applications.[59,60,61] Generally, there are two modes available for the OPM: for smoother surfaces, the phase-shifting integrating (PSI) bucket technique is used since it gives sub-nanometer height resolution capacities by using a monochromatic light source.[62,63] For

rougher surfaces, a vertical scanning (VSI) coherence sensing technique can be used to give nanometer height resolution over several hundred microns of surface height by using white light.[64,65,66,67]

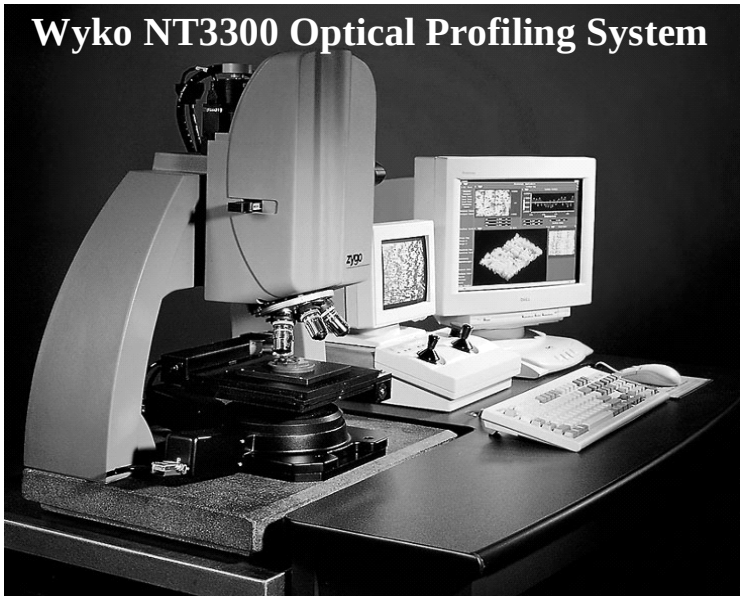

Figure 10. Typical experimental set-ups for optical profiling system.

Figs. 11 and 12 show the typical surface roughness and quantity measurements of the bond coat surfaces using PSI and VSI mode, respectively. The figures on the left are 2D surface analysis and on the right are 3D surface analysis. In VSI mode, the y-axis is in micrometers. While in PSI mode, the y-axis is in nanometers.

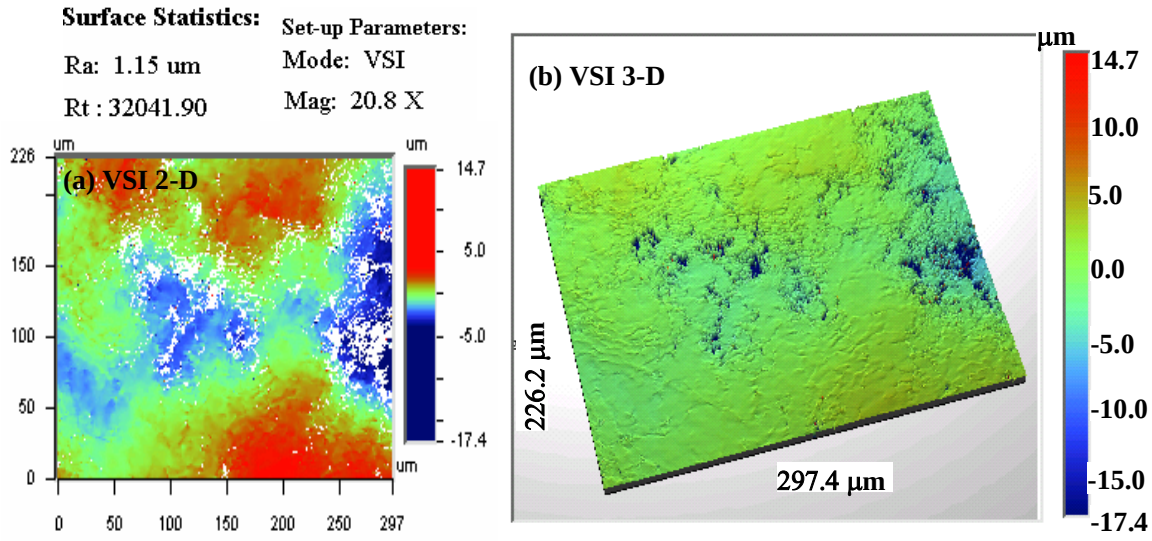

Figure 11. Typical surface roughness profile of rough bond coat surface using VSI mode.

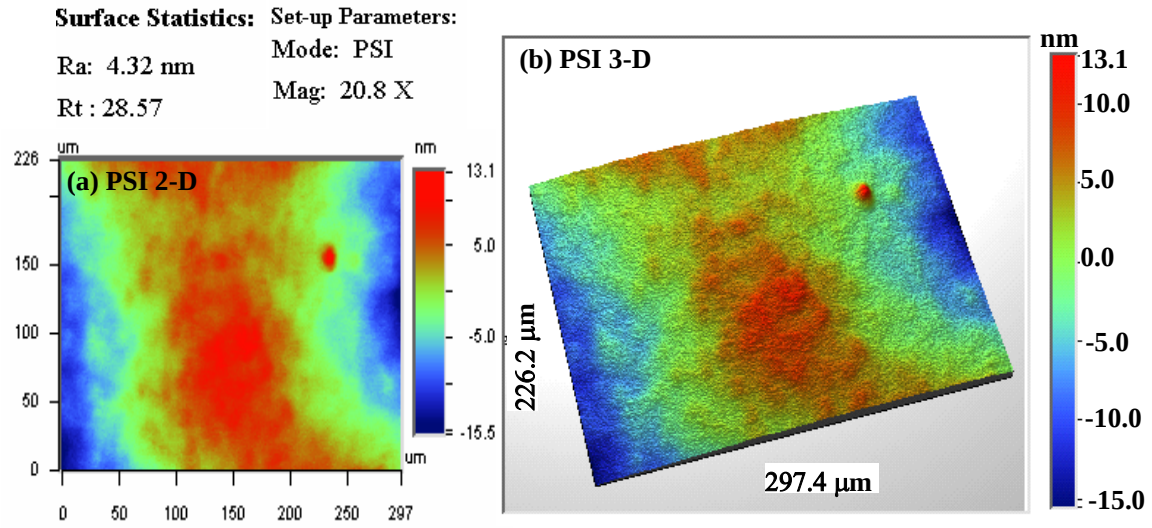

Figure 12. Typical surface roughness profile of smooth bond coat surface using PSI mode.

2.4 Degradation of Bond Coat

Aforementioned, YSZ topcoat of TBCs provides a thermal barrier, but it does not stop underlying bond coats from oxidation, because it is a fast oxygen-ion conductor at high temperatures. As a result, during service, the thermally grown oxide (TGO) scale grows at the interface between the bond coat and the YSZ topcoat. Moreover, the pre-heat treatment prior to the YSZ deposition, and O_2 introduced during EB-PVD to maintain proper oxygen stoichiometry also oxidizes the bond coat. The formation and growth of Al_2O_3-TGO scale generally depletes Al from the bond coat. If Al depletion is severe, it is possible to form other oxides, such as Ni-, Cr- and Co-rich oxide, including NiO, Cr_2O_3, CoO, and spinels such as $(Ni,Co)(Al,Cr)_2O_4$ with low fracture toughness.[12,68] In addition, excessive alloying of Yttrium can result in the formation of $Y_3Al_5O_{12}$ (yttria-alumina garnet YAG) and/or Y_2O_3, and degrade the adhesion between the TGO and bond coat as shown in Fig. 13.[69]

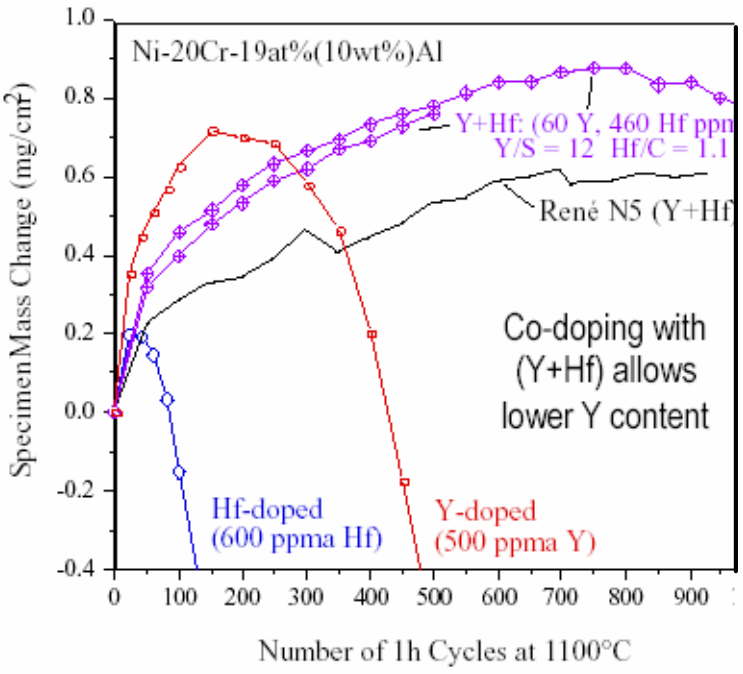

Figure 13. Effects of minor element additions on the high-temperature oxidation behavior of Ni-base alumina-forming alloys.

2.5 Characterization of the TGO Scale

2.5.1 Stress within the TGO Scale

Failure of TBC systems is typically associated with spallation at the TGO/bond coat interface, and/or within the TGO, and/or at the YSZ/TGO interface. Accordingly, the adhesion of the TGO layer and residual stress within the TGO scale exert a central influence on the damage mechanisms and spallation failure of TBCs.

The α-Al_2O_3 is a preferred constituent of the TGO scale, because of its low oxygen diffusivity and superior adhesion to the metallic bond coat surface. The TGO consisting of α-Al_2O_3 develops extremely large residual compressions because of its thermal expansion misfit with the substrate upon cooling (2~6 GPa),[70,71] as listed in Tab. 1 and its growth due to constrained volume expansion (< 1GPa).[51,72,73,74,75] The phase transformations of metastable phases, and the bond coat surface roughness can also contribute to the residual stress in the TGO scale.[25,76,77]

Table 1. Summary of critical materials properties related to TBCs. [70,78]

TGO (α-Al_2O_3)	Young's modulus E_0 (GPa)		350-400
	Growth stress, σ^g_{xx} (GPa)		0-1
	Misfit compression, σ_0 (GPa)		3-4
	Mode I fracture toughness, Γ_0 (J m^{-2})		20
	Thermal expansion coefficient, α_0 (C^{-1} ppm)		8-9
Bond coat	Young's modulus E_S (GPa)		200
	Yield strength(ambient temperature) σ_Y (MPa)		300-900
	Thermal expansion coefficient, α_S (C^{-1} ppm)		13-16
Interface (α-Al_2O_3/ bond coat)	Mode I adhesion energy, Γ^0_1(J m^{-2})	Segregated	5-20
		Clean	>100
TBC (ZrO_2/Y_2O_3)	Thermal expansion coefficient, α_{TBC} (C^{-1} ppm)		11-13
	Young's modulus E_{TBC} (GPa)		0-100
	Delamination toughness Γ_{TBC} (J m^{-2})		1-100

2.5.2 Phase Constituents of the TGO Scale

The Al_2O_3, the primary constituent of the TGO scale has various polymorphs. For instance, the equilibrium α-Al_2O_3, metastable θ-Al_2O_3, and metastable γ-Al_2O_3 have been observed within the TGO.[21,22] Tab. 2 list the various polymorphs of Al_2O_3.

Table 2. Different polymorphs of Al_2O_3.

Phase	System	Structure Type	Lattice Parameter (Å)			c/a, α or β	Space group
			a	b	c		
α	hexagonal	/	4.76	/	12.99	/	$R\bar{3}c$
γ	cubic	Spinel with vacancies	7.86	/	/	/	Fd3m
δ	tetragonal	/	7.95	/	7.79	0.98	/
γ'	cubic	f.c.c	9.36	/	/	/	/
η	hexagonal	/	9.71		17.86	1.84	/
θ	Monoclinic	/	11.24	5.72	11.74	β=103°20'	P6 or $P6_3$
χ	hexagonal	/	/	/	13.44	2.42	P6 or $P6_3$

Other oxides such as Ni-, Cr-, and Co-rich oxide, including NiO, Cr_2O_3, CoO, and spinels such as $(Ni,Co)(Al,Cr)_2O_4$ with low fracture toughness may be also present at the TGO scale due to severe degradation of the bond coat. $Y_3Al_5O_{12}$ (yttria-alumina garnet YAG) and/or Y_2O_3 may form within the TGO due to the excessive of alloying of Y in the bond coat.

Initial phase constituents of the TGO are also considered to be a critical factor influencing the integrity of TBCs. The formation of the metastable γ- and θ-Al_2O_3, and their transformations to the equilibrium α-Al_2O_3 in the TGO scale have been reported to have a profound effect on the structural integrity of TGO/YSZ interface during thermal cycles.[24, 79] These polymorphic transformations of Al_2O_3 may be responsible for additional residual stress from the volumetric constraint in the TGO, and nucleation of sub-critical defects, eventually leading to the spallation of the TGO. For example, there is about a 4.7% volume change for θ- to α-Al_2O_3 phase transformation. Thus, the formation of a uniform and defect-free α-Al_2O_3 scale prior to the deposition of topcoat can help to enhance the durability and reliability of TBCs.

2.5.3 Photo-Stimulated Luminescence Spectroscopy (PSLS)

Non-destructive method of monitoring the damage evolution that leads to the eventual failure is desirable for many engineering materials, including TBCs. Such a method could be used both as the basis of an inspection tool and as input for the development of quantitative models for predicting life-to-failure. One promising method is piezospectroscopy, which has been applied to measure the residual stresses in α-Al_2O_3 by Grabner in the 1970's.[80] Later, photo-stimulated luminescence spectroscopy (PSLS) was developed as a nondestructive inspection technique for the measurement of residual stresses and phase constituents within the TGO scale buried under the YSZ topcoat in

TBC system by Clarke et al.[81] Since the early 1990's,[70,82,83,] numerous studies involving PSLS and TBCs were carried out to refine this technique.[55,56,71,84,85,86]

The schematic diagram presented in Fig. 14 illustrates the principle by which PSLS probes the TGO underneath the YSZ topcoat. PSLS is an optical method that is based on the photon emission from Cr^{3+} impurity in the Al_2O_3 when excited by argon ion laser with a wavelength of 514nm, which is chosen to penetrate through the YSZ and yet be within the optical absorption band of the chromium-doped Al_2O_3. The reflected fluorescence signal is recorded. For stress-free α-Al_2O_3, two distinct fluorescence transitions, which are allowed by the crystallographic symmetry of the Cr^{3+} site in α-Al_2O_3 crystals, take place corresponding to the R_1 and R_2 fluorescence doublets shown as the dashed line in Fig. 15, occurring at frequencies of 14402 and 14432 cm^{-1}, respectively. If the oxide is stressed, the frequency of the Cr^{3+} luminescence shifts systematically (solid line in Fig. 15), $\Delta\nu$, so called piezospectroscopic effect. The frequency shift can be calibrated, and the resulting stress value in the α-Al_2O_3 scale can be determined based on the relation:[55,56,86,87,88]

$$\Delta\nu_{stress} = \Pi_{ij}\,\sigma_{ij}^{c} = \Pi_{ij}\,a_{ki}\,a_{lj}\,\sigma_{kl} \qquad (1)$$

where Π_{ij} is the *ij*th component of the piezospectroscopic tensor and σ_{ij}^{c} is the stress state in the crystallographic basis of the host crystal. In a general coordinate system, the stress state, σ_{ij}, is related to σ_{ij}^{c} by the transformation matrix a_{ij}.

When the Al_2O_3 is untextured and polycrystalline with small grain size (i.e., smaller than the probing volume), the frequency shift is proportional to the trace of the stress tensor, namely,

$$\Delta\bar{\nu} = \frac{1}{3}\Pi_{ii}\sigma_{jj} \tag{2}$$

For a thin alumina scale under biaxial stress, $\bar{\sigma}$, the frequency shift is related to the average residual stress by:

$$\Delta\bar{\upsilon} = \frac{2}{3}\Pi_{ii}\bar{\sigma} \tag{3}$$

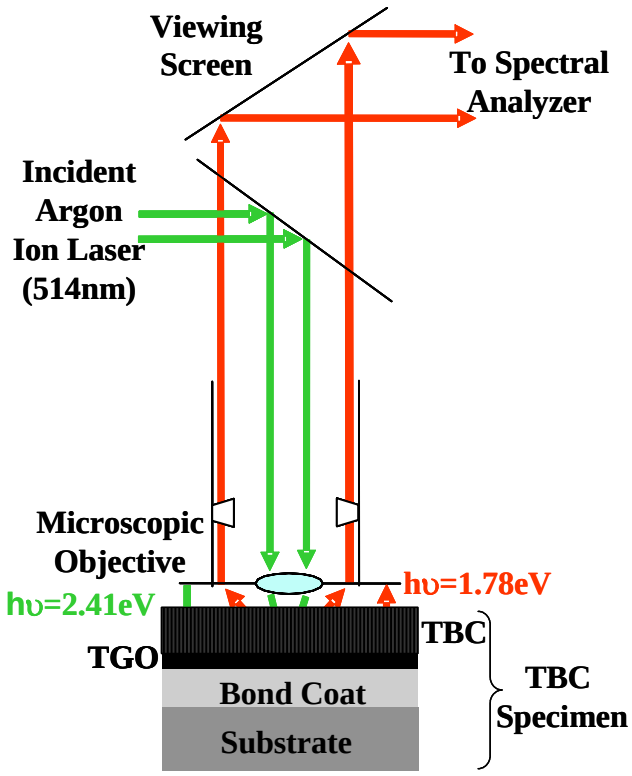

Figure 14. A schematic illustration of photo-stimulated luminescence spectroscopy technique.[89]

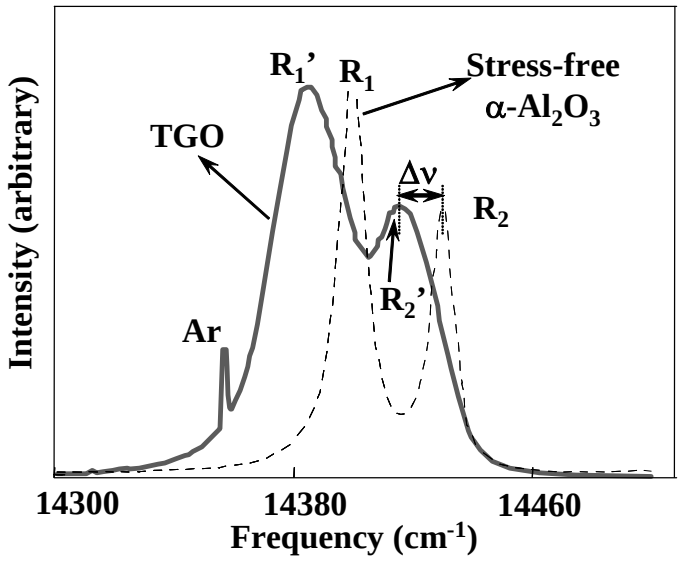

Figure 15. Typical PSLS spectra showing stress free and stressed α-Al_2O_3.

Besides residual stress, there are many other factors that affect the frequency and shape of the luminescence, including temperature and concentration of Cr^{3+} or other impurity ions. Assuming that these contributions are uncorrelated, their net effect on the frequency shift is simply additive:

$$\Delta\nu = \Delta\nu_{stress} + \Delta\nu_{temp.} + \Delta\nu_{conc.} \quad (4)$$

The temperature-induced fluorescence shift is described using a scalar factor, β:

$$\Delta\nu_{temp} = \beta(T)\, T \quad (5)$$

where the temperature dependence of β is empirically found to be insiginificant.[90] In practice, temperature contribution can be corrected by monitoring the temperature during acquisition of spectrum. The Cr^{3+} concentration dependence of the frequency shift has been previously established,[91] and varies as $\Delta\nu_{conc.} = 0.99C_m$, where C_m is the concentration of chromium in weight percent. When the Cr^{3+} is uniformly distributed across the sample, only the temperature and stress variations need to be accounted for. Moreover, the effect of doping ions addition to Cr^{3+} (e.g., Fe, Ti, Ni, or Y) has been investigated recently by Clarke *et. al*.[92] They found the ions that are soluble in α-Al_2O_3 will cause systematic changes in the luminescence frequency and intensity, whereas those ions that are insoluble have no effect on the R-line luminescence.

Besides the frequency shift, the peak shape, peak separation, peak width and peak intensity ratio are also considered to be related to the damage within the TGO.[55,84,93] The fluorescence is a particularly strong signal, and can be detected through rather thick EB-PVD topcoats due to their columnar microstructure, which do not significantly attenuate the optical signals. In contrast, for APS TBCs, porosity, grain boundaries, and most importantly splat boundaries tends to obstruct the observation of luminescence from α-Al_2O_3 through the topcoat.

PSLS not only can determine the residual stress within the α-Al_2O_3 scale, but also can identify Al_2O_3 polymorphs within the TGO scale. Fig. 16 shows, respectively, the N, Q, and G-luminescence arising from a significant Cr_2O_3 concentration in TGO,[94] the presence of metastable θ–Al_2O_3 which is characterized by a doublet at approximately 14575 and 14645 cm^{-1}, and γ-Al_2O_3 which is at about 14360 cm^{-1} within the TGO.[95]

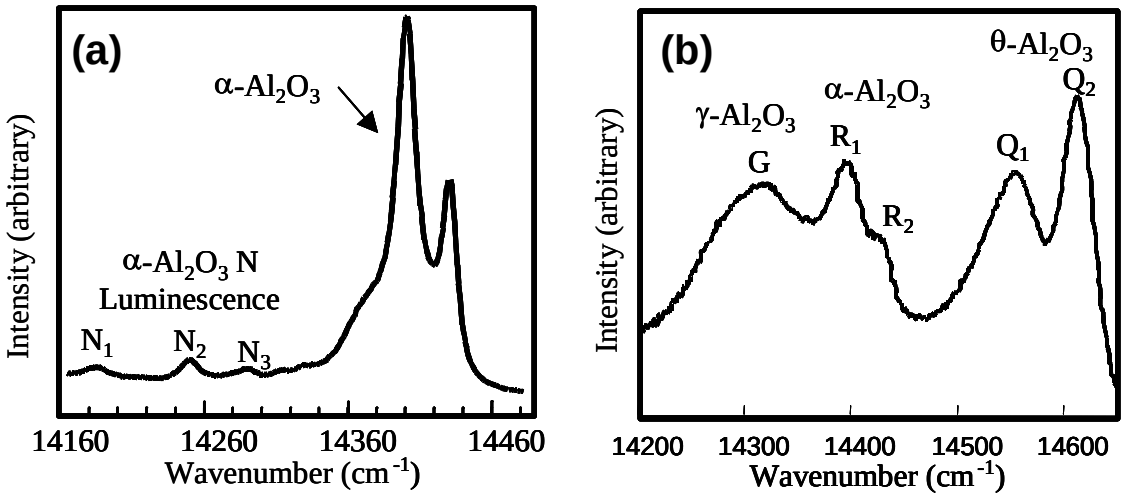

Figure 16. (a) N-type luminescence arising from the presence of significant Cr_2O_3 in α-Al_2O_3 scale; (b) Luminescence from γ, α and θ-Al_2O_3 labeled G, R_1-R_2 and Q_1-Q_2, respectively.[96]

2.5.4 Polymorphic Transformations of Al_2O_3 within the TGO

In general, metastable Al_2O_3 form at early stage of oxidation particularly at lower temperatures. Then, they transform into the equilibrium α-Al_2O_3. The rate of transformation depends on many factors including environment, temperature, bond coat surface finish, etc. For example, Fig. 17 shows the typical whisker microstructure of metastable γ-Al_2O_3 scale formed after oxidation at 788°C for 500 hours and that of transformed α-Al_2O_3 after oxidation at 954°C for 1000 hours.

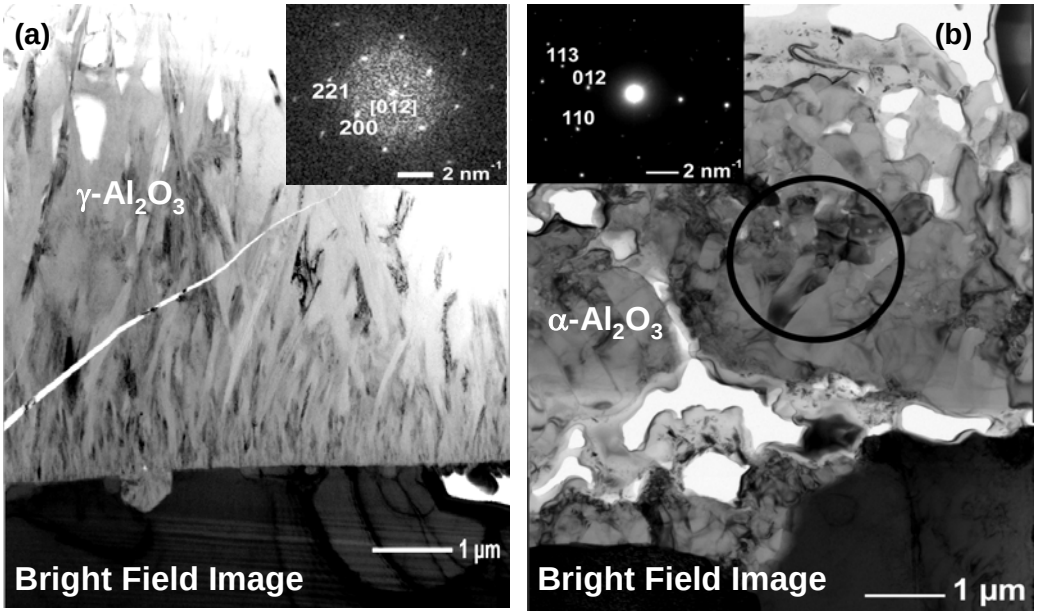

Figure 17. Bright field micrographs of (a) the metastable γ-Al_2O_3 scale formed after oxidation at 788°C for 500 hours; and (b) the equilibrium α-Al_2O_3 scale developed from (a) after 1000 hours' oxidation at 954°C.[97]

2.6 Failure Mechanisms of TBCs

During engine operation, several time- and cycle-dependent phenomena including rumpling, buckling, edge delamination and ratcheting take place within the TBC system, which can be associated with the spallation-failure.

2.6.1 Failure of EB-PVD TBCs

EB-PVD TBCs have columnar structures and are more "strain tolerant" than APS TBCs. Fracture paths occur primarily within the TGO, or at the YSZ/TGO interface or TGO/bond coat interface as schematically illustrated in Fig. 18.

- Path I – Figs. 18(a) and 18(b): Separation of the TGO/bond coat interface driven by out-of-plane stresses; tensile at the undulation crest and compressive at the troughs due to the bond coat surface roughness.[98] With further thermal cycling, TGO thickens and the magnitude of the tensile stress increases, cracking the TGO/bond coat interface at crest. For EB-PVD TBCs with relatively flat and defect-free interfaces, the compression in the TGO causes large-scale buckling at the TGO/bond coat interface, as shown in Fig. 18 (d).[57,99]
- Path II – Figs. 18(b) and 18(c): Separation of the YSZ/TGO interface and penetration of the TGO into the bond coat resulting from one or more of the following mechanisms: (1) progressive TGO roughening (rumpling) caused by bond coat cyclic creep as shown in Fig. 18 (b) and (c);[100,101] (2) accelerated growth of embedded oxides due to localized TGO cracking;[25,55,102] (3) cavity formation in the bond coat; (4) phase transformations of YSZ and TGO; and (5) formations of Ni/Co rich oxides (spinels) that are brittle in nature.
- Path III: Mixture of the above two. TBC fails at both interfaces of TGO/bond coat and YSZ/TGO.

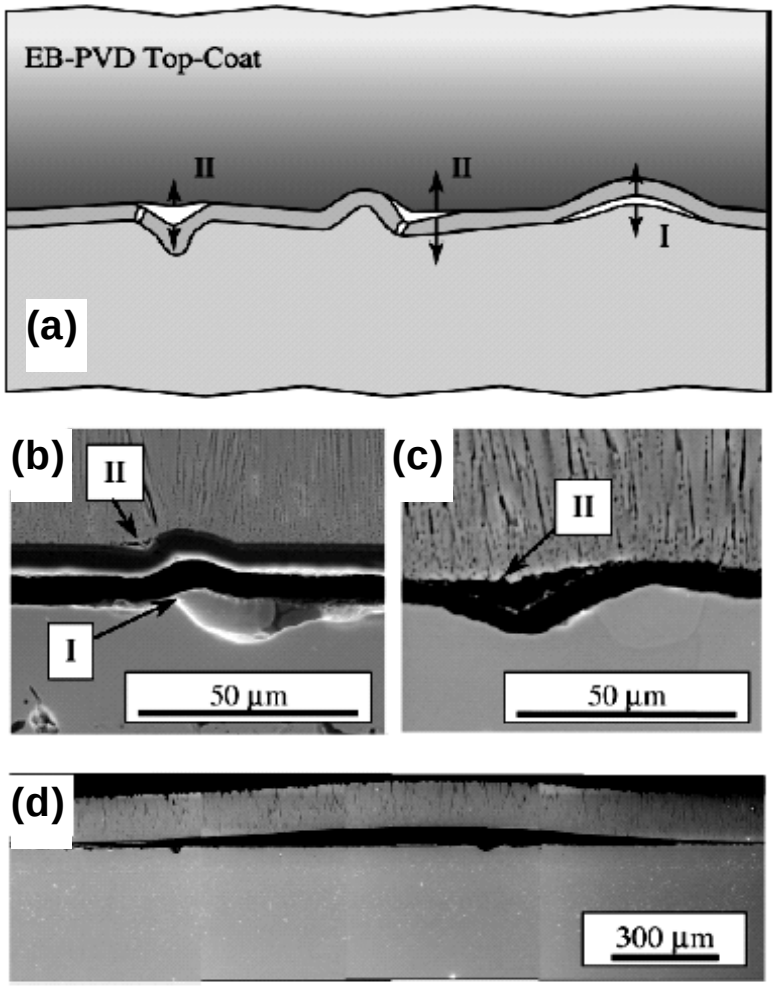

Figure 18. (a) A schematic diagram showing different cracking paths in EB-PVD TBC. Cross-sectional SEM images showing (b) path I and II (1917 cycles), (c) path II (376 cycles), and (d) large-scale buckling (1830 cycles) where bond-coat surface imperfections were eliminated before YSZ deposition.

2.6.2 Final Failure Modes

Rumpling has been commonly observed during cyclic oxidation of aluminide coatings on nickel-based superalloys as shown in Fig. 19.[109] This is due to the coating-substrate thermal expansion mismatch[103] or repeated oxide cracking and spallation[104].

TBCs with smooth bond coats usually spall by buckling over a rather large area as shown in Fig. 20. A number of distinctly separate buckles develop over a large number of cycles. The prerequisite for buckling is the development of a sufficiently large and contiguous debonded region. In general, the size of the debonded region needed for buckling increases with increasing oxide thickness. However, increase in oxide thickness alone does not lead directly to buckling spallation. As the strain energy release rate driving the delamination increases with increasing oxide thickness, the buckling tendency decreases. Therefore, only when the balance is met, that is to say, the thickness of the TGO has reached the critical size for buckling, TBCs will fail.[105,106,107]

Fig. 21 illustrates edge delamination of the TBCs, which initiates at the edge of the TGO/bond coat interface and competes with buckling, as influenced by the in-plane modulus of the top coat. Both forms of delamination scale have the available elastic energy stored in the layers. Usually, the low in-plane elastic moduli of the porous zirconia layer promote buckling, but suppress edge delamination. But the relatively thick top coat also acts to suppress buckling whenever the initial interface flaws are smaller than a critical size.[108]

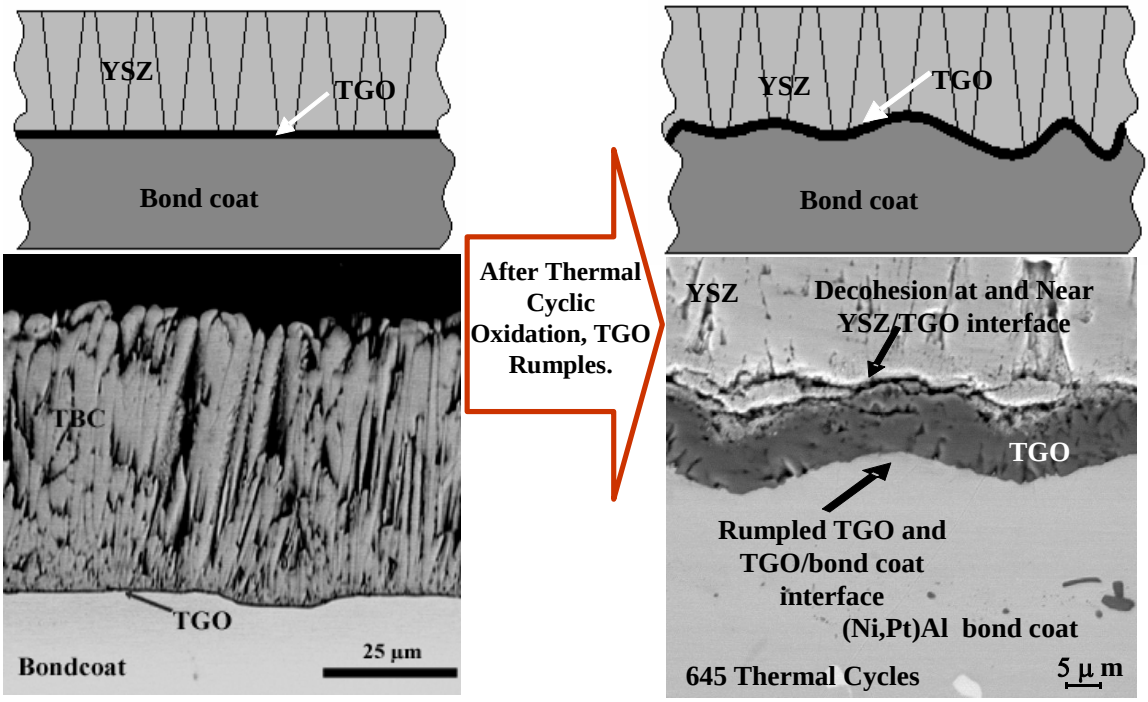

Figure 19. A schematic illustration and example micrograph of TGO rumpling after thermal cyclic oxidation.[109]

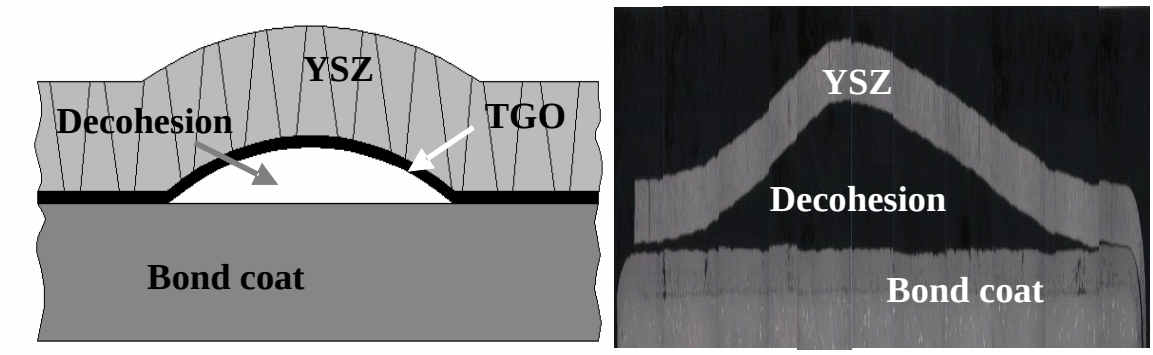

Figure 20. A schematic illustration and example micrograph of TBC failure by a large-scale buckling.

Fig. 22 shows a schematic illustration and an example micrograph of TBC failure by ratcheting. Two factors are required for ratcheting to occur. First, there must be some initial interface imperfections, which are above the critical amplitude to induce the stresses in excess of the cyclic yield strength of the bond coat. Secondly, due to the extreme yield strength anisotropy of β-NiAl, some grains adjacent to the TGO exhibit a soft orientation in the sense that they are highly susceptible to plastic deformation normal to the interface. This combination of orientation softness with interfacial imperfections dictates the ratcheting.[4]

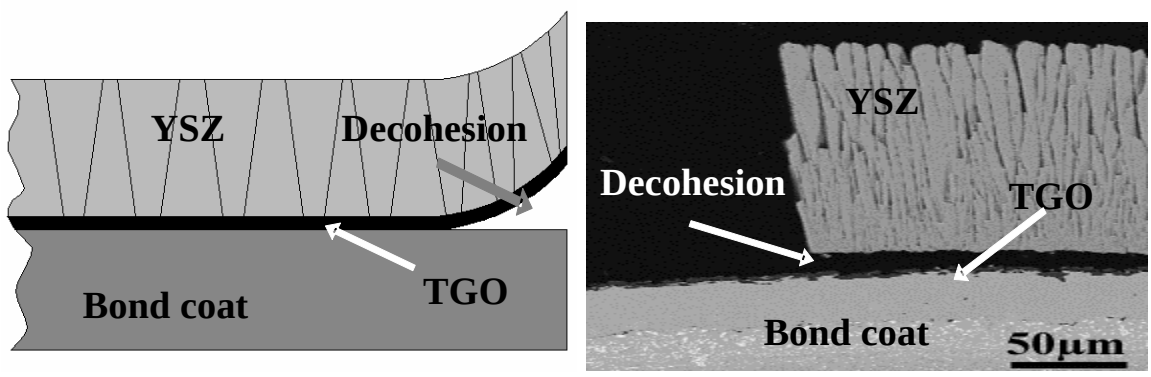

Figure 21. A schematic illustration and example micrograph of TBC failure by edge delamination.

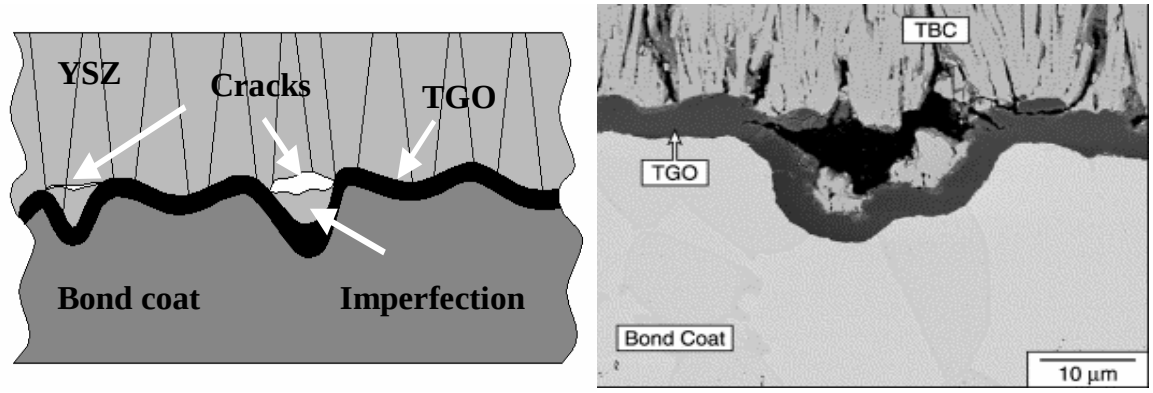

Figure 22. A schematic illustration and example micrograph of TBC failure by ratcheting.

2.6.3 Other Phenomena Related to TBC Failure

The following phenomena may also cause TBC failure:

1) Phase transformations in partially stabilized zirconia (PSZ) ceramic coatings: stress generated by the tetragonal-to-monoclinic phase transformation of PSZ coating is associated with the volume expansion (3-5%).
2) Formation of bond coat oxidation products other than Al_2O_3: formation of brittle spinel also can cause delamination of TBCs.
3) Sintering of the YSZ coating: Sintering increases the thermal conductivity and modulus of elasticity resulting in high metal surface temperature and enhancement of bond coat oxidation and creep. This results in stress-induced spallation at the interface between topcoat and the TGO. Such cases are reported in APS processed TBCs. [5]

4) Sulfur segregation at bond coat/TGO interface degrade the TGO adhesion. [46]
5) Cavity formation along bond coat grain boundaries. Cavity formation in the bond coat is inherent of the CVD aluminizing process. There is a ridge corresponding to each grain boundary in a large polygonal grain structure of platinum aluminized bond coat. The ridge transformed to a cavity partially filled with oxide as a result of cycle and time dependent process during the thermal cycling.[57] This is a cause of ratcheting.
6) Void formation along the TGO/ bond coat interface due to bond coat phase transformation.[110]
7) Foreign object damage (FOD) that locally compresses the TBCs, resulting in hot spots in the underlying bond coat that contribute to failure.[111,112]

3. EXPERIMENTAL PROCEDURE

3.1 Specimen Description

Twenty-six disk-shaped specimens of CMSX-4 superalloys coated with LPPS NiCoCrAlY bond coat and EB-PVD ZrO_2-7 wt.% Y_2O_3 (7YSZ) topcoat as schematically shown in Fig. 23 were employed in this study.

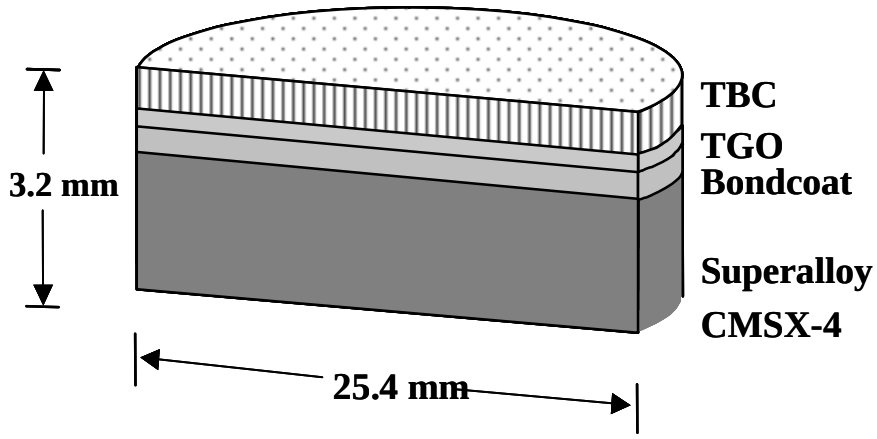

Figure 23. A schematic illustration of specimen geometry.

Various surface preparation and heat treatment were carried out before the deposition of the 7YSZ coatings as listed in Tab. 3. The bond coat surface can be categorized based on processing technique: as-sprayed (as low-pressure plasma sprayed), barrel-finished (media tumble treatment for 90-minutes) and hand-polished down to 0.25μm. Moreover, after each kind of the bond coat surface processing, selected

specimens were pre-oxidized in an oxidizing environment ($P_{O_2} \cong 10^{-8}$ atm) at 1100°C for 2-4 hours.

Table 3. Specimen descriptions according to surface preparation and pre-oxidation heat treatment prior to the 7YSZ deposition.

Surface Preparation	Pre-Oxidation[#]	Number of Specimens Tested
As-Sprayed*	No	4
	Yes	5
Hand-Polished[^]	No	2
	Yes	5
Barrel-Finished[+]	No	3
	Yes	7

* Surface finish as low pressure plasma sprayed.
^ Surface finish by metallographic polishing down to 0.25μm.
[#] Heat treatment in an oxidizing environment ($P_{O_2} \cong 10^{-8}$ atm) at 1100°C for 2-4 hours.
[+] Media tumble treatment for 90-minutes.

3.2 Experimental Flow

An experimental flow chart is shown in Fig. 24. Prior to the YSZ deposition, bond coat surface roughness and phase constituents within the oxide layer were examined by optical profilometry and PSLS, respectively, for specimens with and without pre-oxidation treatment. After the topcoat deposition, changes in the phase constituents of the TGO scale were examined by using PSLS. Then, thermal cycling test at 1121°C was carried out for all TBC specimens. During the test, specimens were periodically

withdrawn for PSLS measurements at room temperature to examine the residual stress and phase transformations within the TGO as a function of thermal cycles.

The specimens were considered to have failed when the YSZ spallation area was greater than 50%. Microstructure and phase constituents of the fracture surfaces (i.e., the top surface of the bondcoat and the bottom surface of the spalled YSZ) were analyzed by scanning electron microscopy (SEM) and energy dispersive spectroscopy (EDS). Also, FIB-INLO technique was employed for the preparation of TEM specimens with an emphasis on the TGO scale. TEM/STEM analysis included high angle annular dark field (HAADF) imaging, electron diffraction, and nano-EDS.

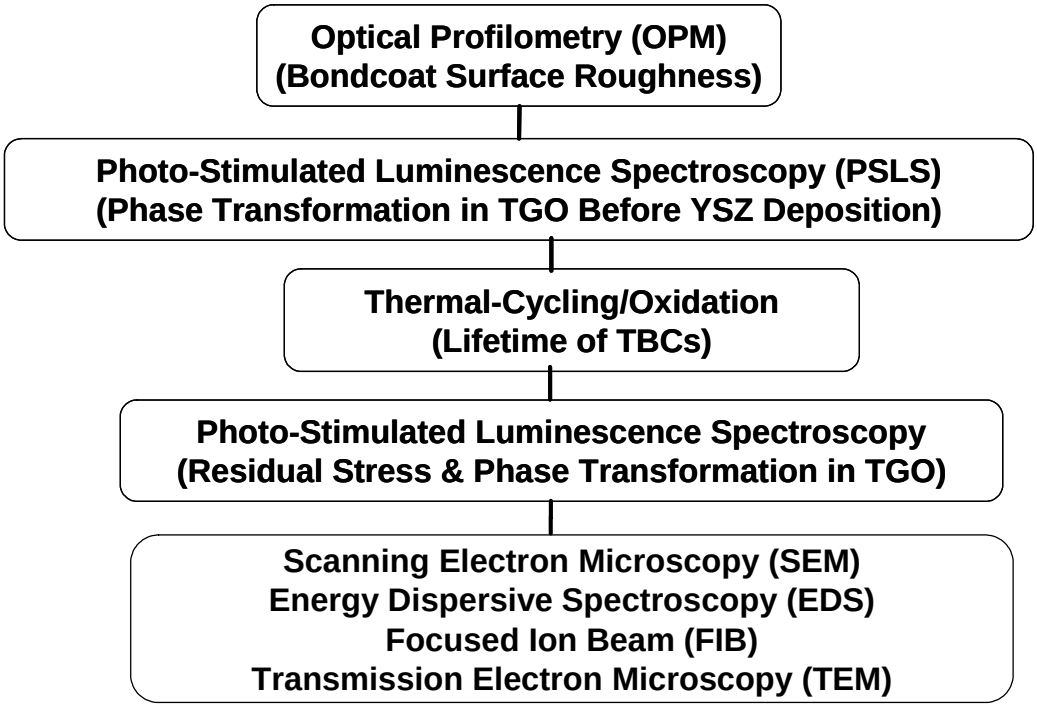

Figure 24. Experimental flow chart of this study.

3.2.1 Characterization of Bond Coat Surface before Ceramic Topcoat Deposition

Prior to the deposition of the YSZ coating by EB-PVD, surface roughness of the bond coat was evaluated by WYKO NT 3300 optical profilometry (OPM) with WYKO Vision 32 software to control the acquisition, analysis, storage and display of data collected with a WYKO optical interferometric microscope (OIM). The surface roughness of the bond coat is presented by R_a (average value) and R_q (RMS value of roughness) expressed by:

$$R_a = \frac{1}{n}\sum_{i=1}^{n} R_i \tag{6}$$

and

$$R_q = \sqrt{\sum_{i=1}^{n} R_i^2} \tag{7}$$

where R_i is the surface roughness of each lateral spatial sampling of 0.3 μm with vertical resolution of 3.0 nm. The value of peak to valley, R_t was also measured and examined. Each measurement made for this study contained approximately 1000 lateral spatial sampling.

For each sample, 10 random-spots covering an approximate area of $0.1mm^2$ were employed to determine the average values of R_a as the surface roughness of the specific specimen. R_q and R_t values were obtained similarly.

The residual stress and phase constituent within the oxide scale were examined by a Renishaw™, System 1000B Ramanscope™ (Renishaw™, Gloucestershire, UK) equipped with a Leica™ DM/LM optical microscope. In this study, an argon-ion laser (514nm) was used to photo-excite the R-line fluorescence at 693nm. PSLS spectra were collected from 20 randomly selected spots from both surfaces of specimens. (i.e. total 40 measurements for each specimen). The collected raw data was deconvoluted by curve-fitting, using a software package named Graphic Relational Array Management System (GRAMS). The R_1 and R_2 peak position, width and shape were simultaneously fitted to a mixed Gaussian and Lorentzian function. The intensity ratio of R_1 and R_2 peak should meet a criterion.[68] The phase constituents and the residual stress within the TGO scale as a function of processing and thermal cyclic oxidation was studied.

3.2.2 Thermal Cycling Test and PSLS

The lifetime of TBC specimens was determined by furnace thermal cycling test in air, which consists of repetition of 10-minute heat-up to 1121°C, 40-minute hold at 1121°C, followed by 10-minute force air-quench. The specimens were considered to have failed when the YSZ spallation area was greater than 50%. The samples were periodically withdrawn from the furnace to determine the residual stress in the TGO underneath the YSZ by PSLS at room temperature. At 0, 5, 25, 50, 75, 100 cycles and failure, PSLS measurements were carried out.

3.2.3 Microstructural Analysis

Microstructure and phase constituents of the TGO scale and the fracture surfaces (i.e., the top surface of the bond coat and the bottom surface of the spalled YSZ) were examined by optical microscopy (Nikon HFX-IIA), scanning electron microscopy (SEM) (JSM-6400F) and energy dispersive spectroscopy (EDS). Gold or platinum coatings were applied to the sample surface for conduction purpose prior to SEM.

For cross-sectional microstructural analysis, selected specimens were mounted in SPI-CHEM cold mount epoxy, sectioned using Isomet® low speed saw and polished down to 0.25μm.

In addition, focus ion beam (FIB) (FEI 200TEM) in-situ lift-out (INLO) technique was employed to prepare transmission electron microscopy (TEM) specimens. In FIB-INLO, a high-energy beam of focused Ga^+ is employed for imaging, milling and ion beam assisted CVD operations. The procedure for preparing a thin film for TEM analysis using FIB-INLO is shown in Fig. 25. A Pt line was deposited to protect the region of interest as shown in Fig. 25(a). After two trenches were cut below and above the Pt line, bottom was cut completely while parts of the sides were left attached as shown in Figs. 25(b), (c) and (d). Then, the W-needle, welded to the specimen, picked up the section, and placed the specimen on the C-shape copper grid shown in Figs. 21(e) to (j). The specimen section was further thinned to the final thickness of less than 100nm, suitable for TEM/STEM analysis, as shown in Figs. 21(k) and (l).[113,114]

TEM using FEI/Tecnai™ F30 300keV TEM, equipped with a Fischione ™ high angle annular dark field (HAADF) detector and EDAX X-ray energy dispersive

spectroscopy (XEDS) was carried out in this study for detailed microstructure analysis of TBCs after the thermal cycling test with an emphasis on the TGO scale.

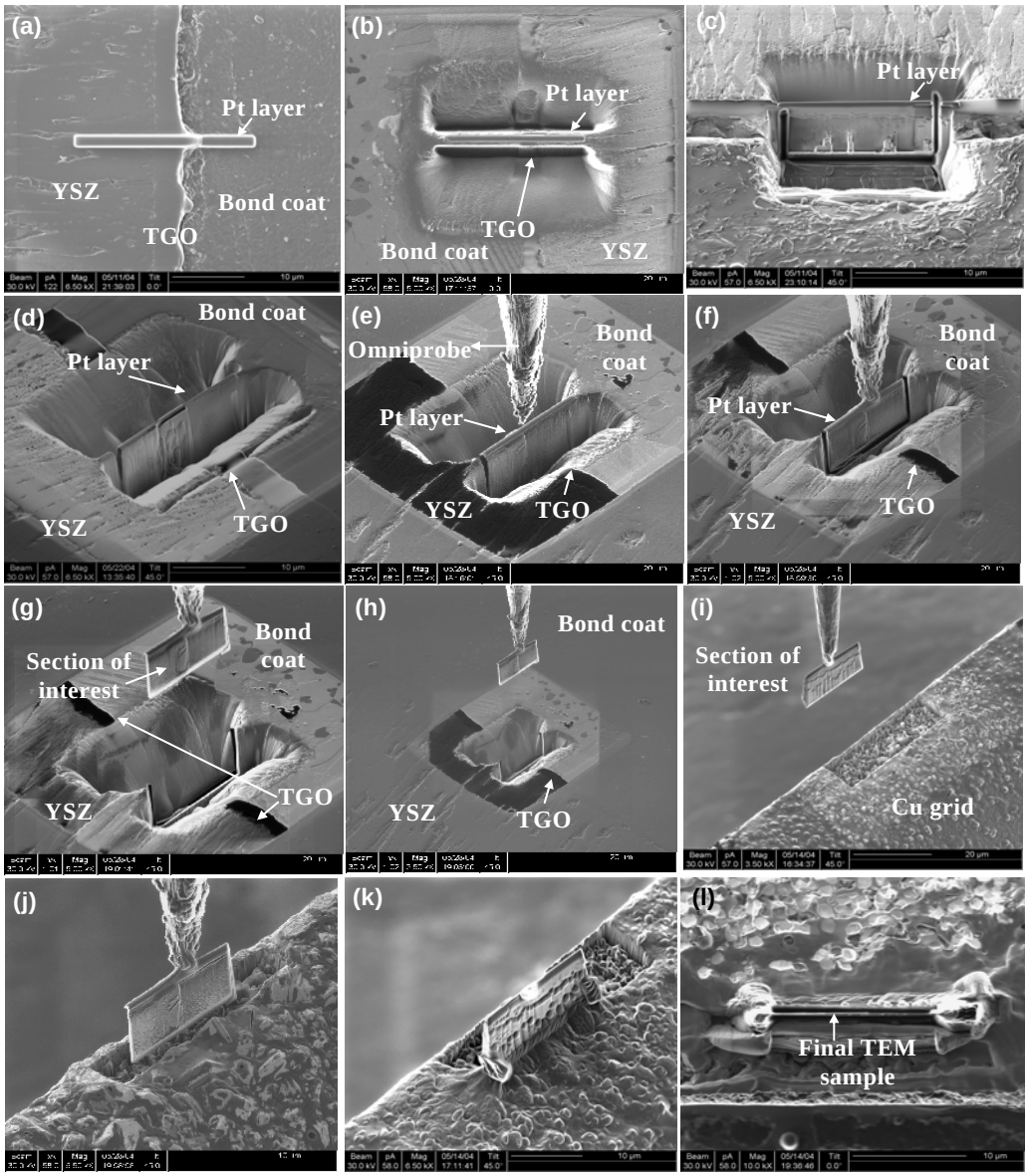

Figure 25. Procedure of FIB in-situ lift-out (INLO) technique for TEM specimen preparation. (a) top view of Pt layer protecting the section of interest (SOI); (b) two trenches were cut on both sides of the Pt layer ; (c) bottom and side cut of the section; (d) rotating to relatively 135 degree and tilted to absolutely 45 degree angle of (c); (e) the omniprobe was brought in; (f) SOI was attached to the omniprobe; (g) SOI was detached completely from bulk sample; (h) SOI was brought out by the omniprobe; (i) SOI was brought to the C-shape copper grid; (j) SOI was attached to the grid; (k) SOI was detached with the omniprobe; (l) final TEM specimen with a thickness of less than 80 nm.

4. RESULTS

4.1 Initial MCrAlY Bond Coat Surface and TGO Characterizations

Since surface preparation of the bond coat, the residual stress of the TGO scale and the phase constituents of the TGO scale are of prime importance and interest in this study, they were examined prior to and after the YSZ deposition, and later correlated to the furnace cycling lifetime of TBCs.

4.1.1 Surface Roughness of Bond Coat Before and After Pre-Oxidation

The surface roughness of the NiCoCrAlY bond coat measured before the EB-PVD is presented in Tab. 4, and in Figs. 26, 27 and 28 using the values of R_a, R_q and R_t. Typical OPM profiles are also presented in Figs. 29, 30, 31, 32, and 33. These results clearly demonstrate that the as-sprayed bond coats have the highest roughness, followed by the barrel-finished and the hand-polished. It is also evident that the roughness of the surface increases after the pre-oxidation heat treatment for hand-polished and barrel-finished bond coats. This roughening phenomenon for hand-polished specimens was quite significant that the measurement mode of OPM had to be changed from PSI to VSI as shown in Figs. 32 and 33.

Table 4. Bond coat surface roughness, R_a, R_q and R_t, of the specimens with and without pre-oxidation.

Bond coat surface preparation	Pre-oxidation	Bond coat surface roughness (R_a, nm)		Bond coat surface roughness (R_q, nm)		Bond coat surface roughness (R_t, nm)	
		Average	St. Dev.	Average	St. Dev.	Average	St. Dev.
As-sprayed	No	1321.3	601.6	1620	690.9	31474.0	658.9
	Yes	1321.3	601.6	1620	690.9	31474.0	658.9
Hand-polished	No	4.32	8.42	6.12	4.12	42.0	21.8
	Yes	302.6	21.1	368.9	25.6	3865.0	1298.7
Barrel-finished	No	320.1	10.3	426.6	17.4	26397.7	1186.2
	Yes	491.2	22.9	846.7	36.2	30257.7	173.2

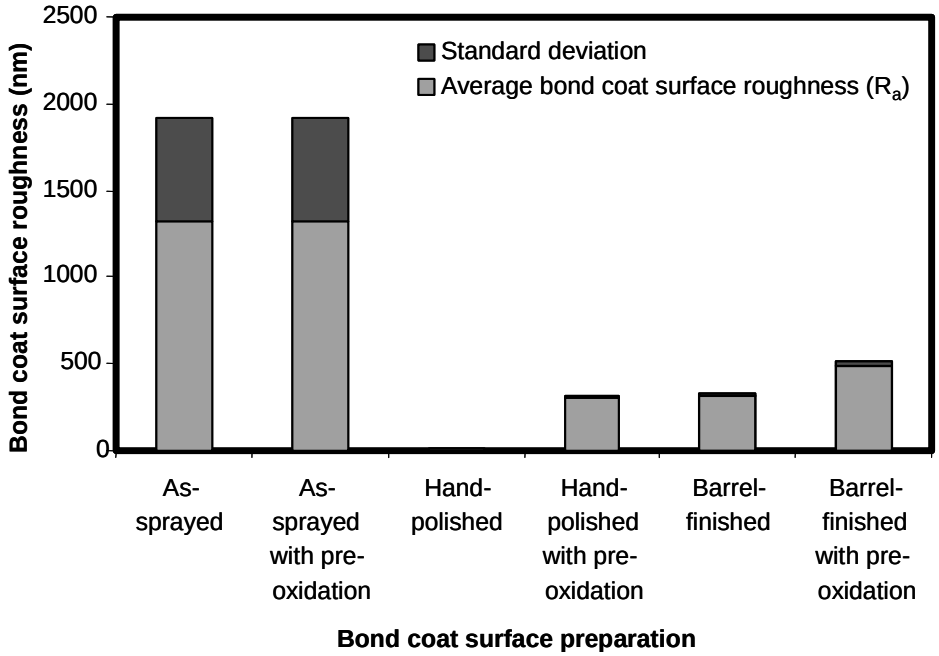

Figure 26. Average surface roughness, R_a of the bond coats as a function of surface preparation.

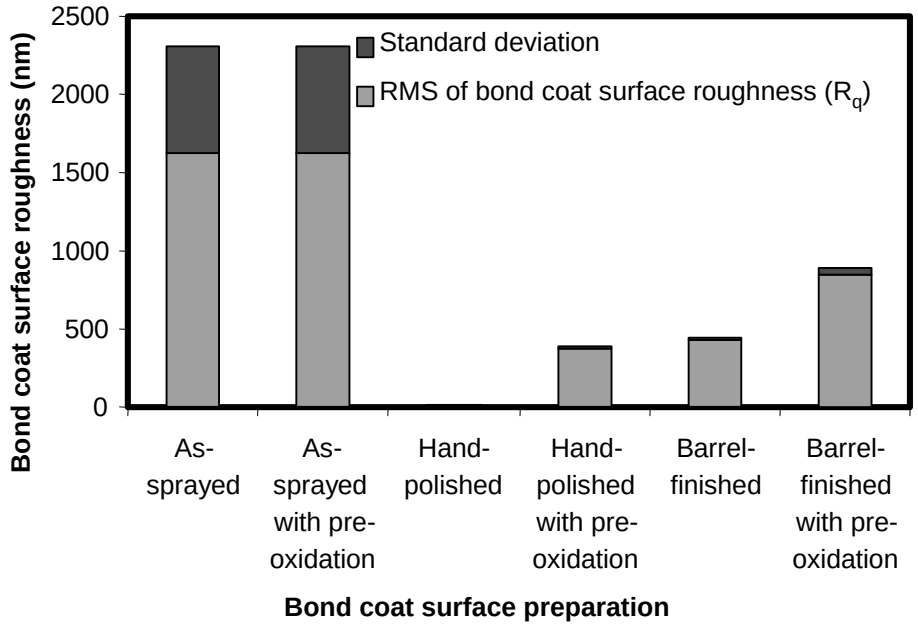

Figure 27. Root mean square surface roughness, R_q of the bond coats as a function of surface preparation.

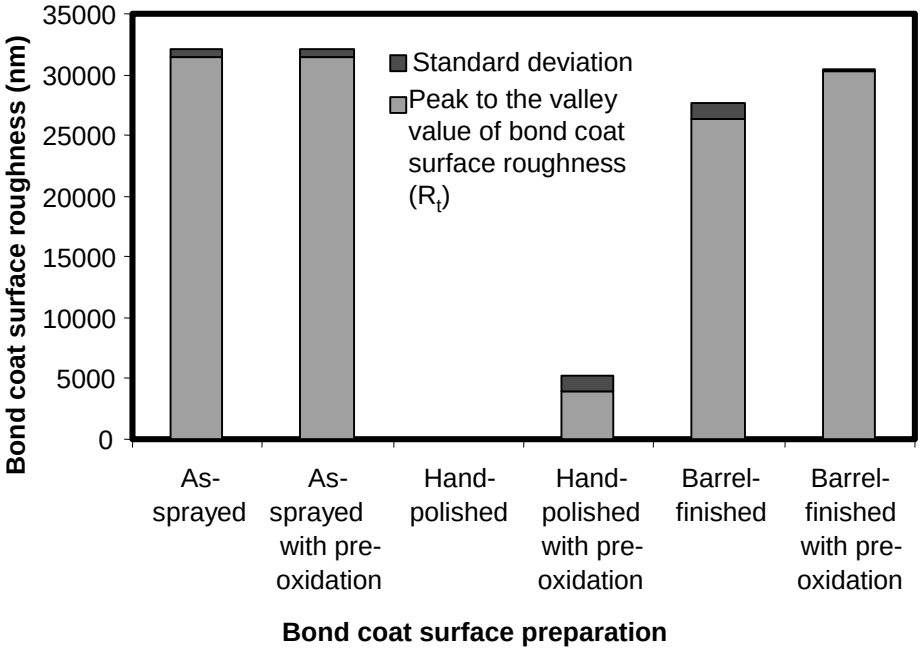

Figure 28. Peak to valley surface roughness, R_t of the bond coats as a function of surface preparation.

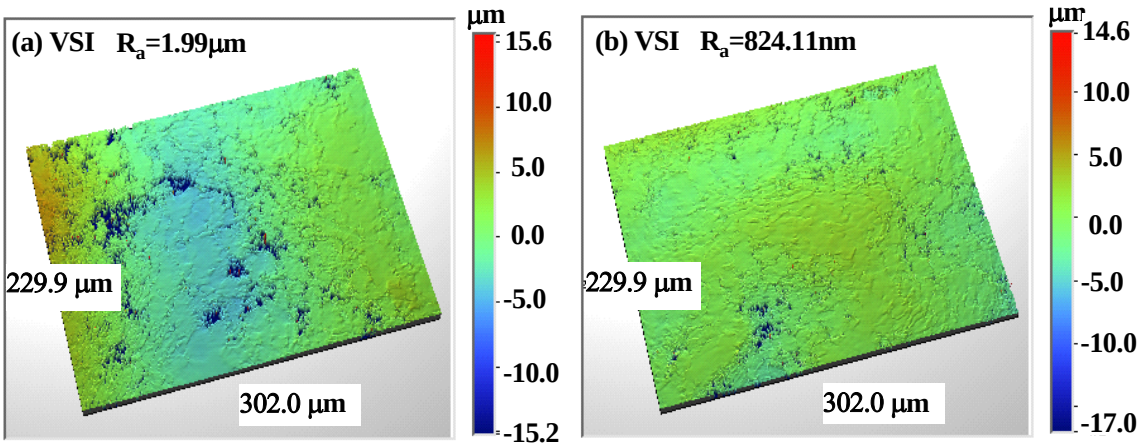

Figure 29. Typical surface roughness of the as-sprayed bond coat without the pre-oxidation treatment.

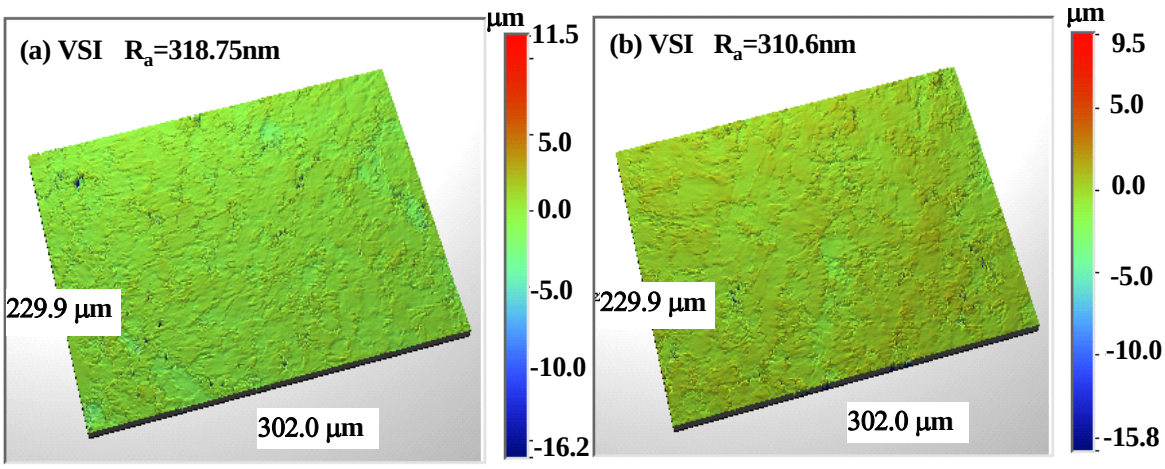

Figure 30. Typical surface roughness of the barrel-finished bond coat without the pre-oxidation treatment.

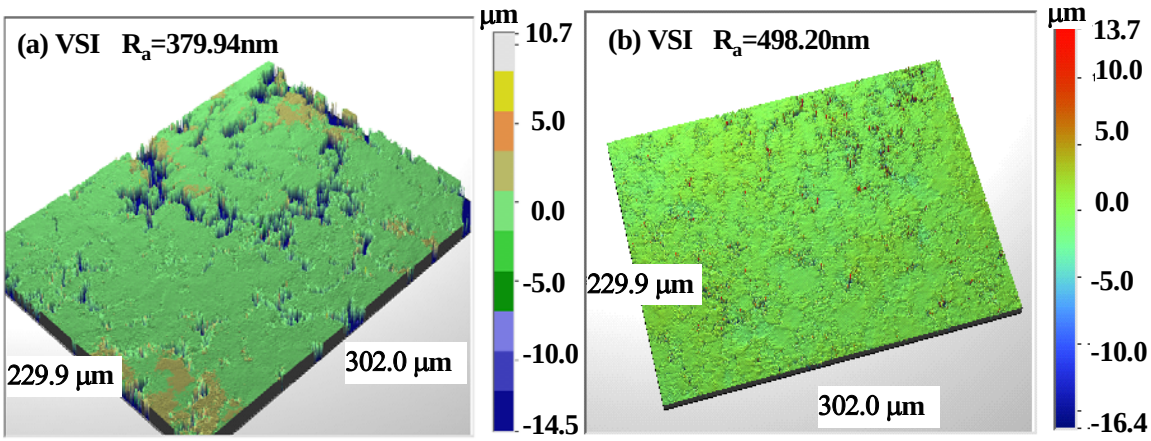

Figure 31. Typical surface roughness of barrel-finished bond coat with the pre-oxidation treatment.

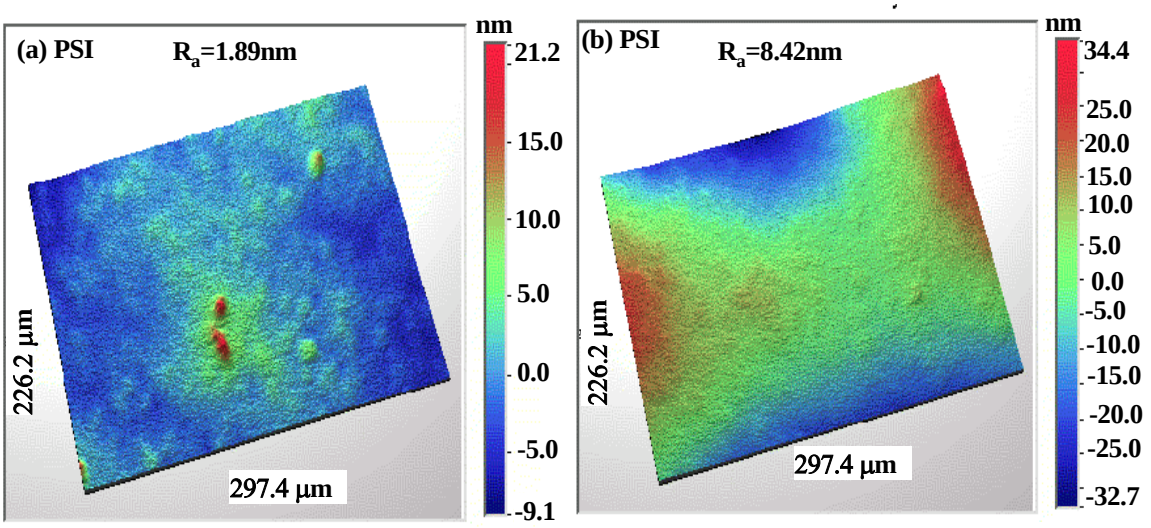

Figure 32. Typical surface roughness of hand-polished bond coat without the pre-oxidation, using PSI mode.

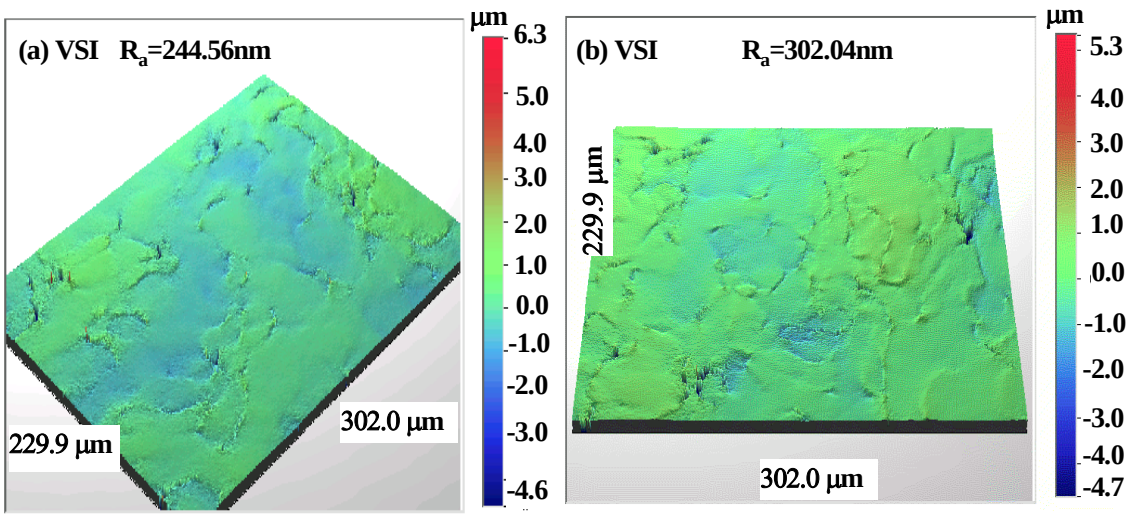

Figure 33. Typical surface roughness of the hand-polished bond coat with the pre-oxidation, using VSI mode.

4.1.2 Initial Phase Constituent of the Al_2O_3 Scale underneath the YSZ Coatings

The presence of various Al_2O_3 polymorphs can be identified using PSLS, as introduced before. Prior to the YSZ deposition by EB-PVD, no observable TGO was detected by optical microscopy and PSLS. Therefore, the initial phase constituents of the Al_2O_3 scale were examined only after the YSZ deposition. Figs. 34, 35 and 36 represent typical luminescence spectra obtained from the TGO scale developed on the as-sprayed, barrel-finished and hand-polished bond coats. No significant luminescence from the TGO scale was observed for TBCs with hand-polished bond coat that was produced without any pre-oxidation heat treatment. In general, luminescence from the metastable Al_2O_3 phases, labeled m_1 and m_2, was observed from all TBC specimens. The m_1 and m_2 luminescence may correspond to γ- and θ-Al_2O_3. The relative intensity of luminescence from the equilibrium R_1 and R_2, and the metastable m_1 and m_2, was determined as

reported in Tabs. 5, 6 and 7. These values indicate that the pre-oxidation heat treatment gives rise to greater presence of α-Al_2O_3 in the scale after the YSZ deposition.

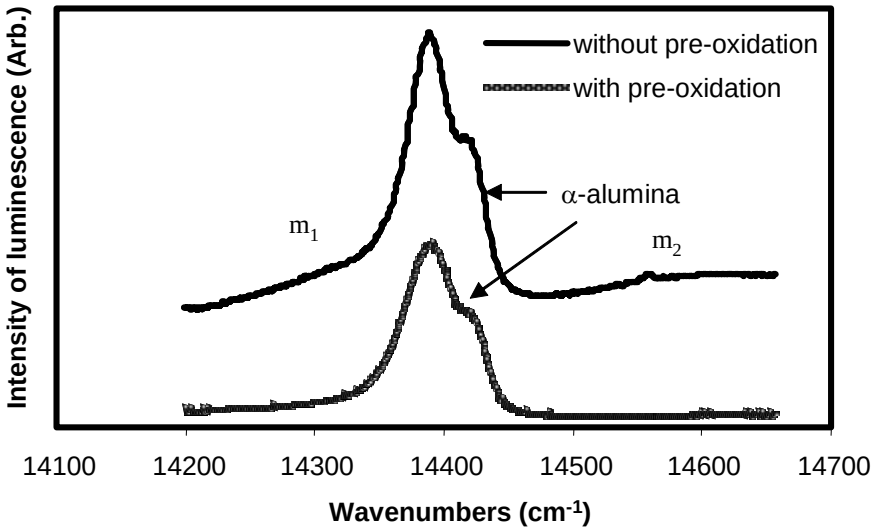

Figure 34. PSLS spectra from the TGO scale developed on the TBC specimen with as-sprayed bond coats with and without pre-oxidation.

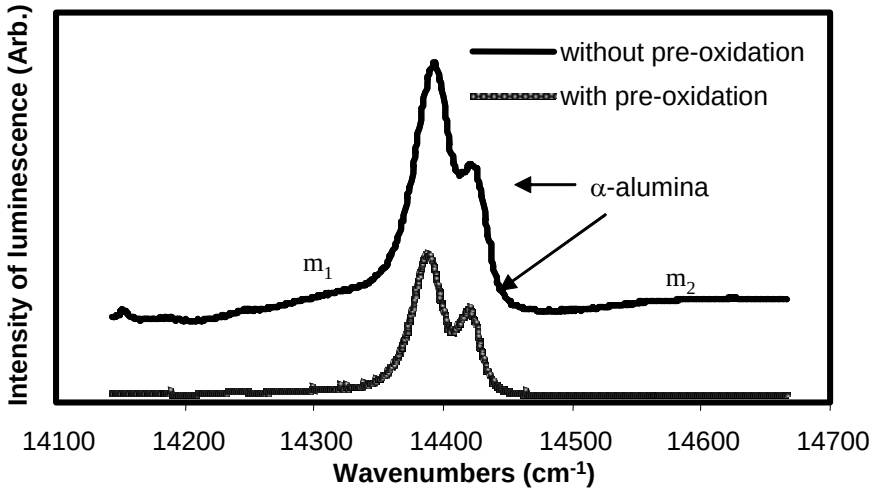

Figure 35. PSLS spectra from the TGO scale developed on the TBC specimen with barrel-finished bond coats with and without pre-oxidation.

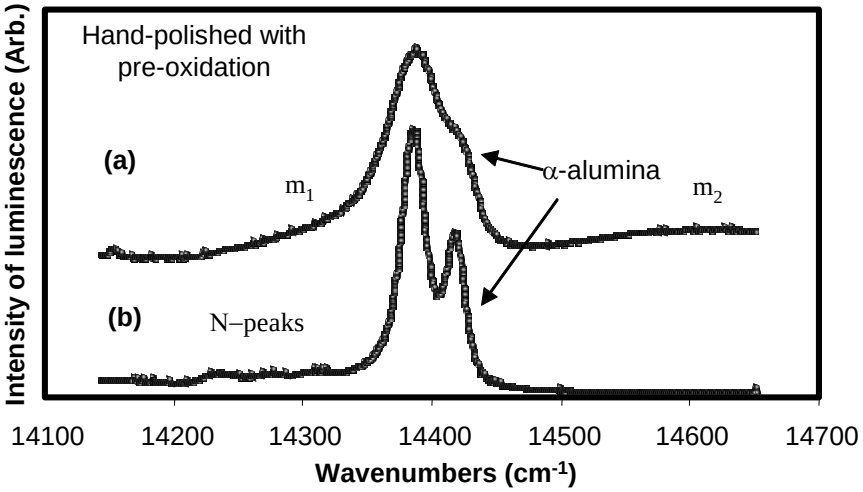

Figure 36. PSLS spectra from the TGO scale developed on the TBC specimen with hand-polished bond coats only with pre-oxidation.

Table 5. Luminescence intensity ratio of Al_2O_3 polymorphs to the total luminescence intensity from the TGO scale developed on the TBC specimen with as-sprayed bond coats.

Intensity ratio of different alumina phases to the total intensity	Without pre-oxidation		With pre-oxidation	
	Average	Standard Deviation	Average	Standard Deviation
I_α/I_{total}	0.57	0.01	0.69	0.04
I_{m_1}/I_{total}	0.23	0.01	0.20	0.03
I_{m_2}/I_{total}	0.20	0.02	0.11	0.04

Table 6. Luminescence intensity ratio of Al_2O_3 polymorphs to the total luminescence intensity from the TGO scale developed on the TBC specimen with barrel-finished bond coats.

Intensity ratio of different alumina phases to the total intensity	Without pre-oxidation		With pre-oxidation	
	Average	Standard Deviation	Average	Standard Deviation
I_α/I_{total}	0.61	0.03	0.66	0.06
I_{m_1}/I_{total}	0.19	0.02	0.18	0.01
I_{m_2}/I_{total}	0.20	0.03	0.16	0.04

Table 7. Luminescence intensity ratio of Al_2O_3 polymorphs to the total luminescence intensity from the TGO scale developed on the TBC specimen with hand-polished bond coats.

Intensity ratio of different alumina phases to the total intensity	Without pre-oxidation	With pre-oxidation	
		Average	Standard Deviation
I_{α}/I_{total}	Not detectable	0.72	0.03
I_{m_1}/I_{total}	Not detectable	0.16	0.02
I_{m_2}/I_{total}	Not detectable	0.12	0.02

4.2 Lifetime of TBCs

4.2.1 TBCs without Pre-Oxidation

The average thermal cycling lifetime of TBC specimens as a function of bond coat surface preparation (i.e., as-sprayed, hand-polished and barrel-finished) is presented in Tab. 8 and Fig. 37. These TBC specimens were produced without any pre-oxidation. TBC specimens with as-sprayed bond coats have the longest lifetime. The hand-polished specimens failed before any thermal cyclic test (e.g., failure out of the EB-PVD coater).

Table 8. Average thermal cycling lifetime of TBCs without any pre-oxidation heat treatment as a function of bond coat surface preparation.

Bond coat surface preparation	No. of specimen tested	Average lifetime (cycles)	Standard deviation
As-sprayed	4	87.5	25.0
Hand-polished	2	0	0
Barrel-finished	3	25.0	22.9

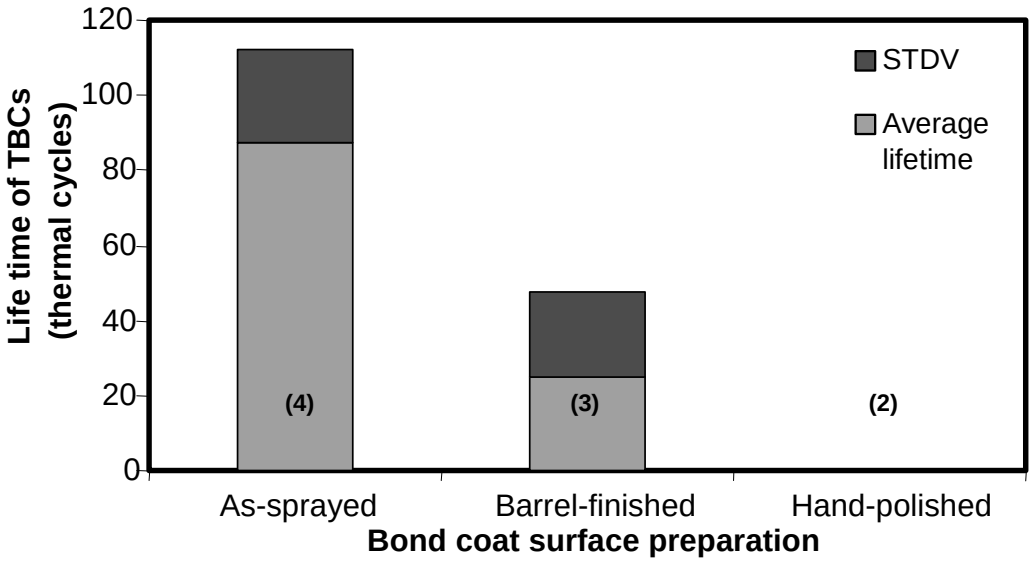

Figure 37. Average thermal cycling lifetime of TBCs without any pre-oxidation heat treatment as a function of bond coat surface preparation. (Numbers in the parentheses refer to the numbers of specimen tested.)

4.2.2 TBCs with Pre-Oxidation

The average thermal cycling lifetime of TBC specimens as a function of bond coat surface preparation (i.e., as-sprayed, hand-polished and barrel-finished) is presented in Tab. 9 and Fig. 38. These TBC specimens were produced with pre-oxidation. The TBC specimens with as-sprayed bond coats still have the longest lifetime, followed by specimens with hand-polished and barrel-finished bond coats. Smaller standard deviation in lifetime was observed with longer lifetimes. In addition, lifetime of all TBCs increased after pre-oxidation as presented in Fig. 39. The most significant improvement in TBC lifetime was observed for specimens with hand-polished bond coats that were pre-oxidized prior to the EB-PVD of 7YSZ.

Table 9. Average thermal cycling lifetime of TBCs with pre-oxidation heat treatment as a function of bond coat surface preparation.

Bond coat surface preparation	No. of specimens tested	Average lifetime (cycles)	Standard deviation
As-sprayed	3	101.7	2.9
Hand-polished	4	95.0	18.0
Barrel-finished	2	50.0	35.4

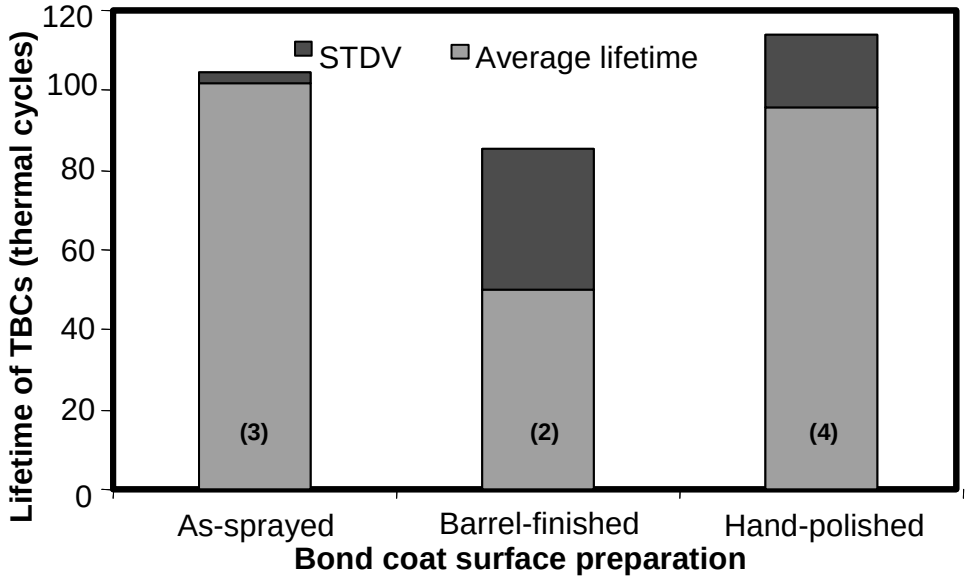

Figure 38. Average thermal cycling lifetime of TBCs with pre-oxidation heat treatment as a function of bond coat surface preparation. (Numbers in the parentheses refer to the numbers of specimen tested.)

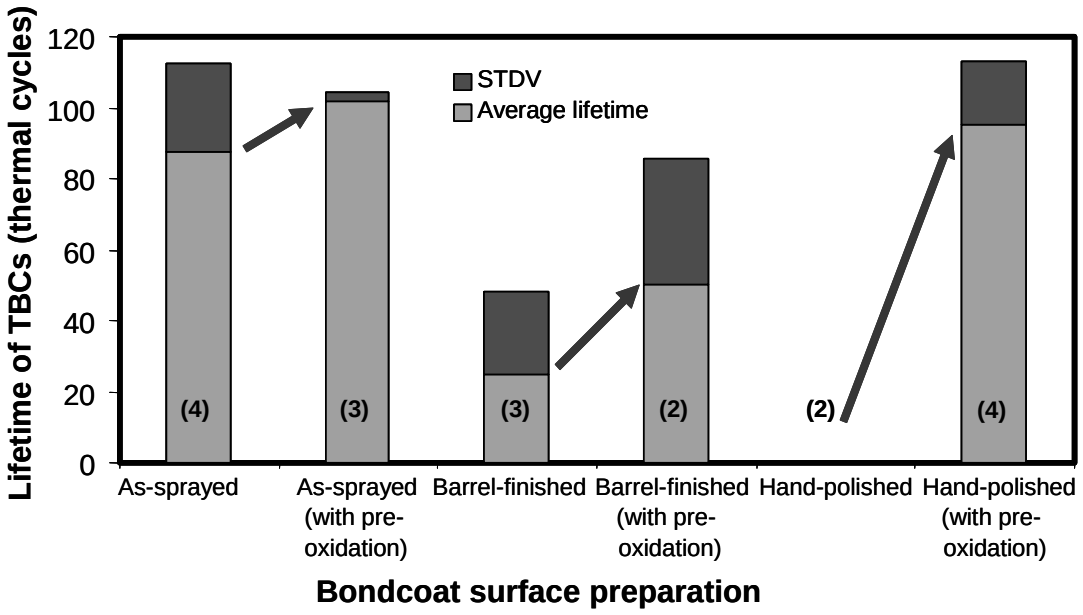

Figure 39. Lifetime of TBCs as a function of bond coat surface preparation and pre-oxidation. (Numbers in the parentheses refer to the numbers of specimen tested.)

4.3 Evolution of Phase Constituents in the Al_2O_3 Scale

After a few thermal cycles, all luminescence from the metastable phase observed by PSLS disappeared as typically shown in Fig. 40. Therefore, it is confirmed that the luminescence peaks other than those from α-Al_2O_3 obtained before thermal cycling are due to the metastable Al_2O_3 polymorphs.

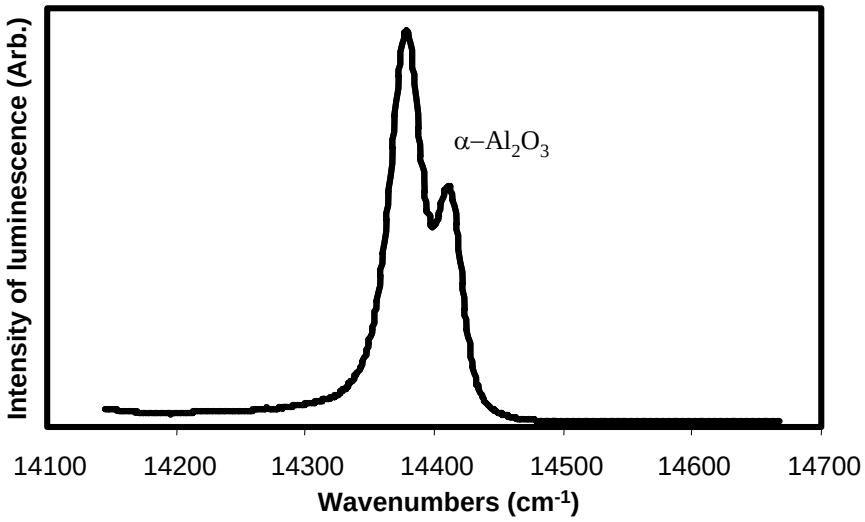

Figure 40. Typical PSLS spectrum for all specimens after a few thermal cycles at 1121°C.

4.4 Evolution of Residual Stress in the α-Al_2O_3 Scale during Thermal Cycling

4.4.1 TBCs without Pre-Oxidation

Tab. 10 and Fig. 41 present the magnitude of compressive residual stress in the α-Al_2O_3 scale as a function of thermal cycle for TBCs produced without any pre-oxidation heat treatment. The magnitude of initial compressive residual stress is higher for TBCs with as-sprayed bond coat, and lower for the TBCs with barrel-finished bond coat. However, during the thermal cycling test, the compressive residual stress in the α-Al_2O_3 scale increased rapidly for TBCs with barrel-finished bond coats after 5 cycles.

Table 10. Compressive residual stress in α-Al_2O_3 scale for TBC specimens without pre-oxidation.

Bond coat	Compressive residual stress in α-Al_2O_3 for TBCs without pre-oxidation (GPa)						
	No. of thermal cycles	0	5	25	50	75	100
As-sprayed	Average	1.87	3.27	3.77	3.56	3.89	3.66
	St. Dev.	0.62	0.65	0.40	0.76	0.29	0.86
Barrel-finished	Average	1.78	3.58	4.12	Failure	-	-
	St. Dev.	0.39	0.20	0.23	-	-	-

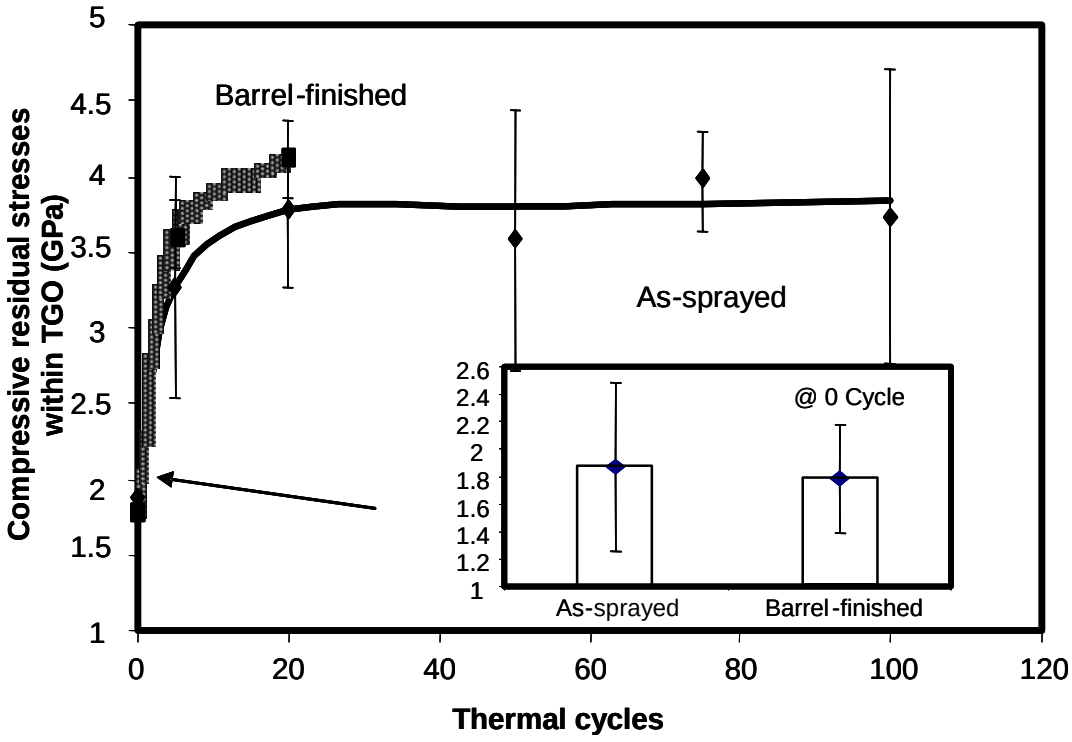

Figure 41. Compressive residual stresses in the α-Al_2O_3 scale for TBCs as a function of thermal cycle. The bond coats for these TBCs were not pre-oxidized.

4.4.2 TBCs with Pre-Oxidation

Tab. 11 and Fig. 42 present the compressive residual stress in α-Al_2O_3 scale of TBCs with pre-oxidized bond coats as a function of thermal cycle. The magnitude of initial compressive residual stress is the highest for TBCs with hand-polished bond coat, followed by as-sprayed and barrel-finished. During thermal cycling test, the magnitude of compressive residual stress in the Al_2O_3 scale of TBCs with hand-polished and as-sprayed bond coats remained high compared to that of TBCs with barrel-finished bond coat as shown in Fig. 42. Also the standard deviation of the compressive residual stress during thermal cycling is significantly larger for TBCs with barrel-finished bond coat as reported in Tab. 11.

Table 11. Compressive residual stress in the α-Al_2O_3 scale for TBC specimens with pre-oxidation.

Bond coat	Compressive residual stress in α-Al_2O_3 for TBCs with pre-oxidation (GPa)						
	No. of thermal cycles	0	5	25	50	75	100
As-sprayed	Average	1.59	3.47	3.65	3.63	3.80	3.82
	St. Dev.	0.17	0.69	0.32	0.28	0.23	0.25
Barrel-finished	Average	1.46	3.50	3.26	3.28	Failure	-
	St. Dev.	0.20	1.07	0.80	1.07	-	-
Hand-polished	Average	2.80	3.40	3.63	3.74	3.79	Failure
	St. Dev.	0.08	0.12	0.10	0.11	0.13	-

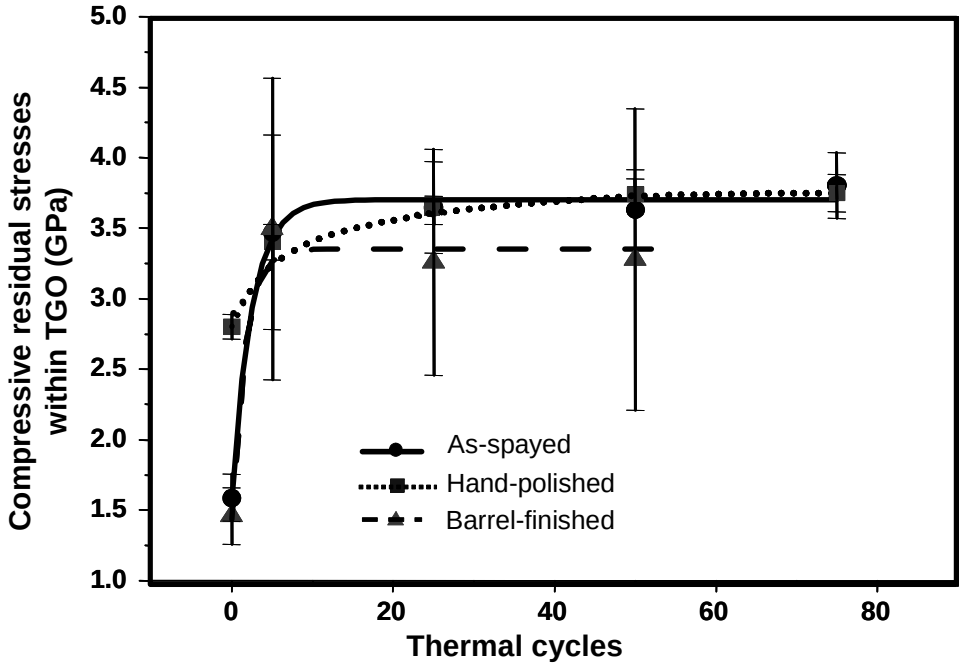

Figure 42. Compressive residual stresses within the TGO for TBCs with pre-oxidized bond coats as a function of thermal cycle.

4.5 Microstructural Development of the TGO Scale

4.5.1 Cross-sectional Microscopy

Cross-sectional microstructure of TBCs with pre-oxidized bond coats was examined by SEM and EDS. Figs. 43, 44, 46, 46 and 47 present the cross-sectional microstructure of failed TBCs with as-sprayed bond coat. Cr-, Y- rich particles were frequently found within the TGO, which is penetrated into the bond coat (i.e., pegging). Spinels containing Ni, Co, and Cr were also found at the fracture interfaces, which may

lead to the final failure as shown in Fig. 47. Figs. 48 and 49 present the cross-sectional microstructure of failed TBCs with hand-polished bond coat. Uniform TGO layer was still attached to the YSZ, delaminated from the bond coat surface. Y- rich particles were frequently found in the TGO scale for TBCs with hand-polished bond coat as shown in Fig. 49. Figs. 50 and 51 show the cross-sectional microstructure of failed TBCs with barrel-finished bond coat. Uniform TGO layer was still attached to the YSZ, delaminated from the bond coat surface. Cr-, Y- rich particles were also found within the TGO.

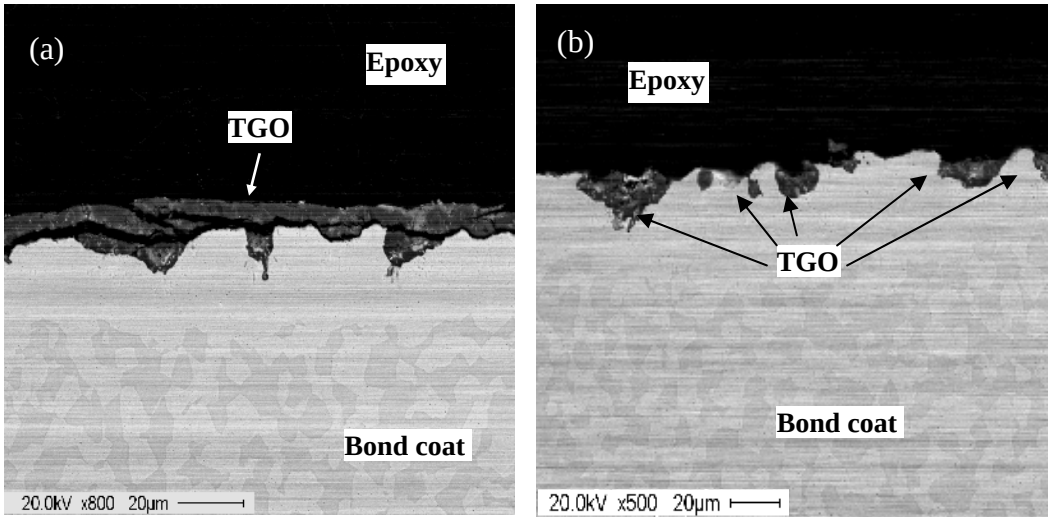

Figure 43. Backscattered electron micrographs from cross-section of failed TBCs with as-sprayed and pre-oxidized bond coat. Peggings were frequently observed at the interface of TGO/bond coat.

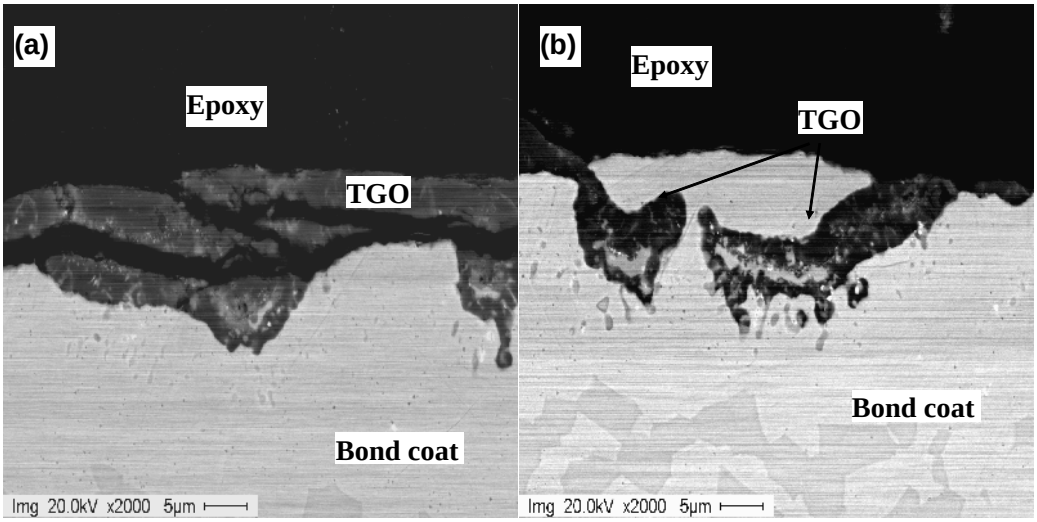

Figure 44. Backscattered electron micrographs from cross-section of failed TBCs with as-sprayed and pre-oxidized bond coats:

(a) TBCs failed at the TGO/bond coat and YSZ/TGO interfaces as well as within the TGO;
(b) TGO with white particles embedded in the bond coat.

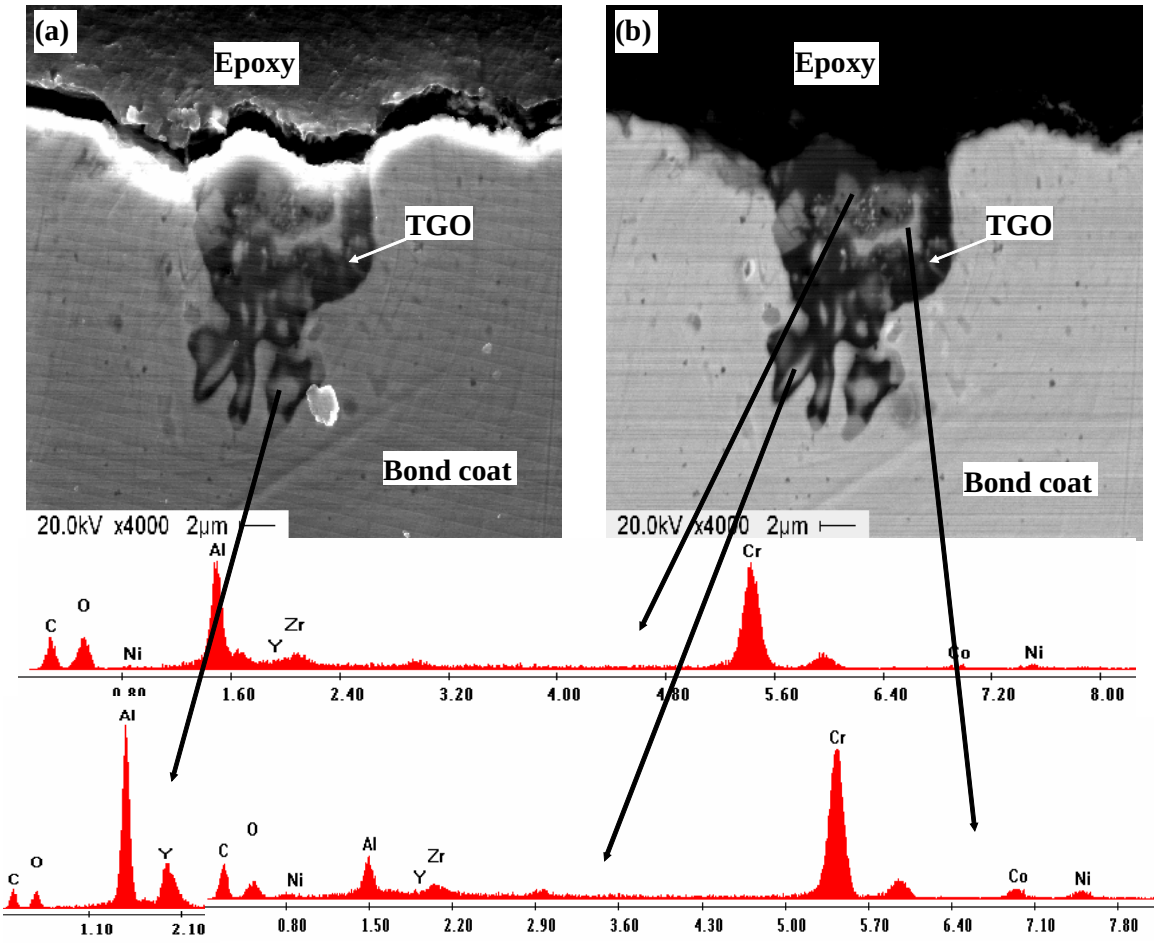

Figure 45. Cross-sectional analysis of failed TBCs with as-sprayed and pre-oxidized bond coat:

(a) Secondary electron image of the TGO with white particles embedded in the bond coat. EDS results indicated that these white particles are rich in Cr and Y.
(b) Corresponding backscattered electron micrograph of (a).

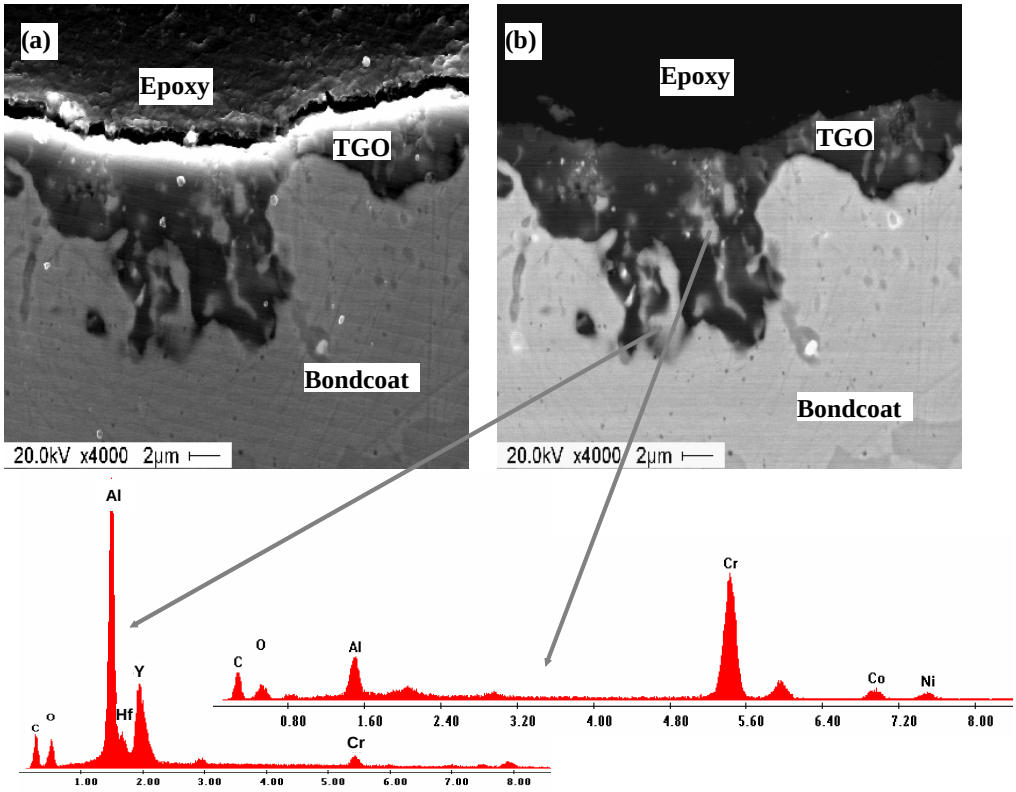

Figure 46. Cross-sectional micrographs of failed TBCs with as-sprayed and pre-oxidized bond coat:

(a) Secondary electron micrograph of the TGO with white particles embedded in the bond coat. EDS results indicated that the white particles are rich in Cr and Y.
(b) Corresponding backscattered electron micrograph of (a).

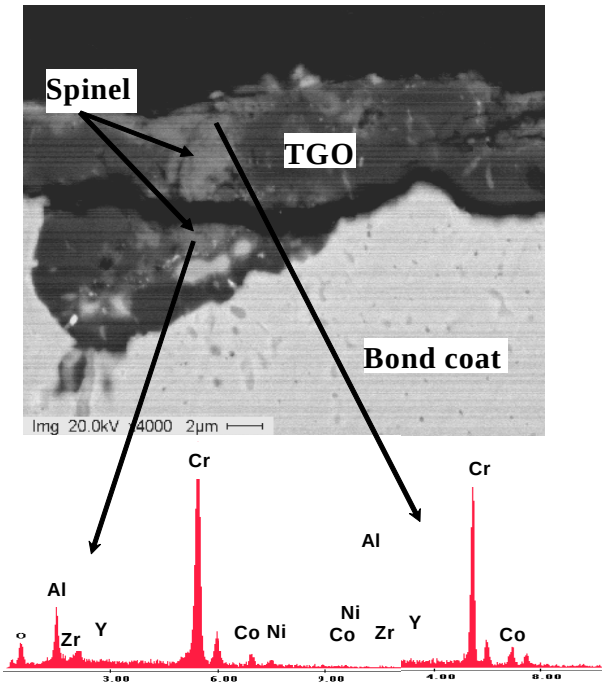

Figure 47. Cross-sectional backscattered electron micrograph and selected EDS of TBCs with as-sprayed and pre-oxidized bond coat.

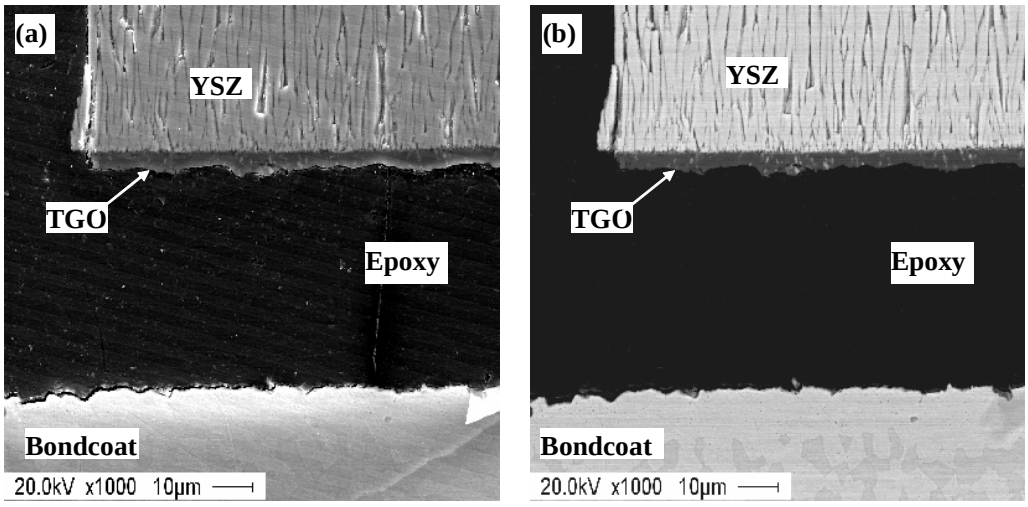

Figure 48. Cross-sectional micrographs of failed TBCs with hand-polished and pre-oxidized bond coat:

(a) Secondary electron image of fracture path showing that the failure occurs at the interface of TGO/bond coat;
(b) Corresponding backscattered electron micrograph of (a).

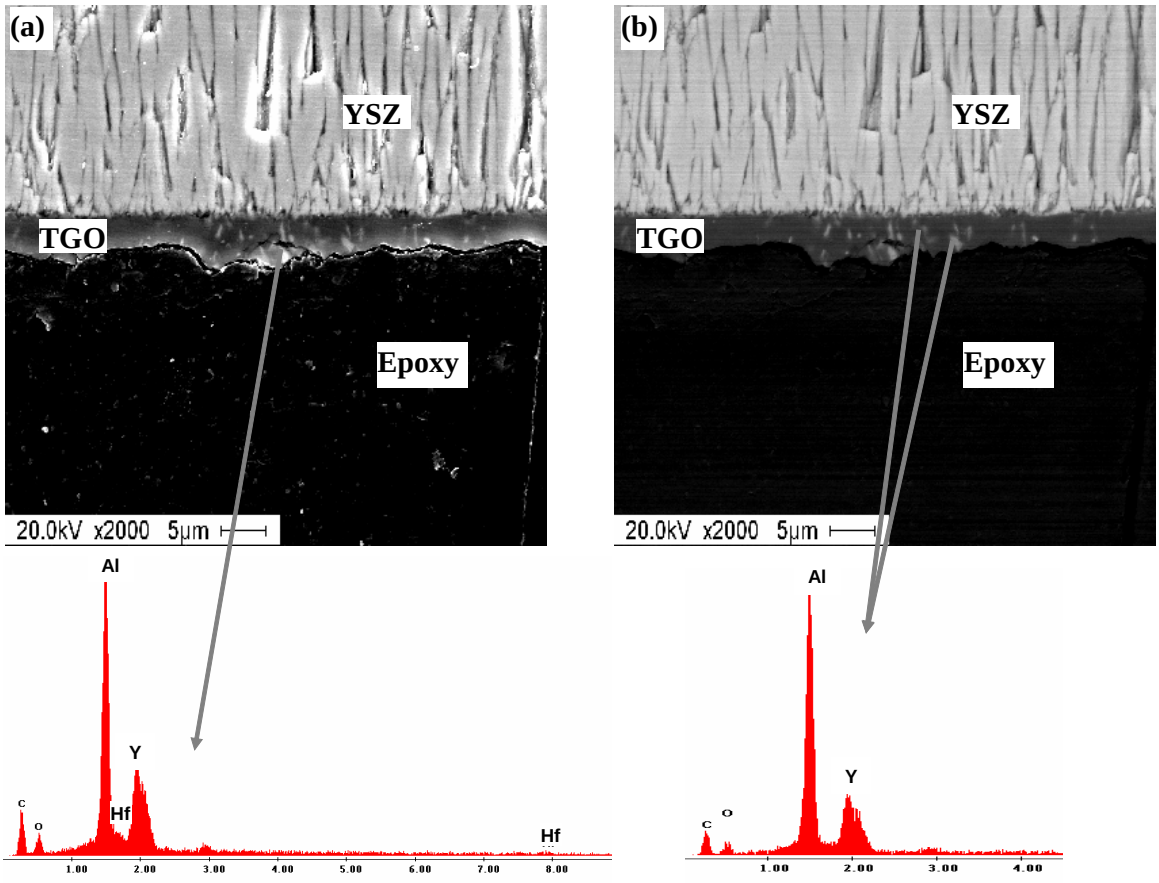

Figure 49. Cross-sectional micrographs of failed TBCs with hand-polished and pre-oxidized bond coat:

(a) Secondary electron image of the white particles embedded in the TGO. EDS results indicated that the white particles are rich in Y and Hf.
(b) Corresponding backscattered electron image of (a).

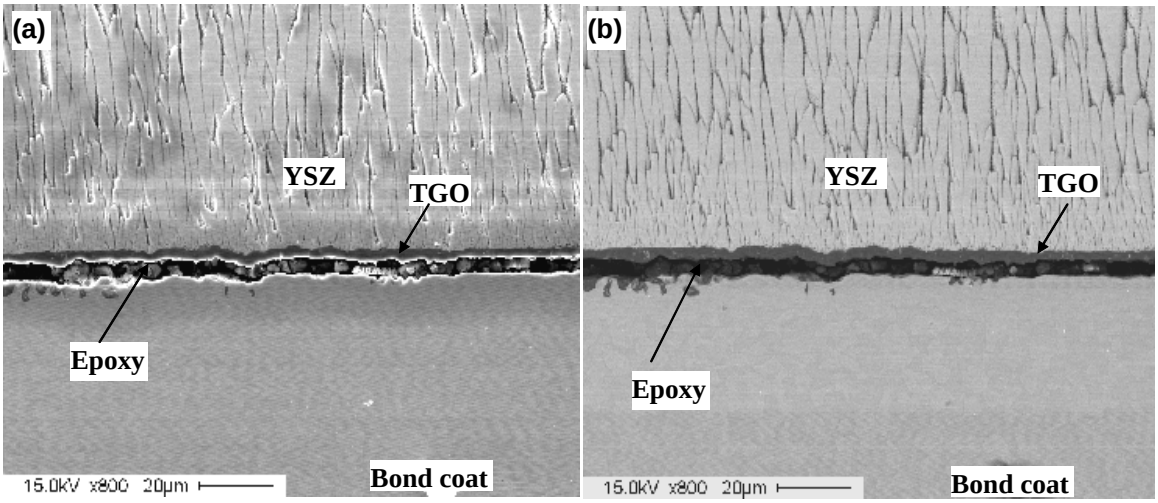

Figure 50. Cross-sectional micrographs of failed TBCs with barrel-finished and pre-oxidized bond coat:

(a) Secondary electron image of fracture path showing that the failure occurs at the TGO/bond coat interface;
(b) Corresponding backscattered electron image of (a).

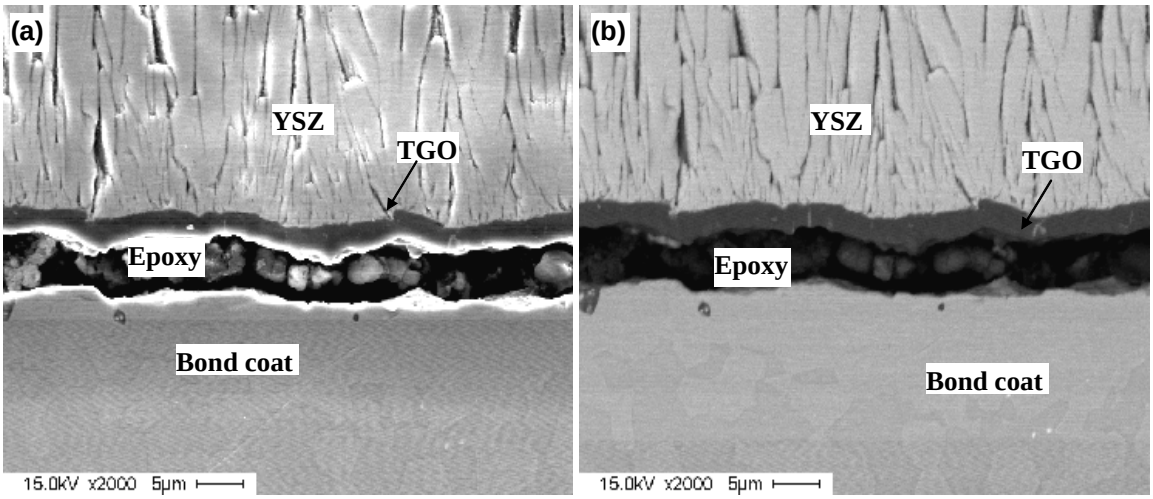

Figure 51. Cross-sectional analysis of failed TBCs with barrel-finished and pre-oxidized bond coat:

(a) Secondary electron image of the fracture interface showing that the failure occurs at the interface of TGO/bond coat;
(b) Corresponding backscattered electron micrograph of (a).

4.5.2 Transmission Electron Microscopy (TEM)

Fig. 52 shows a typical bright field image of the TGO for TBCs with as-sprayed and pre-oxidized bond coat. The inset in Fig. 52 shows the diffraction pattern corresponding to the α-Al_2O_3, which was the primary constituent of the TGO scale. Many particles, embedded within the TGO layer was observed as shown in Figs. 53 and 54. EDS shows that these particles are rich in Y, Hf and Cr. Y-rich particles were identified as Y_2O_3 by diffraction analysis as shown in Fig. 54.

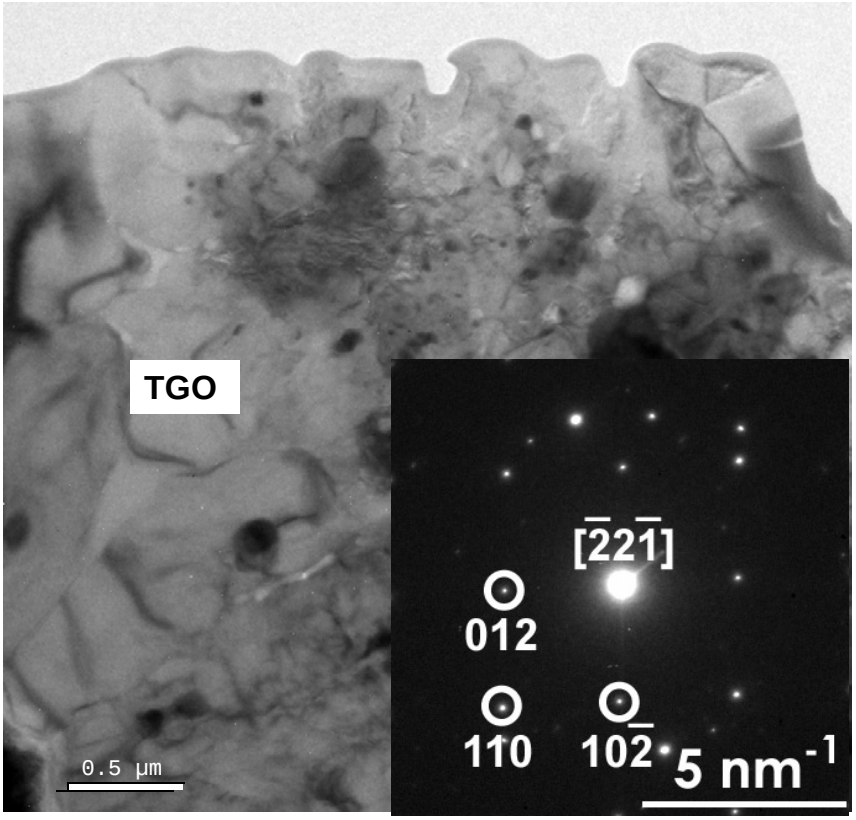

Figure 52. Bright field image with diffraction pattern showing α-Al_2O_3 as predominant constituent in the TGO for TBCs with as-sprayed and pre-oxidized bond coat.

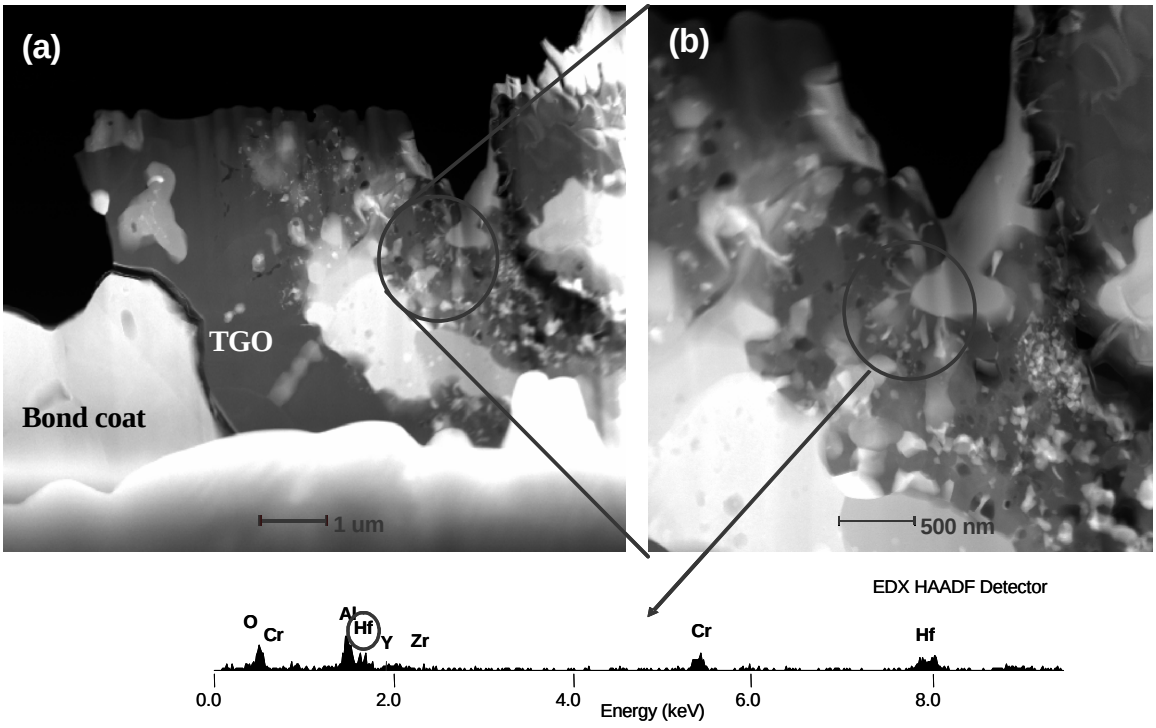

Figure 53. (a) HAADF image of the TGO embedded in the as-sprayed and pre-oxidized bond coat with small particles inside the TGO; (b) high magnification HAADF micrograph of the circled area in (a) .

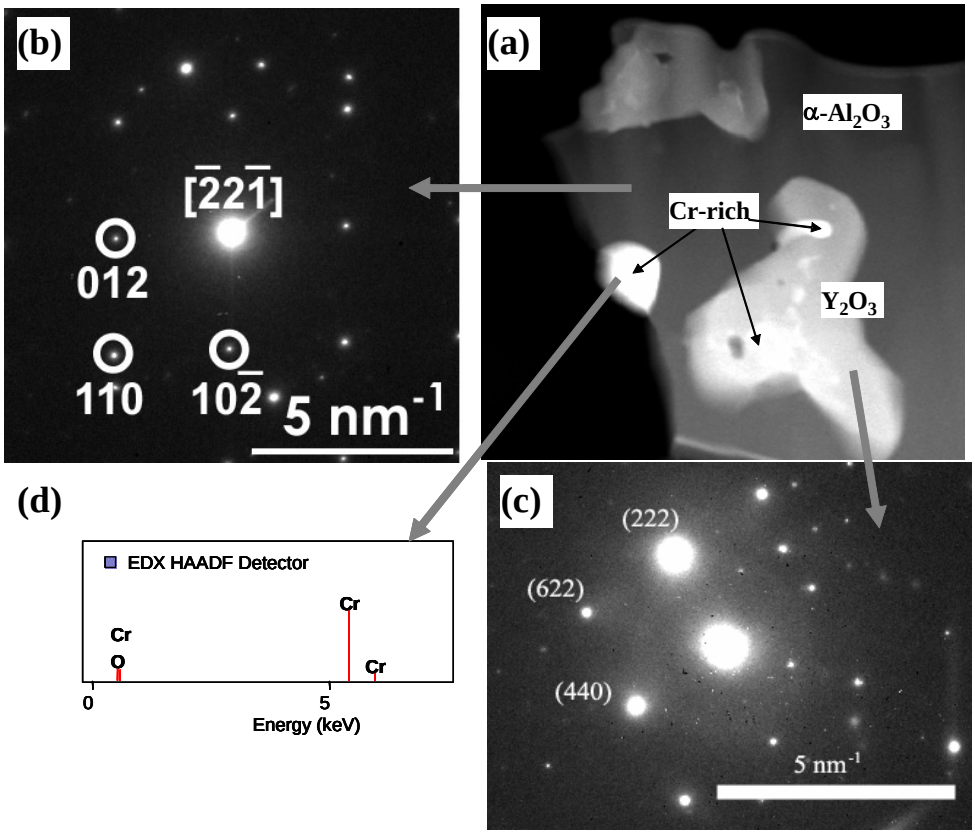

Figure 54. (a) HAADF image; (b) and (c) diffraction patterns; (d) EDS showing the TGO embedded in the as-sprayed bond coat. The TGO primary consisted of (b) α-Al_2O_3 and small particles rich in (c) Y and (d) Cr. The Y-rich particle was identified as Y_2O_3.

For TBCs with hand-polished and pre-oxidized bond coat, Y_2O_3 (cubic) particles were found within the TGO, as shown in Figs. 55, 56 and 57. Hf concentration was observed to be higher near the interface of the Y_2O_3/α-Al_2O_3 than within the Y_2O_3 particles as shown in Fig. 57(c). Heavy elements, such as Hf and Y, may be segregated at the grain boundaries as shown in Fig.56 (e). Severe segregation may cause the formation of these particles as shown in Fig. 56 (f). The size of the particles is similar to the grain size of α-Al_2O_3 as shown in Figs. 56 (a) to (d).

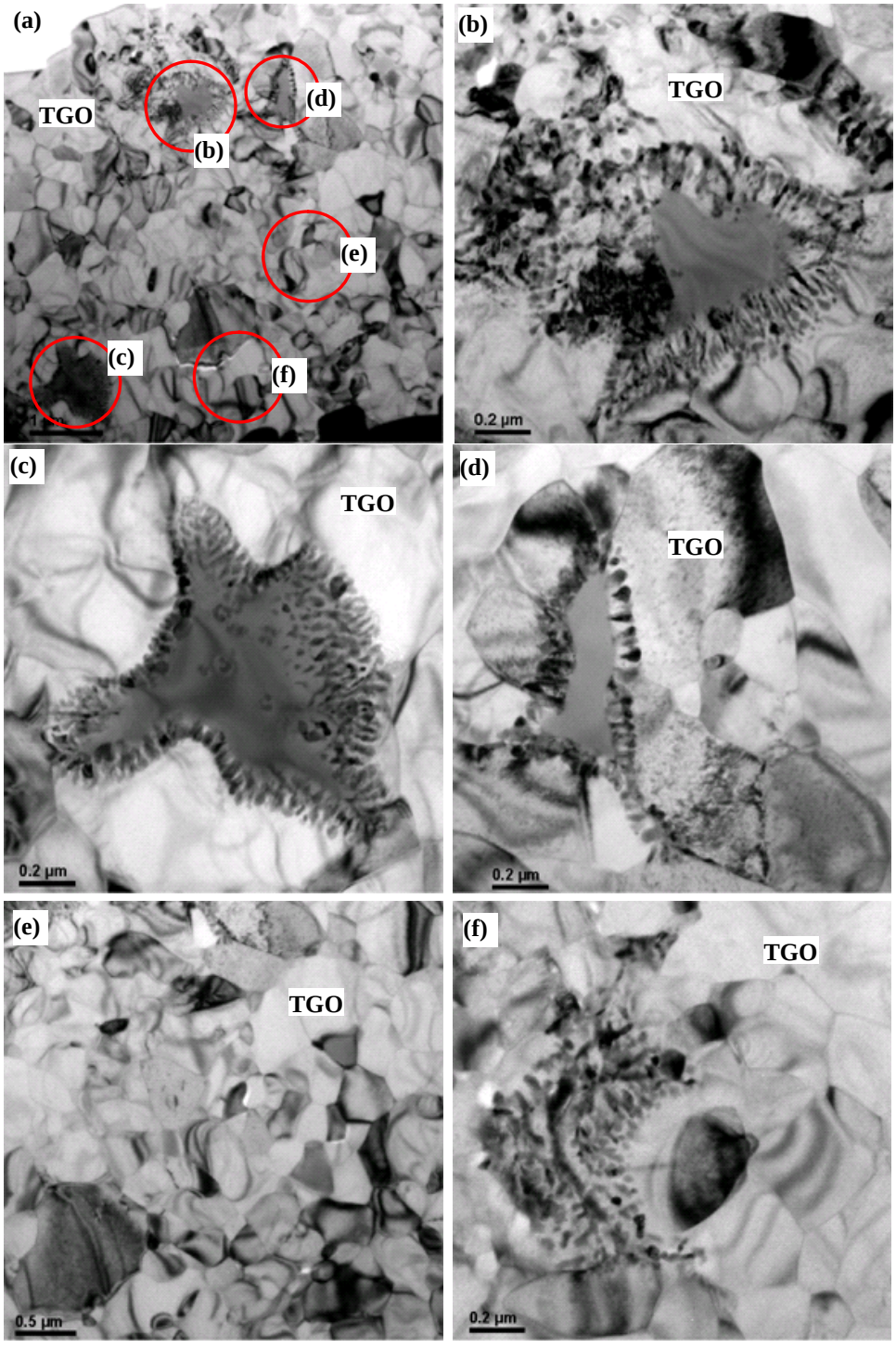

Figure 55. (a) Bright field images of small particles embedded in the TGO on failed TBC specimen with hand-polished and pre-oxidized bond coat; (b), (c), (d), (e) and (f) high magnification images of the circled parts in (a).

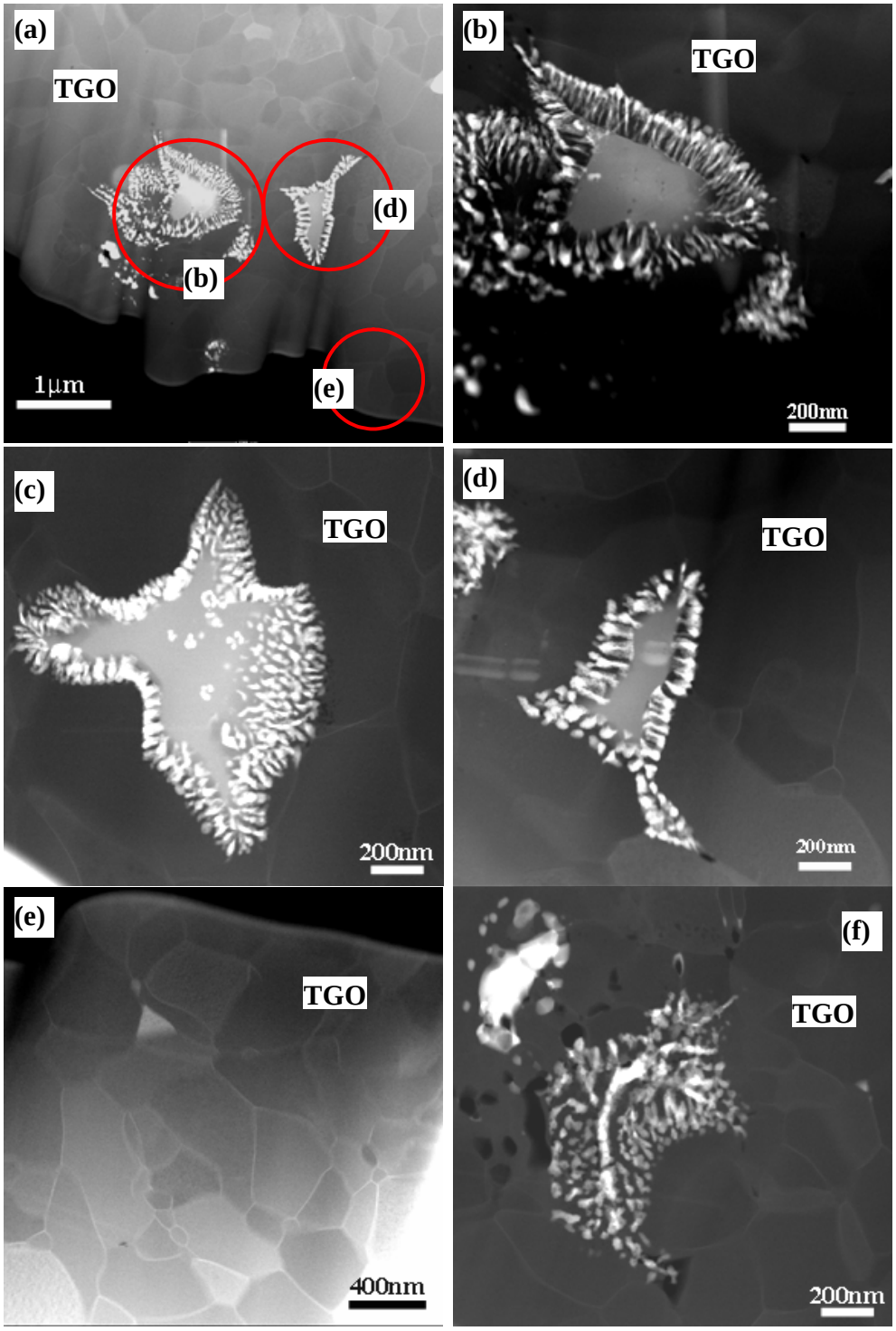

Figure 56. (a) HAADF images of small Y_2O_3 particles embedded in the TGO (α-Al_2O_3) for failed TBC specimen with hand-polished and pre-oxidized bond coat; (b), (d), (e) high magnification images of the circled parts in (a).

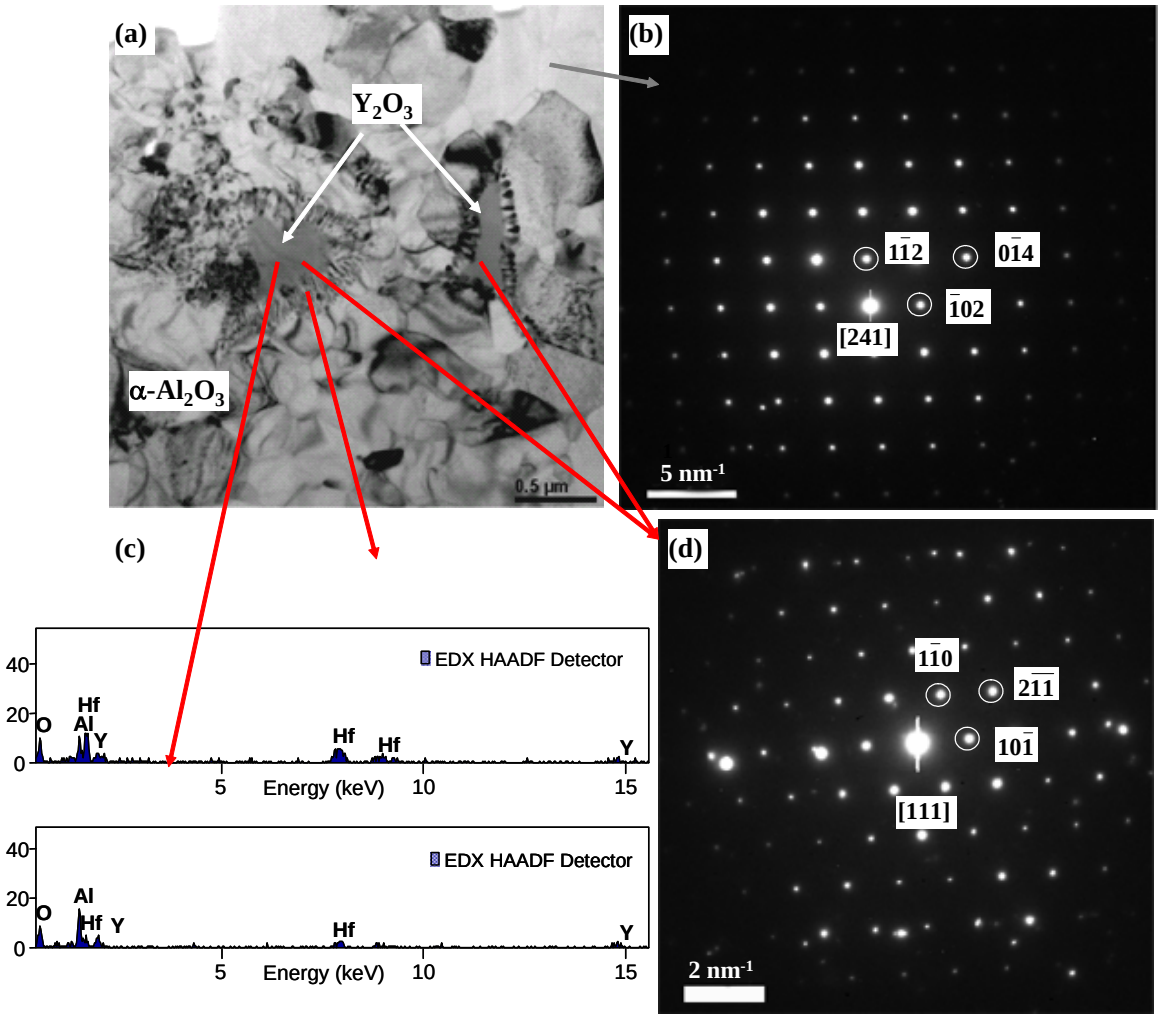

Figure 57. (a) Bright field image of small particles embedded in the TGO for failed TBC specimen with hand-polished and pre-oxidized bond coat; (b) and (d) Diffraction patterns of α-Al_2O_3 and Y_2O_3 (cubic) particles; (c) EDS showing higher concentration of Hf near the Y_2O_3/α-Al_2O_3 interface.

4.6 Fracture Surface Analysis

4.6.1 TBCs without Pre-Oxidation

Figs. 58 and 59 present backscattered and secondary electron micrographs from the fracture surfaces (i.e., bottom surface of the spalled YSZ and top surface of the bond coat) of TBCs with as-sprayed and barrel-finished bond coats, respectively. These TBC specimens were produced without any pre-oxidation. For TBCs with as-sprayed bond coats, the TGO is present on both the bottom surface of spalled YSZ and the top surface of exposed bond coat. This means that the fracture took place after 100 thermal cycles within the TGO and at the TGO/bond coat and the YSZ/TGO interfaces. Some islands of TGO are found embedded in the bond coat corresponding to bond coat surface roughness and pegging as shown in Figs. 58 (e) and 58 (f). For TBCs with barrel-finished bond coats, the TGO is present only on the top surface of exposed bond coat. This means that the fracture took place after 20 thermal cycles at the interface between the TGO and the YSZ topcoat.

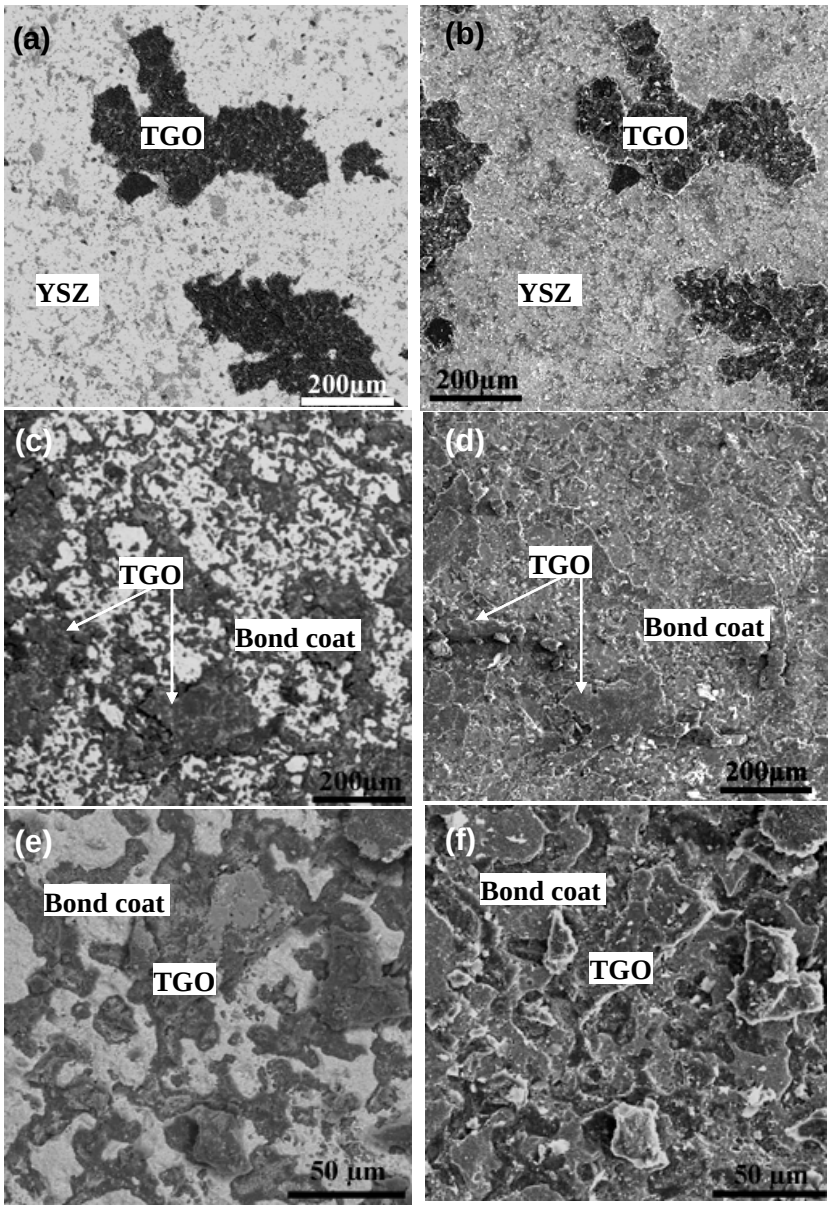

Figure 58. Fracture surfaces (i.e., bottom surface of the spalled YSZ and top surface of the exposed bond coat) of TBCs with as-sprayed bond coats. The spallation failure occurred after 100 1-hour thermal cycles at 1121°C.

(a) Backscattered electron micrograph from the bottom surface of the spalled YSZ.
(b) Corresponding secondary electron micrograph of (a).
(c) Backscattered electron micrograph from the top surface of the exposed bond coat.
(d) Corresponding secondary electron micrograph of (c).
(e) High magnification backscattered electron micrograph from the top surface of the exposed bond coat showing some islands of embedded TGO in the bond coat.
(f) Corresponding secondary electron micrograph of (e).

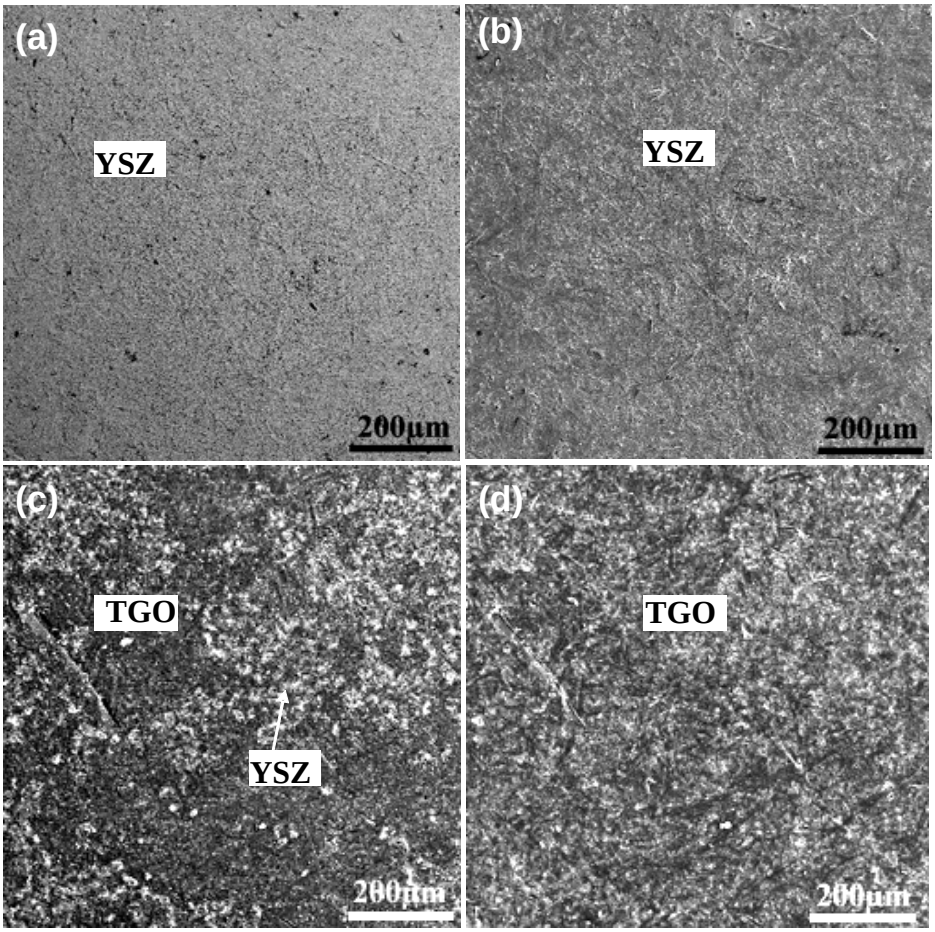

Figure 59. Fracture surfaces (i.e., bottom surface of the spalled YSZ and top surface of the exposed bond coat) of TBCs with barrel-finished bond coats. The spallation failure occurred after 20 1-hour thermal cycles at 1121°C.

(a) Backscattered electron micrograph from the bottom surface of the spalled YSZ.
(b) Corresponding secondary electron micrograph of (a).
(c) Backscattered electron micrograph from the top surface of the exposed bond coat.
(d) Corresponding secondary electron micrograph of (c).

4.6.2 TBCs with Pre-Oxidation

Backscattered and secondary electron micrographs from the bottom surface of the spalled YSZ and the top surface of the exposed bond coat are shown in Figs. 60, 61, and 62, as a function of bond coat surface finish: as-sprayed, hand-polished, and barrel-finished, respectively. These TBC specimens were produced with pre-oxidation, which was carried out prior to YSZ deposition. Fig. 60 shows that the fracture took place at the TGO/bond coat and YSZ/TGO interfaces as well as within the TGO for pre-oxidized TBC specimens with as-sprayed bond coats. However, for pre-oxidized TBCs with hand-polished bond coats, the fracture primarily occurred at the TGO/bond coat interface as presented in Fig. 61. The only TGO observed on the top surface of the exposed bond coat was that embedded in the bond coat. Similar fracture along the TGO/bond coat interface was observed for the pre-oxidized TBCs with barrel-finished bond coats as presented in Fig. 62.

Tab. 12 summarizes the characteristics of fracture path and lifetime of TBCs as a function of bond coat surface preparation. For TBCs with hand-polished and barrel-finished bond coats after pre-oxidation, more TGO remained on the bottom surface of the spalled YSZ while increases in the thermal cycling lifetime were observed. The fracture path remained similar for TBCs with as-sprayed bond coat (i.e., both interfaces of YSZ/TGO and TGO/bond coat as well as within the TGO) after the pre-oxidation heat treatment: the improvement in the lifetime of the TBCs with as-sprayed bond coats was not significant after the pre-oxidation heat treatment.

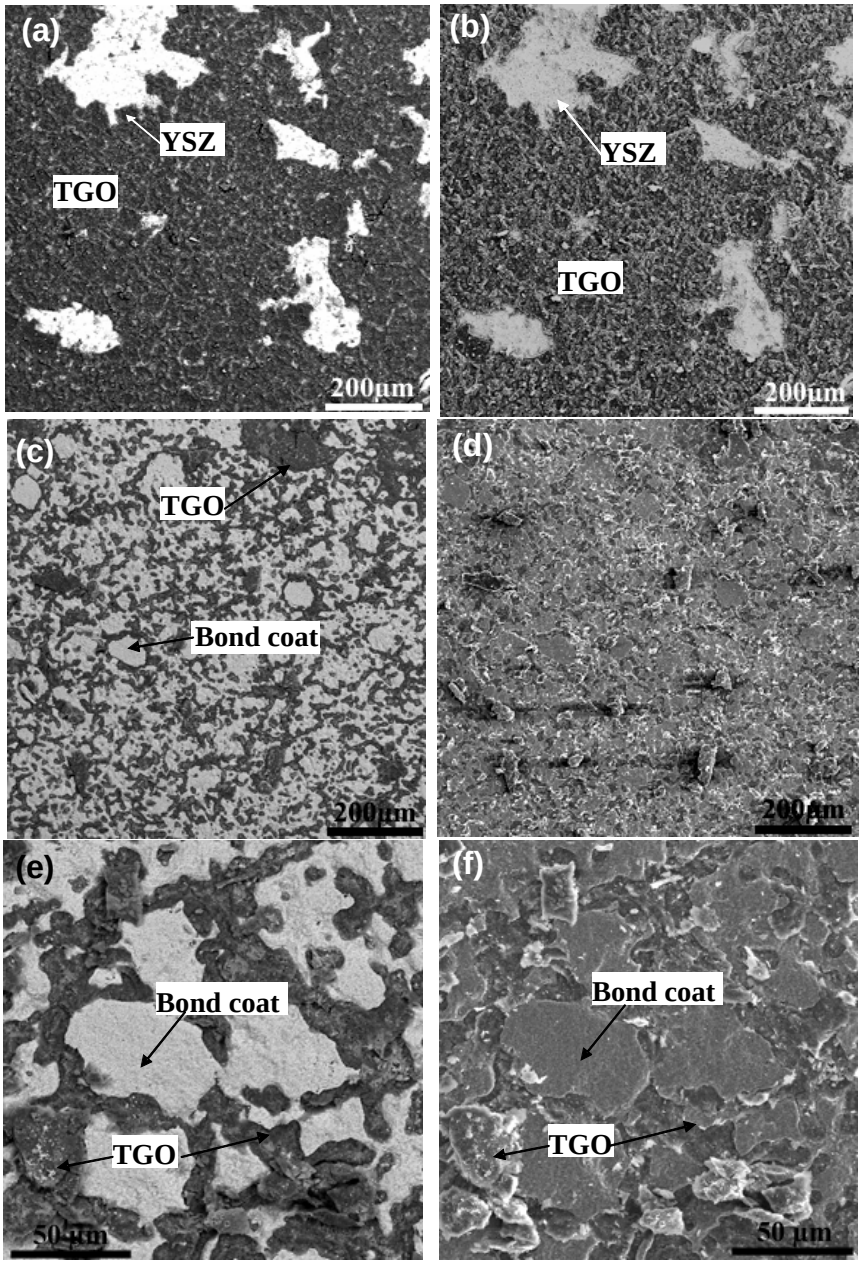

Figure 60. Fracture surfaces (i.e., bottom surface of the spalled YSZ and top surface of the exposed bond coat) of TBCs with as-sprayed and pre-oxidized bond coats. The spallation failure occurred after 100 1-hour thermal cycles at 1121°C.

(a) Backscattered electron micrograph from the bottom surface of the spalled YSZ.
(b) Corresponding secondary electron micrograph of (a).
(c) Backscattered electron micrograph from the top surface of the exposed bond coat.
(d) Corresponding secondary electron micrograph of (c).
(e) High magnification backscattered electron micrograph from the top surface of the exposed bond coat showing some islands of embedded TGO in the bond coat.
(f) Corresponding secondary electron micrograph of (e).

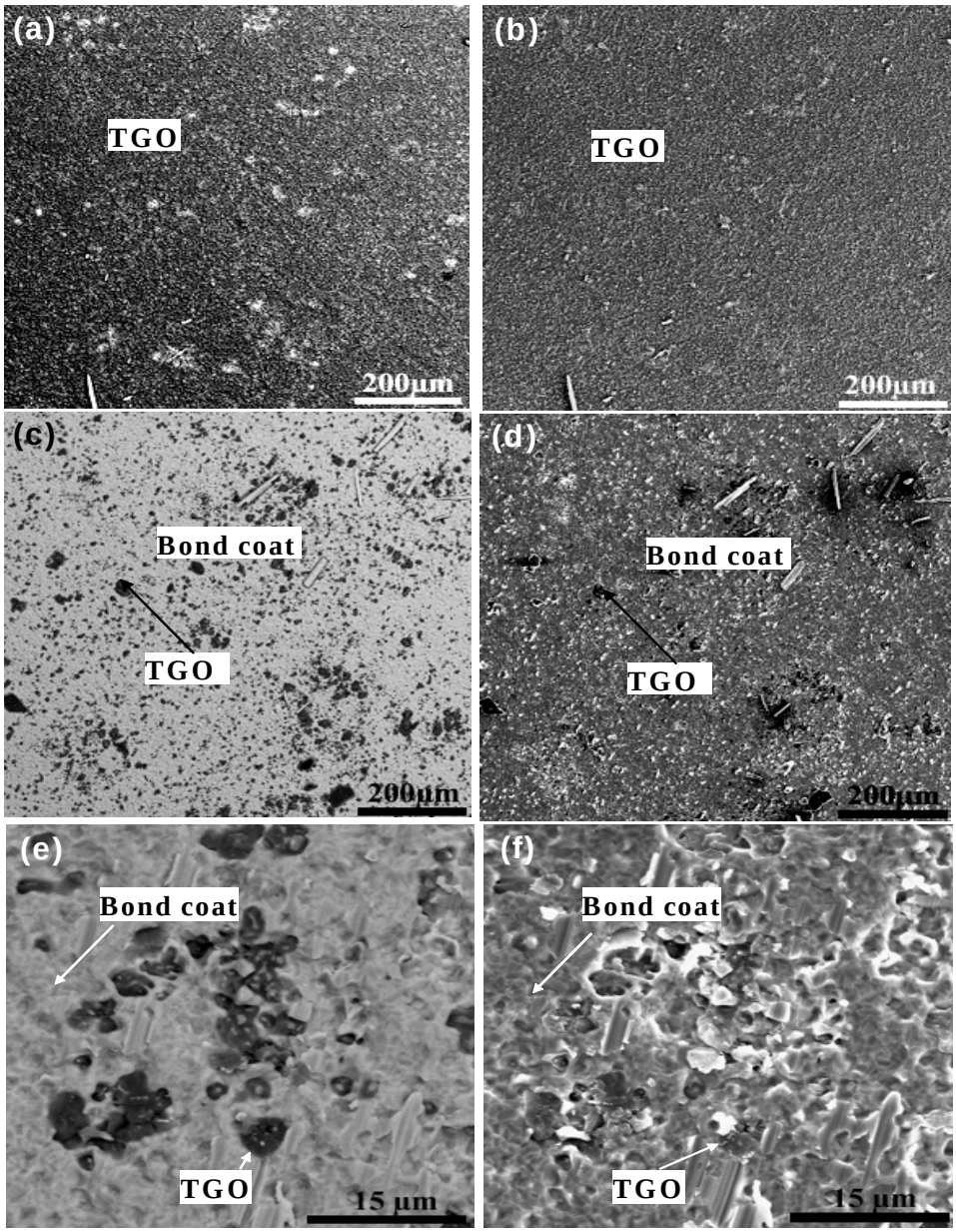

Figure 61. Fracture surfaces (i.e., bottom surface of the spalled YSZ and top surface of the exposed bond coat) of TBCs with hand-polished and pre-oxidized bond coats. The spallation failure occurred after 105 1-hour thermal cycles at 1121°C.

(a) Backscattered electron micrograph from the bottom surface of the spalled YSZ.
(b) Corresponding secondary electron micrograph of (a).
(c) Backscattered electron micrograph from the top surface of the exposed bond coat.
(d) Corresponding secondary electron micrograph of (c).
(e) High magnification backscattered electron micrograph from the top surface of the exposed bond coat showing some islands of embedded TGO in the bond coat.
(f) Corresponding secondary electron micrograph of (e).

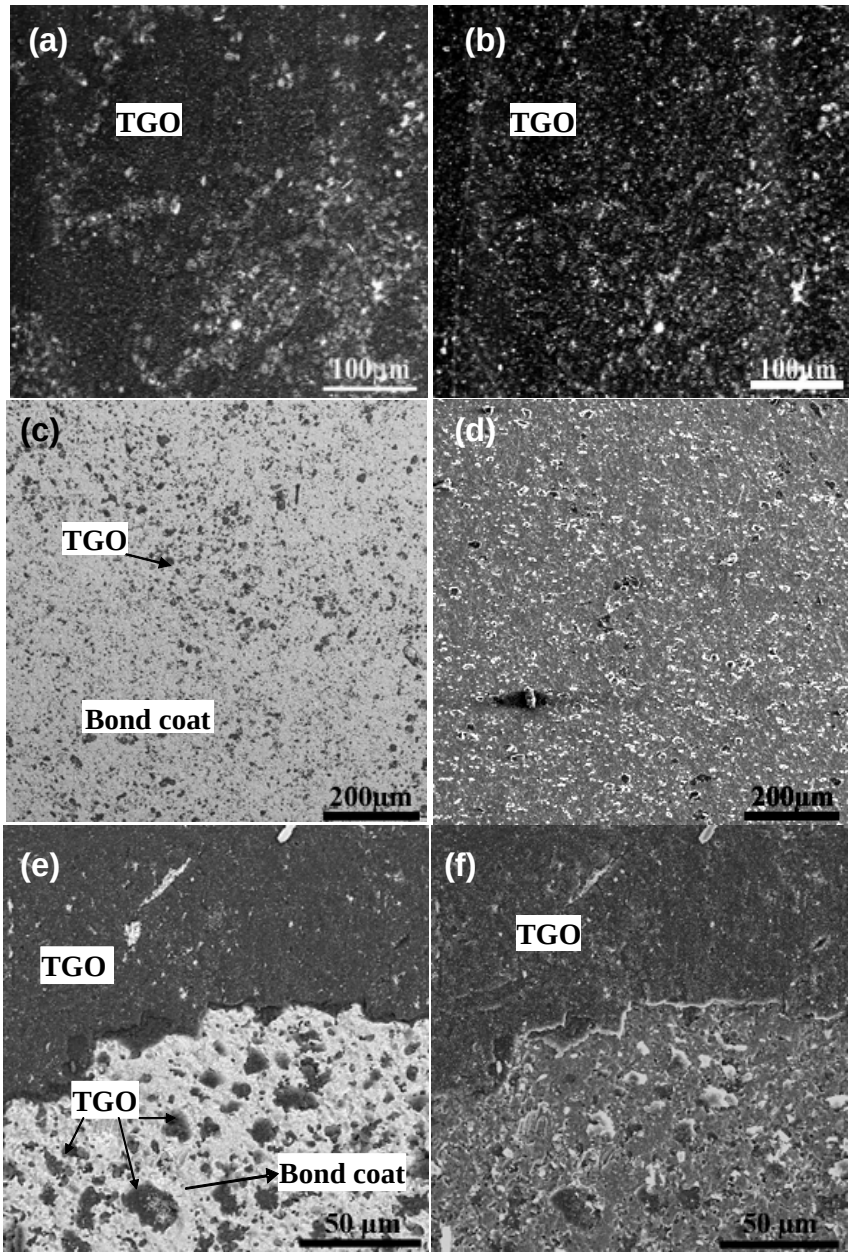

Figure 62. Fracture surfaces (i.e., bottom surface of the spalled YSZ and top surface of the exposed bond coat) of TBCs with barrel-finished and pre-oxidized bond coats. The spallation failure occurred after 75 1-hour thermal cycles at 1121°C.

(a) Backscattered electron micrograph from the bottom surface of the spalled YSZ.
(b) Corresponding secondary electron micrograph of (a).
(c) Backscattered electron micrograph from the top surface of the exposed bond coat.
(d) Corresponding secondary electron micrograph of (c).
(e) High magnification backscattered electron micrograph from the top surface of the exposed bond coat showing some islands of embedded TGO in the bond coat.
(f) Corresponding secondary electron micrograph of (e).

Table 12. Summary of fracture path characteristics and the lifetime of TBCs as a function of bond coat surface preparation.

Bond coat surface preparation	Pre-Oxidation	Fracture path	Percentage of TGO on the exposed bond coat	Average Lifetime of TBCs
As-received	No	YSZ/TGO & TGO/Bond coat	70.5%	87.5
	Yes	YSZ/TGO & TGO/Bond coat	58.9%	101.0
Hand-polished	No	*	*	0
	Yes	TGO/Bond coat	18.0%	95.0
Barrel-finished	No	YSZ/TGO	98.9%	25.0
	Yes	TGO/Bond coat	24.1%	50.0

* No observable TGO. Fracture between YSZ and bond coat.

Based on these observations, one can conclude that the premature spallation of TBCs can occur when there is not a well-developed TGO scale prior to or during the YSZ deposition by EB-PVD. Early spallation has been observed with failure at YSZ/TGO interface for non-pre-oxidized TBCs with barrel-finished bond coat. TBCs with the longest durability can be achieved by having the fracture paths restricted to the TGO/bond coat interface after the TGO scale has been fully established through the pre-oxidation heat-treatment and/or EB-PVD.

5. DISCUSSION

5.1 Surface Roughness of Bond Coats

After the pre-oxidation heat treatment at 1100°C, the surface roughness increased for barrel-finished and hand-polished bond coats as reported in Tab. 4 and Figs. 26, 27 and 28. However, for as-sprayed bond coat, small changes in the topography do not have large influence on the high average surface roughness. Therefore, the surface roughness of the as-sprayed bond coat can be considered to remain the same.

For hand-polished bond coats as shown in Fig. 32 and 33, bond coat surface rumples after pre-oxidation, presumably due to coating-substrate thermal expansion mismatch and plasticity. Hand-polishing may introduce residual stress near the bond coat surface, which can provide well distributed strain energy near the surface. Thus, during heat treatment, the surface may be oxidized easily with a uniform TGO layer. During cooling, the difference between thermal expansion coefficient of the TGO and bond coat, as listed in Tab.1, introduces thermal expansion mismatch between these two layers. Since no major surface defect except for grain boundaries exists on the hand-polished bond coat, the flat surface can rumple and increase the roughness of the surface. Therefore, pre-oxidation heat treatment can increase the surface roughness for hand-polished bond coat.

On the other hand, grain boundaries can act as surface defects for hand-polished bond coat. Thus, at the initial stage of oxidation, oxides can first nucleate at these grain

boundaries. Based on the observation in Figs. 32 and 33, the grain boundaries deepened, which would mean that the metal flow was directed out of the boundaries. This suggested that bond coat volume decrease during oxidation. The major change in the bond coat microstructure is the phase transition to a γ-Ni solid solution with associated dissolution of the β-NiAl. This is attributed to Al depletion caused by the formation of Al_2O_3 on top of bond coat surface and inward Al diffusion into the superalloy. Along with the reaction, there is a volume constriction according to the calculation by Tolpygo.[115] Since grain boundaries can act as the fast diffusion paths, Al deplete fast near the grain boundaries. Therefore, grain boundaries appeared to be deepened.

However, the barrel-finished bond coats appear to have more grooves and protrusions after the heat treatment as shown in Figs. 30 and 31. This may be caused by uneven oxidation due to barrel-finish processing. Moreover, difference in oxidation rate and the formation of other oxide phases can arise from contamination associated with barrel-finish processing.

5.2 Factors Related to the Lifetime of TBCs

5.2.1 Bond Coat Surface Roughness and TBC Lifetime

Fig. 63 correlates the bond coat surface preparation technique, the average bond coat surface roughness, and the average thermal cycling lifetime of TBCs. For TBCs without pre-oxidation heat treatment, a longer TBC lifetime was observed with rougher bond coats as presented in Fig. 63(a). However, such a simple relation does not exist for TBCs after the pre-oxidation heat treatment as presented in Fig. 63(b). TBCs with hand-polished and pre-oxidized bond coats yielded higher durability than TBCs with barrel-finished and pre-oxidized bond coat. Therefore, surface roughness of the bond coat is not the only factor that affects the lifetime of the TBCs. Initial development of the TGO scale from the bond coat is another critical factor influencing the TBC lifetime.

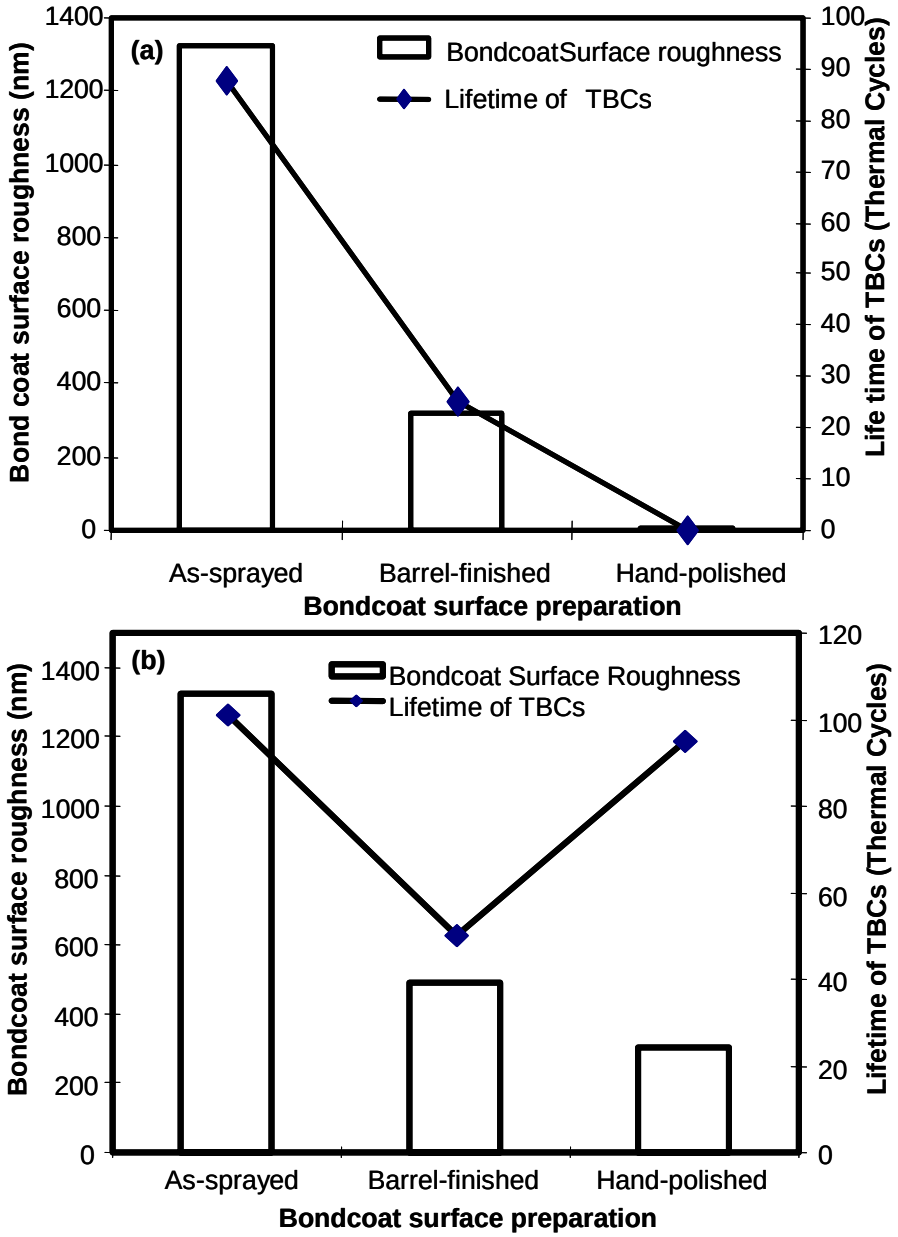

Figure 63. Correlation between the bond coat surface preparation method, the bond coat surface roughness and the lifetime of EB-PVD TBCs with NiCoCrAlY bond coat (a) without and (b) with pre-oxidation heat treatment.

5.2.2 Residual Stress in the Al_2O_3 Scale and TBC Lifetime

For TBCs specimens produced without any pre-oxidation heat treatment, Fig. 64 shows the correlation among the initial residual stresses of the TGO scale (α-Al_2O_3), bond coat surface preparation and the thermal cycling lifetime. The magnitude of initial compressive residual stress in the α-Al_2O_3 is only slightly higher for TBCs with as-sprayed bond coats, which has the longer lifetime.

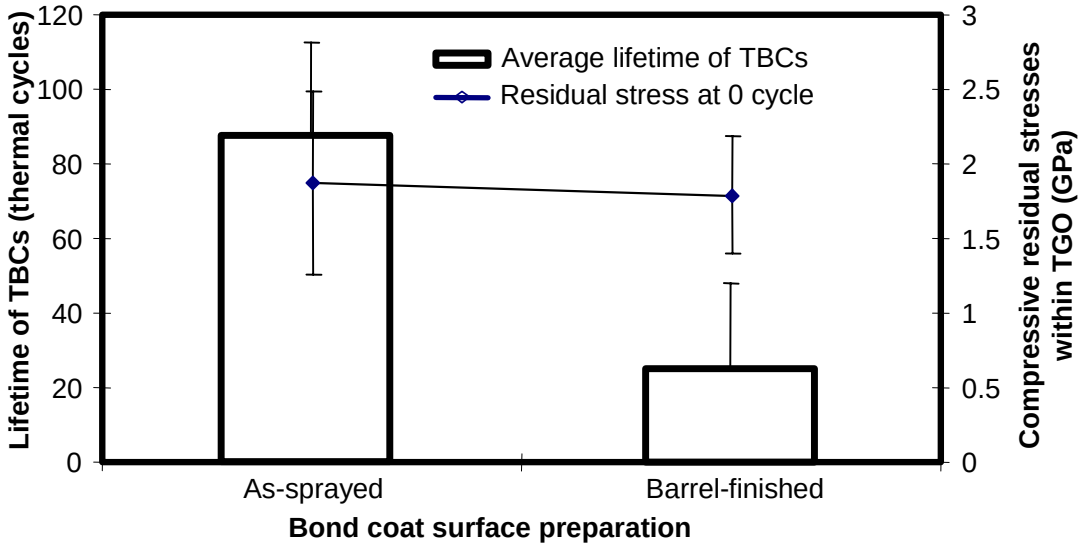

Figure 64. Correlation among the initial residual stresses within the α-Al_2O_3 scale, bond coat surface preparation and the thermal cycling lifetime for TBCs specimens with no pre-oxidation heat treatment.

For TBCs with pre-oxidized bond coats, the magnitude of the initial compressive residual stress in the α-Al_2O_3 was similar for the TBCs with as-sprayed and barrel-finished bond coats. However, the lifetime of these two types of specimens had a great difference as shown in Fig. 65.

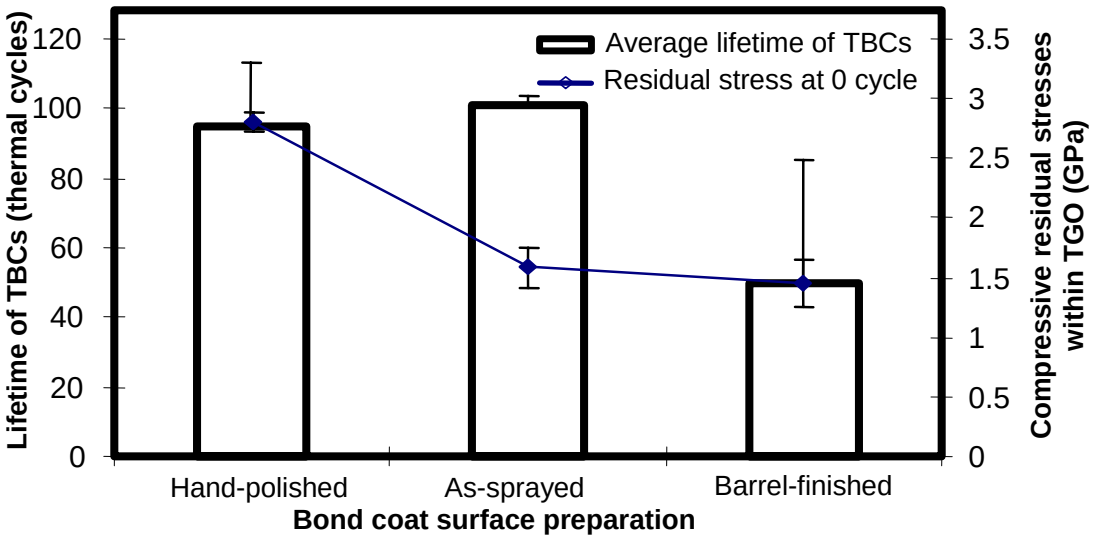

Figure 65. Correlation among the initial residual stresses within the TGO scale, bond coat surface preparation and the thermal cycling lifetime for TBCs specimens with pre-oxidized bond coats.

The initial rise in compressive residual stress after few thermal cycles, as shown in Figs. 41 and 42 can be attributed to the coverage of TGO scale from discontinuous to continuous. Similar results were also found by Xie et al..[116,117] In their study, the initial oxide scale did not form a continuous layer until after at least 10, 1-hour thermal cycles at 1121°C.

Throughout thermal cycling, for TBCs without pre-oxidation heat treatment, the magnitude of compressive residual stress within the TGO was observed to be lower for the specimens with as-sprayed bond coat. These TBCs had a longer lifetime. For TBC specimens with barrel-finished bond coat and a shorter lifetime, the magnitude of the compressive residual stress in the TGO was higher as shown in Fig. 41.

For TBCs with pre-oxidized bond coats, the magnitude of compressive residual stress within the TGO remained higher during thermal cyclic test for the TBCs with longer lifetime as shown in Fig. 42.

Therefore, from this study, the initial compressive residual stress within the TGO is not the only factor that can be directly and simply related to the lifetime of the TBCs. Other factors such as bond coat surface roughness, initial phase constituent of the Al_2O_3 scale should also be taken into consideration.

5.2.3 Polymorphic Constituents of the Al_2O_3 Scale and TBC Lifetime

A longer lifetime was obtained for specimens with higher relative luminescence intensity from the equilibrium α-Al_2O_3 in the initial TGO layer for a given surface preparation/roughness as shown in Fig. 66. Phase transformation from the metastable to stable phase may be accompanied by the formation of voids due to volumetric constraints. For example, there is about 4.7% volume contraction for θ- to α-Al_2O_3 phase transformation. Thus, these phase transformations can create damages at the YSZ/TGO interface. However, pre-oxidation heat treatment will promote the formation of α-Al_2O_3 and can stop premature failure at YSZ/TGO interface. Therefore, the lifetime of the TBCs increased after the pre-oxidation heat treatment.

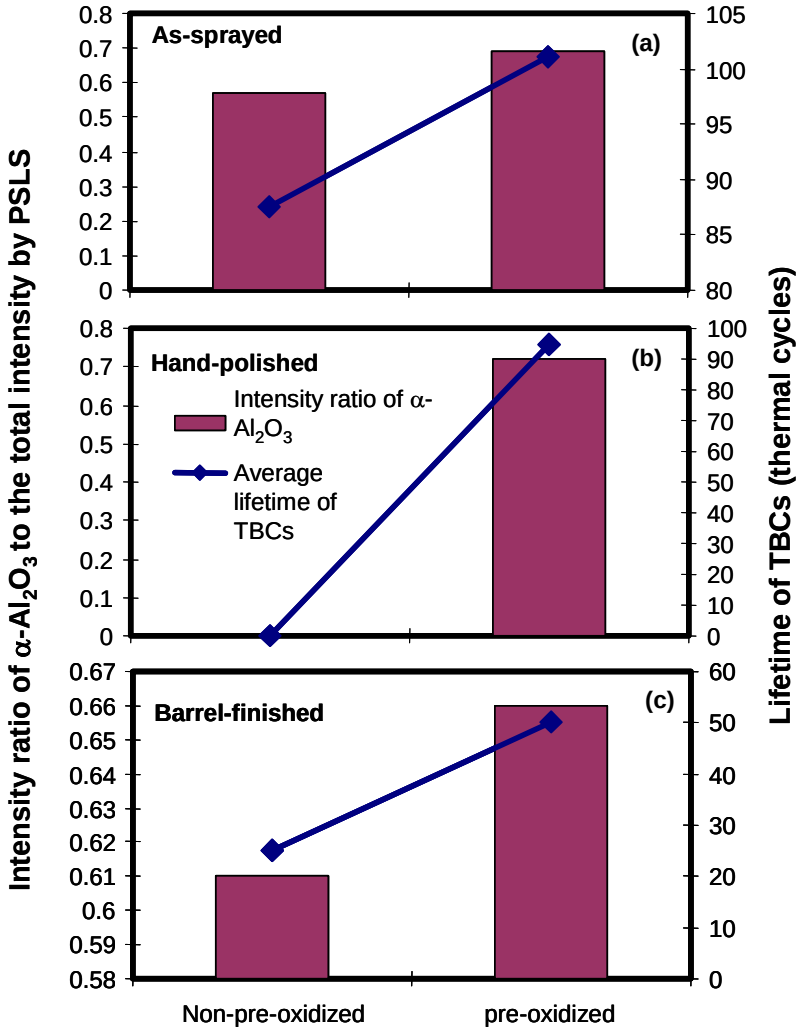

Figure 66. Correlation among the relative initial intensity ratio of α-Al_2O_3, bond coat surface preparation, and the thermal cycling lifetime of TBCs specimens. (a) TBCs with as-sprayed bond coat; (b) TBCs with hand-polished bond coat; (c) TBCs with barrel-finished bond coat.

The smooth bond coat surface should not promote the formation of the equilibrium phase. However, N-luminescence from TGO scale was observed from pre-oxidized TBC specimens with hand-polished bond coat, presumably due to a significant presence of Cr^{3+} in α-Al_2O_3 a shown in Fig. 26. The formation of Cr_2O_3 has been

reported to assist the nucleation of α-Al_2O_3. [118] In addition, hand-polishing may introduce residual stress near the bond coat surface, which can provide necessary energy for the equilibrium phase nucleation and/or transformation. Moreover, the hand-polished process removes the absorbed contaminants that can adversely affect the phase nucleation/transformation.

Initial phase constituents within TGO, not only affect the lifetime of TBCs, but also influence the initial compressive residual stress within the α-Al_2O_3. Before thermal cycling, the higher relative luminescence intensity from the equilibrium α-Al_2O_3 corresponded to the larger magnitude of initial compressive residual stress for TBCs with pre-oxidized bond coats. For these TBCs, a correlation between the luminescence intensity and the residual stress exists as shown in Fig 67.

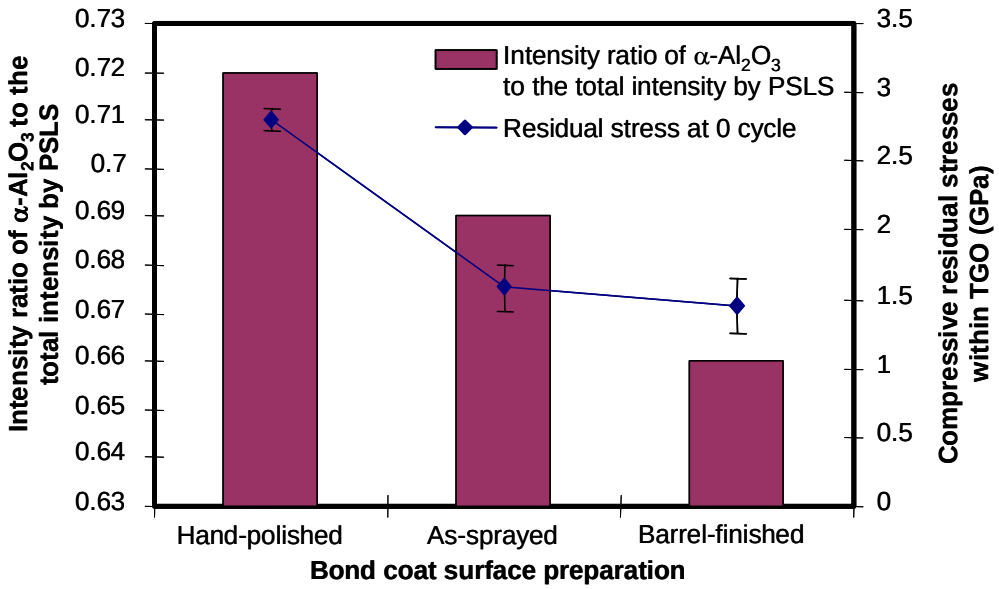

Figure 67. Correlation among the bond coat surface preparation method, initial residual stresses within the α-Al_2O_3 scale, and initial relative intensity ratio of the equilibrium α-Al_2O_3 for pre-oxidized TBC specimens.

5.3 Microstructural Development and Failure Mechanisms

For specimen with as-sprayed bond coat, the bond coat surface was observed to be rough and not uniform, so that the TGO can easily grow by penetrating into the bond coat. Those embedded TGO can act as nails (e.g., pegging) interlocking the interface as shown in Fig. 44. A schematic illustration of this mechanism is shown in Fig. 68. Over the years, there have been contradictory reports on pegging. Douglas suggested that the adhesion can be improved between the TGO and bond coat based on pegging.[119] The oxide pegs are important to spallation resistance because of their potential to arrest crack propagation at the metal-scale interface. However, the presence of oxide pegs has been linked to increased scale spallation because of stress concentration and/or thermal expansion mismatch between the alloy and the TGO scale.[120]

A significant amount of spinels were detected at fracture interfaces as shown in Fig. 47. They are considered to be the weak link of the interface, and may lead to the spallation failure.[121] According to Mumm and Evans, brittle appearance of the region around the embedded oxides suggests the occurrence of embrittlement. This also matches the fracture path results, since parts of the TGO remained on the as-sprayed bond coat surface.

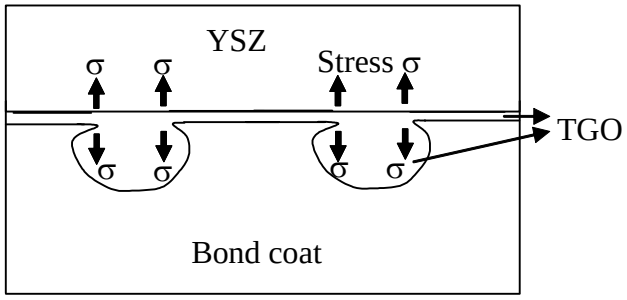

Figure 68. A schematic diagram for continuous TGO layer embedded in the bond coat interlocking the interface from delamination.

For hand-polished specimens, the bond coat surface is smoother. After the pre-oxidation, a uniform TGO can form without impurities or other oxides (as shown in Fig. 49) to degrade the adhesion of YSZ topcoat deposited by EB-PVD. TBCs with smooth bond coats usually spall by buckling over a rather large area. A number of distinctly separate buckles develop over a large number of cycles. The prerequisite for buckling is the development of a sufficiently large and contiguous debonded region. In general, the size of the debonded region needed for buckling increases with increasing TGO thickness. As the strain energy release rate driving the delamination increases with an increasing TGO thickness, the buckling tendency decreases because a larger flaw is required. Therefore, the increase in oxide thickness alone does not lead directly to buckling spallation. Thus, for samples with hand-polished bond coat surface, spallation involves a more difficult and time-consuming degradation process, which leads to a longer lifetime. The as-sprayed and hand-polished and pre-oxidized specimens have longer lifetime than the barrel-finished specimens due to different reasons.

TBCs with barrel-finished bond coat may have contaminations absorbed on to the bond coat surface. These contaminations can cause formation of deleterious reaction products, degrade the interfacial integrity and eventually lead to early failure. [111]

The difference in the thermal expansion coefficient of the bond coat and TGO is much larger than that of the TGO and YSZ as listed in Tab. 1. Therefore, for large repeated thermal fatigue, fracture prefers to propagate at the TGO/bond coat interface. For specimen with shorter lifetime, spallation occurs at the interface of YSZ/TGO, presumably due to a poor adhesion between the YSZ and the TGO. Similar spallation results were found by Mumm and Evans.[122] After short times (<10 hours) exposure at 1100°C, delamination occurs primarily within the TGO and YSZ. After longer exposures (<100 hours), delamination occurs principally along the interface of TGO and bond coat.

According to Wright, reactive elements (RE) (e.g., Y) inhibit S segregation at the metal-oxide interface. Also, RE segregate to oxide grain boundaries, where they can significantly reduce the outward transport of Al, hence decrease the rate of oxidation (now mostly by oxygen transport), drastically change the oxide morphology and contribute to the improved scale adherence (reduced interfacial void formation). However, oversupply of the RE can be detrimental. Increased concentration of RE in the bond coat can cause internal oxidation and formation of RE oxides (e.g., HfO_2, Y_2O_3 and YAG) within the TGO scale as shown in Figs. 53 to 57. Also, the formation of RE oxides can act as fast diffusion paths for oxygen and cause mechanical disruption if incorporated into the TGO scale.

6. CONCLUSIONS

Effects of surface preparation methods for the NiCoCrAlY bond coats on the thermal cyclic lifetime and failure of TBCs were investigated in this study. Variables arising from the surface preparation methods include initial surface roughness of the bond coats, initial phase constituents in the TGO scale, and the initial residual stress in the TGO scale. The development of phase constituents (i.e., transformations) and the residual stress in the TGO scale was non-destructively examined by PSLS as a function of thermal cycling. Microstructural development of selected specimens was also examined as a function of thermal cycling by using SEM/EDS and TEM/STEM. The thermal cyclic lifetime of TBCs obtained in this study was correlated to the bond coat surface preparation methods. Findings from this investigation are listed below:

- The long lifetime during 1-hour thermal cycling at 1121°C around 100 cycles was observed for TBCs with as-sprayed bond coats regardless of pre-oxidation and TBCs with hand-polished and pre-oxidized bond coats.
- Lifetime of TBCs, in general, was observed to improve when a pre-oxidation heat treatment at 1100°C with P_{O_2} =10^{-8} atm was carried out prior to YSZ deposition. With pre-oxidation heat treatment, relative photostimulated luminescence intensity of the α-Al_2O_3 increased. Thus, the improvement in TBC lifetime can be correlated with the increase in luminescence intensity of α-Al_2O_3 in the TGO scale given a surface preparation/roughness. The lifetime improvement due to the pre-oxidation was

particularly significant to TBCs with hand-polished bond coats and negligible for TBCs with as-sprayed bond coat.

- Spallation-fracture paths depended on the lifetime of TBCs. Premature spallation of TBCs occurs at the interface between the YSZ and TGO. Longer durability can be achieved by restricting the fracture paths to the TGO/bond coat interface.
- Small particulate phase observed through the TGO scale was identified as Y_2O_3 (cubic) by diffraction analysis on TEM. While the addition of Y in the NiCoCrAlY bond coat helps the adhesion of the TGO scale, excessive alloying can lead to deleterious effects.

APPENDIX

PUBLICATIONS AND PRESENTATIONS

Publications:

J. Liu and Y. H. Sohn, "Effects of Bond Coat Surface Roughness and Pre-Oxidation on the Thermal Cycling Lifetime of Thermal Barrier Coatings", Proceedings of International 28th Annual International Conference on Advanced Ceramics and Composites, in Press, 2004.

N. Mu, **J. Liu**, Y. H. Sohn and Y. L. Nava, "Long Term Oxidation and Phase Transformations in Aluminized CMSX-4 Superalloys**",** Surface and Coatings Technology, Accepted for Publication, in Press, 2004.

Presentations:

J. Liu, N. Mu, S. K. Jha, and Y. H. Sohn, "Al-O-N Based Duplex Coating System for Improved Oxidation resistance for Superalloys and NiCrAlY Coatings,' Presented at the 2003 Annual Joint Symposium of Florida Chapter of American Vacuum Society and Florida Society for Microscopy, March 17-18, 2003, Orlando, Florida, USA.

J. Liu and Y. H. Sohn, "Effect of Surface Preparation on the Lifetime and Failure of Thermal Barrier Coating Specimens" Presented at ASM International Surface Engineering Congress & Exposition-Thermal Spray Coatings, September 26, 2003, Indianapolis, Indiana, USA.

J. Liu, Y. H. Sohn, "Effects of Bond Coat Surface Roughness and Pre-Oxidation on the Thermal Cycling Lifetime of Thermal Barrier Coatings", Presented at the 28^{th} International Cocoa Beach Conference and Exposition on Advanced Ceramics and Compositions in conjunction with the 8^{th} International Symposium on Ceramics in Energy Storage and power Conversion Systems-Advanced Thermal Barrier Coating Development, January 25-30, 2004, Cocoa Beach, Florida, USA.

S. Laxman, S. K. Jha, B. M. Kempshall, **J. Liu** and Y. H. Sohn, "A Microstructural Observation of Nearly-Failed Thermal Barrier Coating: A study by Photo-Stimulated Luminescence Spectroscopy and Transmission Electron Microscopy" Presented at Gordon Research Conference-High Temperature Corrosion, July 2003, New London, New Hampshire, USA.

N, Mu, **J. Liu**, Y. H. Sohn, Y. L. Nava, "Long Term Oxidation and Phase Transformations in Aluminized CMSX-4 Superalloys", Presented at the International Conference on Metallurgical Coatings and Thin Films, ICMCTF 2004, April 19-23, 2004, San Diego, California, USA.

LIST OF REFERENCES

[1] D. J. Wortman, B. A. Nagaraj, E. C. Duderstadt, " Thermal barrier coatings for gas turbine use," *Mater. Sci. Eng. A*, 120-121, 433-38, 1989.

[2] R. L. Jones, Experiences in seeking stabilizers for zirconia having hot corrosion-resistance and high temperature tetragonal (t') stability. *NRL/MR/6170--96-7841*, 1996.

[3] R. Miller, "Thermal barrier coatings for aircraft engines: History and directions," *Journal of Thermal Spray Technology*, 6, 35-41, 1997.

[4] A. G. Evans, D. R. Mumm, J. W. Hutchinson, G. H. Meier, F. S. Pettit, "Mechanisms controlling the durability of thermal barrier coatings," *Progress in Materials Science*, 46, 505-53, 2001.

[5] D. Zhu, R. A. Miller, "Thermal-Barrier coating for advanced gas-turbine engines," *MRS Bulletin*, 25, 43-48, 2000.

[6] W. J. Brindley and R. A. Miller, TBCs for better engine efficiency, *Adv. Mat. Proc.*, 8, 29, 1989.

[7] I. Kvernes, Ceramic coatings as thermal barriers in diesel and gas turbine components, in *High Tech. Ceram. - Part C: Materials Science Monographs* 38 C, Elsevier, Amsterdam, pp. 2519-36, 1987.

[8] R. L. Jones, Metallurgical and Ceramic Protective Coatings, K. H. Stern, ED. (Chapman & Hall, London, 1996) 194.

[9] J. D. Plunkett, NASA Contributions to the technology of inorganic coatings, *Technology survey* NASA SP-504, NASA, Washington D. C., 145, 1964.

[10]Rigney, R. Viguie, D. J. Wortman, and W. W. Skelly, *Proc. of the Workshop on Thermal Barrier Coatings*, NASA-SP-3312, 135-150, NASA Lewis Research Center, 1995.

[11] U. Schulz, M. Menzebach, C. Leyens, Y. Yang, *Surf. Coat. Technol*. 146-147, 117-123, 2001.

[12] N. P. Padture, E. H. Jordan, M. Gell, *Science*, 296, 280, 2002.

[13] P. K. Wright, *Current Opinions in Solid Stated Mater. Sci*., 4, 255, 1999.

[14] F. H. Stott, G. C. Wood, *Mater. Sci. Eng*. A87, 267, 1987.

[15] P. Kofstad, *High Temperature Corrosion* (Elsevier Applied Science), New York, 1988.

[16] P. K. Wright, *Mater. Sci. Eng.* A245 191-200, 1998.

[17] E. Schumann, C. Sarioglu, J. R. Blachere, F. S. Pettit, G. H. Meier, *Oxid. Metals* 53, 259, 2000.

[18] D. M. Lipkin, D. R. Clarke, *Oxid. Metals* 45, 267, 1996.

[19] K. W. Schlichting et al., *Mater. Sci. Eng*. A291, 68, 2000.

[20] S. M. Meier, D. M. Nissley, K. D. Sheffler, T. A. Cruse, *J. Eng. Gas Turbines Powers*, 112, 521, 1990.

[21] M. W. Brumm, and H. J. Grabke, *Corrision Science*, 33, 1677-1690, 1992.

[22] J. Doychak, J. L. Smialek and T. E. Mitchell, *Metall. Trans.* A. 20A, 499, 1989.

[23] C. Mennicke, D. R. Mumm and D. R. Clarke, *Zeits. Metallkd*., Vol 90, pp. 1079, 1999.

[24] D. R. Clarke, V. Sergo and M. Y. He, Elevated Temperature Coatings: Science and Technology III, ed. J. M. Hampikian and N. B. Dahotre, TMS, Warrendale, PA, pp. 67, 1999.

[25] J. Cheng, E. H. Jordan, B. Barber, and M. Gell, *Acta Mater*., 46, 5839, 1998.

[26] A. G. Evans, M. Y. He, J. W. Hutchinson, *Prog. Mater.Sci.*, 46, 249, 2001.

[27] F. O. Soechting, *Thermal Barrier Coating Workshop 1995. NASA Conference Publication* 3312, 1, 1995.

[28] D. S. Duvall, and D. L. Ruckle, Ceramic thermal barrier coatings for turbine engine components, *ASME Paper 82-GT-332*, 1982.

[29] S. Stecura, "Optimizaiton of the NiCrAl-Y/ZrO_2-Y_2O_3 thermal barrier system", *NASA Tech. Memo.* 86905, NASA, Cleveland OH, 1985.

[30] D. W. Richerson, *Modern Ceramic Engineering: Properties, Processing, and Use in Design*, Marcel Dekker, New York, pp.38-45 and 139-142.

[31] A. V. Virkar, R. L. K. Matsumoto, *J. Am. Ceram. Soc*., 69(10), C224-6, 1986.

[32] D. G. Teer, *Coatings for High Temperature Applications*, Ed, by E. Lang, Applied Science Publisher p. 79, 1983.

[33] C. T. Sims, N. S. Stoloff and W. C. Hagel, edited, *Superalloy II*, New York: John Wiley and Sons, 1987.

[34] P. K. Wright and A. G. Evans, *Mechanisms governing the performance of thermal barrier coatings*, Princeton Materials Institute & Princeton University, PMI-99-11.

[35] T. E. Strangman, *Thin Solid Films*, 127, 93-105, 1985.

[36] G. W. Goward, (1974) Coatings and coating processing for gas turbine airfoils operating in a marine environment, in *Proceedings of 1974 Gas Turbine Materials in the Marine Environment Conference* (eds J. W. Fairbanks and I. Machlin), Castine ME, Metals and Ceramics Information Center, Battelle, Columbus OH, pp. 277-96.

[37] S. Terry, and C.Levi, University of California-Santa Barbera, unpublished research.

[38] S. Stecura, *American Ceramic Society Bulletin*, vol. 56, 1082-1086, 1977.

[39] S. Stecura, "Optimizaiton of the Ni-Cr-Al-Y/ZrO_2-Y_2O_3 thermal barrier system", *Advanced Ceramic Materials*, vol. 1, p.68-76, 1986.

[40] N. Czech, M. Juez-Lorenzo, V. Kolarik, W. Stamm, *Surf. Coat. Technol.*, 108-109, 36-42, 1998.

[41] D. J. Wortman, E. C. Duderstadt, and W. A. Nelson, *Journal of Engineering for Gas Turbines and Power*, vol. 112, p. 527-530, 1990.

[42] W. J. Brindley, and R. A. Miller, "Thermal barrier coatings life and isothermal oxidation of low-pressure plasma sprayed bond coat alloys', *Surf. coat. Technol.*, vol. 43-44, p. 446-457, 1990.

[43] J. A. Haynes, E. D. Rigney, M. K. Ferber and W. D. Porter, *Surf. Coat. Technol.*, 86-87, 102, 1996.

[44] D. M. Zhu and R. A. Miller, in Fundamental Aspects of High Temperature Corrosion, Ed. D. A. Shores et al (Electronchemical Society Proceedings, Pennington, 1997), pp. 288307.

[45] J. G. Smeggil, *Mater. Sci. Engr*., 87, 261-265, 1987.

[46] J. L. Smialet, D. T. Jayne, J.C. Schaeffer, W. H. Murphy, *Thin Solid Films*, 253, 285-92, 1994.

[47] G. H. Meier, F. S. Pettit, Report on AFOSR Contract F 49620-981-0221. Univ. of Pittsburgh, 1 September, 1999.

[48] J. A. Hyanes, Y. Zhang, W. Y. Lee, B. A. Pint, I. G. Wright, K. M. Cooley, In: J. M. Hampiklan, N. B. Dahotre, editors. *Elevated temperature coatings: science and technology*. Warrendale (PA): TMS, p 185, 1999.

[49] P. Deb and D. H. Boone, Microstructrual formation and effects on the performance of Platinum modified aluminide coatings, Technical report, Nava Postgraduate School, 1985.

[50] G. R. Johnston and P. G. Richards, The relative durabilities of conventional aluminide and platinum-modified aluminide coatings in an operational gas turbine engine, I. G. Wright, edited, *Corrosion in Fossil Fuel Systems,* Eelectrochemical society, 456, 1983.

[51] M. J. Stiger, N. M. Yanar, M. G. Topping, F. S. Pettit, G. H. Meier, *Z. Metallkd.*, 90, 1069-78, 1999.

[52] W. F. Schilling, "Low pressure plasma sprayed coatings for industrial gas turbines, NAT Advanced Workshop, *Coatings for heat engines*, Italy, April 1984.

[53] A. N. Khan, J. Lu, *Surf. Coat. Technol.*, 166, 37-43-TA, 2003.

[54] M. F. Trubelja, et.al, Pratt & Whitney Thermal Barrier Coatings Development, United Technologies Research Center, 411 Silver Lane, East Hartford, CT 06108.

[55] M. Gell, E. Jordan, K. Vaidyanathan, K. McCarron, B. Barber, Y. H. Sohn, V. K. Tolpygo, *Surf. Coat. Technol*. 120-121, 53, 1999.

[56] M. Gell, K. Vaidyanathan, B. Barber, J. Cheng, E. Jordan, *Met. Mater. Trans*. A. A 30, 427, 1999.

[57] K.Vaidyanathan, M. Gell, E. H. Jordan, *Surf. Coat. Technol*., 133-134, 28-34, 2000.

[58] P. Hariharan, "Interferometers", in Handbook of Optics, McGraw-Hill Companie, Inc., New York, Chapter 21, 1996.

[59] B. Bhushan, J. C. Wyant and C. L. Koliopoulos, "Measurementof surface topography of magnetic tapes by Mirau interferometer", *Appl. Opt*., 28: 1489-1497, 1985.

[60] J. C. Wyant, "Optical profilers for surface roughness", *Proceedings of the Society of Photo-Optical Instrumentation Engineers*, 525, 174-180, 1985.

[61] J. C. Wyant, and K. Creath, " Advances in Interferometric Optical Profiling", *Int. J. Mach. Tools Manufact.* vol. 32, No. 1/2, 5-10, 1992.

[62] J. C. Wyant, "Use of an ac heterodyne lateral shear interferometer with real-time wavefront corrections systems", *Appl. Opt*. 14 (11): 2622-2626, Nov. 1975.

[63] K. Creath, "Phase-Shifting Interferometry Techniques", in *Progress in Optics XXVI*, E. Wolf, ed. (Elsever Science, 1988), pp. 357-373.

[64] M. Davidson, K. Kaufman, I. Mazor, and F. Cohen, "An application of interference microscopy to integrated circuit inspection and metrology", *Proc. SPIE*, 775, 233-247, 1987.

[65] G. S. Kino and S. Chim, "Mirau correlation Microscope", *Appl. Opt*. 29, 3775-3783, 1990.

[66] T. Dresel, G. Hausler, and H. Venzke, "Three-dimensional sensing of rough surfaces by coherence radar, *Appl. Opt.* 31(7): 919-3925 ,March 1992.

[67] P. J. Caber, "An interferometric Profiler for Rough Surfaces", *Appl. Opt*. 32 (19): 3438-3441, July 1993.

[68] J. A. Haynes, E. D. Rigney, M. K. Ferber, W. D. Porter, Oxidation and degradation of a plasma-sprayed thermal barrier coating system, *ASME Paper*, 96-GT-286, 1996.

[69] I. G. Wright and B. A. Pint, Some Effects of Interactions Among Minor Element Additions on the High-Temperature Oxidation Behavior of Ni-Base Alumina-Forming Alloys, First International Conference on Industrial Gas Turbine Technologies CAME-GT Brussels, 10-11 July 2003.

[70] D. M. Likin and D. R. Clarke, "Measurement of the stress in oxide scales formed by oxidation of aluminum containing alloys", *Oxid. Met.*, 45, 267-80, 1996.

[71] K. W. Schlichting, K. Vaidyanathan, Y. H. Sohn, E. H. Jordan, M. Gell, N. P. Padture, "Application of Cr^{3+} photoluminescence piezo-spectroscopy to plasma-sprayed thermal barrier coatings for residual stress measurement", *Mater. Sci. & Eng.*, A 291. 68-77, 2000.

[72] C. Mennicke, E. Schumann, C. Ulrich, M. Ruehle, *Mater. Sci. Forum*, 389, 251-4, 1997.

[73] F. N. Rhines, J. S. Wolf, *Met. Trans*, 5, 1701-10, 1970.

[74] D. B. Dove, D. H. Baldwin, *Met. Trans*, 5, 1637-441, 1974.

[75] E. Schumann, C. Sarioglu, F. R. Blacheere, F. S. Pettit, G. H. Meier, *Oxid. Metals*, 53, 259, 2000.

[76] S. M. Meier, D. K. Gupta, *J. Eng Gas Turbines and Power,* 116, 250, 1994.

[77] D. Zhu, R. A. Miller, *J. Mater. Res.*, 14, 146, 1999.

[78] V. K. Tolpygo, D. R. Clarke, *Oxid. Metals*, 49, 187-211, 1998.

[79] S. Laxman, B. Franke, B. W. Kempshall, Y. H. Sohn, L. A. Giannuzzi and K. S. Murphy, *Surf. Coat. Technol.*, 177-178, 121-130, 2004.

[80] L. Grabner, *J. Appl. Phys.*, 49, 2, 580, 1978.

[81] Q. Ma and D. R. Clarke, "Stress measurement in single-crystal and polyctrstalline ceramics using their optical fluorescence*", J. Am. Ceram. Soc.,* 76 (6) 1433-40, 1993.

[82] J. R. Christensen, D. M. Lipdin, D. R. Clarke, and K. Murphy, "Non-destructive evaluation of oxidation stresses through thermal barrier coatings using Cr^{3+} peizospectroscopy", *Appl. Phys. Lett*., 69, 3754-56, 1996.

[83] D. M. Lipkin and D. R. Clarke, *J. Appl. Phys*., 77, 1885, 1995.

[84] Y. H. Sohn, K. Vaidyanathan, M. Ronski, E. H. Jordan, M. Gell, *Surf. Coat. Technol*., 146-147, 102, 2001.

[85] Y. H. Sohn, K. Schlichting, K. Vaidyanathan, E. H. Jordan, M. Gell, *Metall. Mater. Trans.* A, 31 A, 2388, 2000.

[86] V. Sergo, D. R. Clarke, *J. Am. Ceram. Soc*., 81, 3237, 1998.

[87] A. G. Shillington, D. R. Clarke, *Acta Mater*. 47, 297, 1999.

[88] M. J. Lance, J. A. Haynes, W. R. Cannon, M. K. Ferber, Ceramic Transactions: Non-destructive evaluation of ceramic, American Ceramic Society, Westerville, OH, p.229, 1998.

[89] S. Sridharan, L. Xie, E. J. Jordan, M.Gell, *Surf. Coat. Technol*. In Press.

[90] J. He and D. R. Clarke, *J. Am. Ceram. Soc*., 78, 1347, 1995.

[91] A. A. Kaplyanskii, A. K. Przhevuskii, and R. B. Rozenbaum, *Sov. Phys. Solid State* 10, 1864, 1969.

[92] H. J. Yu, D. R. Clarke, *J. Am. Ceram. Soc*., 85, 1966-70, 2002.

[93] J. A. Nychka, D. R. Clarke, *Surf. Coat. Technol*., 146-147, 110, 2001.

[94] A.L. Schawlow, D. L. Wood, A. M. Clogston, *Phys. Rev. Lett*., 3, 271, 1995.

[95] Q. Z. Wen, D. M. Linpkin, and D. R. Clarke, *J. Am. Ceram. Soc*., 81 (12), 3345-48, 1998.

[96] Y. H. Sohn, V. H. Desai, L. A. Giannuzzi, UTSR Semi-Annual Report, No.1, 2002.

[97] N. Mu, J. Liu, Y. H. Sohn, Y. L. Nava, *Surf. Coat. Technol*. In Press.

[98] X. Y. Gong, D. R. Clarke, *Oxid. Metals*, 50, 355, 1998.

[99] A. G. Evans, J. W. Hutchinson, *Int. J. Solids Struct.* 20, 455, 1984.

[100] A. G. Evens, M. Y. He, J. W. Hutchinson, *Prog. Mater.Sci.,* 46, 249, 2001.

[101] Y. H. Sohn, J. H. Kim, E. H. Jordan, M. Gell, *Surf. Coat. Technol.*, 146-147, 70-78, 2001.

[102] D. R. Mumm, A. G. Evans, *Acta Mater*., 48, 1815, 2000.

[103] R. C. Pennefather, and D. H. Boone, *Surf. Coat. Technol*., 76-77, 47, 1995.

[104] J. W. Holmes, and F. A. McClintock, *Metall. Trans.* 21A, 1209, 1990.

[105] J. W. Hutchinson, Z. Suo, *Adv. Appl. Mech*., 29, 63, 1992.

[106] A. G. Evans, G. B. Crumley, R. E. Demaray, *Oxidation of Metals*, 20, 5-6, 193, 1983.

[107] S. R. Choi, J. W. Hutchinson, A. G. Evans, *Mechanics of Materials*, 31, 7, 431, 1999.

[108] S. R. Choi, J. W. Hutchinson, A.G. Evans, *Mechanics of Materials,* 31, 431-447, 1999.

[109] B. W. Kempshall, Y. H. Sohn, S. K. Jha, S. Laxman, R. R. Vanfleet and J. Kimmel, *Thin Solid Films*, in press.

[110] G. M. Kim, N. M. Yanar, E. N. Hewitt, F. S. Pettit, G. H. Meier, *Scripta Materialia*, 46, 489-495, 2002.

[111] X. Chen, R. Wang, N. Yao, A.G. Evans, J.W. Hutchinson, R.W. Bruce, "Foreign object damage in a thermal barrier system: mechanisms and simulations", *Materials Science and Engineering* A352, 221-231, 2003.

[112] J. R. Nicholls, *Materials Science Forum*, 935, 251-4, 1997.

[113] K. Gamo, *Nuclear Instruments and Methods in Physics Research B*, 121, 464-469, 1997.

[114] T. Kamino, T. Yaguchi, T. Ohnishi, K. Umemura, S. Tomimatsu, *Micoroscopy and Microanalysis 6* (Supplement 2), 510, 2000.

[115] V. K. Tolpygo and D. R. Clarke, *Acta Mater.*, 48, 3283-323, 2000.

[116] L. D. Xie, Y. H. Sohn, E. H. Jordan, M. Gell, *Surf. Coat. Technol*., 176, 57-66, 2003.

[117] S. Sridharan, L. D. Xie, E. H. Jordan, M. Gell, *Surf. Coat. Technol*., 179, 286-296, 2004.

[118] T. F. An, H. R. Guan, X. F. Sun, Z. Q. Hu, *Oxidation of Metals*, Vol. 54, No. 3/4, 2000.

[119] J. D. Kuenzly and D. L. Douglass, "The Oxidation Mechanism of Ni_3Al Containing Yttrium," *Oxid. Met*., 8 139-178, 1974.

[120] J. Nowok, "Formation Mechanisms of Keying or Pegging Yttrium Oxide and increased Plasticity of Alumina Scale on FeCrAlY," *Oxid. Met*., 18, 1-17, 1982.

[121] A. Christensen, E. A. Asche and E. A. Carter, "Atomic-level properties of thermal barrier coatings: Characterization of metal-ceramic interfaces", TBC chapter of Department of Chemistry and Biochemistry, University of California, Los Angeles, CA.

[122] D. R. Mumm, A. G. Evans, *Acta Mater*., 48, 1815-1827, 2000.